2001

Investigation of iron-aluminum based weld overlay and thermal spray coatings for the protection of boiler tubes in high-temperature low NOx environments

Jonathan Regina
Lehigh University

Regina, Jonathan

Investigation of Iron-Aluminum Based Weld Overlay and Thermal Spray Coatings for…

January 2002

INVESTIGATION OF IRON-ALUMINUM BASED WELD OVERLAY AND THERMAL SPRAY COATINGS FOR THE PROTECTION OF BOILER TUBES IN HIGH-TEMPERATURE LOW NOx ENVIRONMENTS

By

Jonathan Regina

A Thesis

Presented to the Graduate and Research Committee

of Lehigh University

in Candidacy for the Degree of

Master of Science

in

Materials Science and Engineering

Lehigh University

December 3, 2001

This thesis is accepted and approved in partial fulfillment of the requirements for the Master of Science.

December 1, 2001

Date

Thesis Advisor

Co-Advisor

Chairperson of Department

Acknowledgments

First off, I would like to acknowledge and thank my advisors, Dr. Arnold R. Marder and Dr. John N. DuPont, for providing the opportunity to get involved with a variety of projects as an undergraduate as well as the opportunity to pursue my present research. I would like to thank Dr. Marder for all of his help and advice through not only my undergraduate years when I was naive and overly ambitious, but over the last several humbling years as well. His technical input along with his advice on all aspects of life has been an invaluable asset. Special thanks go out to the project sponsors, for without them none of this would have been possible. Funding for this project was provided by the Fossil Energy Advanced Research and Technology Development (AR&TD) Materials Program, US Department of Energy, under subcontract 19X-SU604V with UT Battelle Research Corporation.

From the outside community, I would like to thank Vinod Sikka and Bruce Pint of Oak Ridge National Laboratory for providing the cast alloys used during the corrosion experimentation. Special thanks as well to Ametek and Oak Ridge National Laboratory for supplying the Fe-Al powder used to make the thermal spray coatings. Thanks also goes to Richard Wright of Idaho National Engineering and Environmental Laboratory for producing the HVOF thermal sprays used in the corrosion experiments. In addition, I would also like to thank Peter Tortorelli, Ian Wright, Bruce Pint, and Mike Brady from Oak Ridge National Laboratory for their help and thought provoking discussions.

From the Lehigh Community, I would like to thank Arlan Benscoter for his aid in metallographic preparation, Dave Ackland for his help with the electron microscopy, and Mike Rex for his help in preparing corrosion specimens. Thanks so much to Stephen Banovic and Kevin Luer for their help in understanding the subject of high-temperature corrosion. I would also like to thank fellow students Ryan Deacon for his help in preparation and characterization of

thermal spray coatings and Shane Para for his assistance with regression analysis. Special thanks also must go to my fellow group members both past and present: Phil Anderson, Stephen Banovic, Nick Barbosa, Ryan Deacon, Chad Kusko, Kevin Luer, Melissa Lim, Jesse Nawrocki, Brian Newbury, Rick Norecker, Shane Para, Matt Perricone, Heather Snow, and Ray Unocic. Each has taught me a thing or two about research, surviving graduate school, making it through life, and friendships. Thank you all for keeping me "relatively sane" over the past few years.

I would like to thank my friends and family for their understanding and support. Hopefully now everyone can understand why I practically disappeared for the last two years. I want to thank both my father, Larry, and my mother, Gail, for raising me with a good (although slightly misshapen) head on my shoulders, as well as my brothers Jeff and Jeremy who have given me so many great memories (as well as a few well-placed scars).

I would especially like to thank my beautiful wife, Merideth. Thank you so much for supporting me and putting up with me on a daily basis. The excitement you project when I have a break-through and the compassion that you show when I've had enough is so very appreciated. YOU are my driving force to finish and get on with our life together. I love you.

Table of Contents

Abstract

Low NOx power plant furnaces have encountered major problems with high-temperature corrosion of the waterwall boiler tubes. The unacceptable wastage has been attributed to sulfur rich gasses that promote the formation of non-protective sulfides on the surface of the currently used boiler tubes. The boiler tube corrosion problem is compounded by the accumulation of sulfur rich slag on the boiler tube surface. The objective of this research was to develop corrosion resistant iron-aluminum based coatings that can be deposited as either a weld overlay cladding or a thermal spray coating.

Weld overlay coatings containing 7.5-10wt%Al and 0-5wt%Cr were chosen as experimental alloys for gaseous corrosion testing and gas-slag corrosion testing. Two alloys also contained titanium additions to determine if titanium had any effect on the corrosion behavior of Fe-Al-Cr alloys. High-Velocity Oxy-Fuel (HVOF) thermal spray coatings containing aluminum contents greater than the weld overlay claddings were chosen for gaseous and gas-slag corrosion testing as well. The corrosion tests were carried out at 500°C in three different gaseous corrosive environments for 100 hours. The gaseous environments used for testing ranged from a sulfidizing environment (high P_{S_2}, low P_{O_2}), to a mixed oxidizing/sulfidizing environment (intermediate P_{S_2}, P_{O_2}), to an oxidizing environment (low P_{S_2}, high P_{O_2}). The slag found on the surface of boiler tubes was simulated by placing FeS_2 powder in contact with the test material and then blowing corrosive atmospheres over the setup.

Gaseous corrosion tests were carried out in a furnace that measures weight changes over time. Kinetic data was initially used to describe the corrosion behavior of the alloys. It was found that the scale morphology must be considered in detail to determine whether an alloy was protective or not. Based on these characterization methods, it was found that alloys required 10wt%Al to significantly reduce the amount of corrosion that occurs after 100 hours of exposure in all three gaseous environments. To completely prevent unwanted corrosion from occurring

chromium additions of 5wt% were required. Gas-slag corrosion testing showed similar results to the gaseous corrosion testing. To prevent significant inward growing corrosion from occurring in an alloy exposed to FeS_2 powder while in contact with the mixed atmosphere and the oxidizing environment, 10wt%Al was required. Additions of 5wt%Cr to alloys containing 10wt%Al helped prevent any corrosion from occurring in the gas-slag environments, as well.

HVOF thermal spray coatings containing 16wt%Al and 21wt%Al were exposed to the mixed oxidizing/sulfidizing environment and the oxidizing environment both with and without FeS_2. The HVOF thermal spray coatings contained relatively low amounts of oxides and porosity, which indicated that they were good quality coatings. Thermal spray coatings exposed for 100 hours in these environments either developed cracks that ran along or parallel to the coating/substrate interface, suffered a significant coating thickness loss, or they formed corrosion products at the coating/substrate interface. Coatings exposed to the mixed oxidizing/sulfidizing environment for 450 hours demonstrated significant coating thickness loss as well as large amounts of corrosion both on the surface of the coating and at the coating/substrate interface.

Overall, it was determined that HVOF thermal spray coatings are unacceptable for the protection of waterwall boiler tubes found in Low NOx power plant furnaces. Weld overlay coatings were found to be protective with aluminum contents of at least 10wt%Al and chromium contents of 5wt%. Although the alloy compositions used in this study have been shown to be protective in these environments, the welding behavior of these alloys is unknown. Future work will focus on the weldability of Fe-Al-Cr alloys to determine the maximum aluminum and chromium concentrations that can be achieved when depositing Fe-Al-Cr weld overlay claddings. The corrosion behavior of these welds will then be determined and evaluated.

1. Chapter 1: Low NOx Waterwall Corrosion

1.1. Introduction

New clean air regulations have called for a reduction in the emission of NOx, a known carcinogen produced from coal combustion in fossil-fueled power plants. In order to reduce the NOx emission, the design of the burner and the combustion process have been changed in Low NOx furnaces. This new combustion procedure has caused unacceptable corrosion wastage of 2¼ Cr-Mo steel boiler tubes. Conventional furnaces generally formed compounds such as SO_2 in the gaseous environment. These compounds are less corrosive at the boiler wall temperatures as they form slower growing oxides. The new combustion parameters result in the formation of H_2S, which causes accelerated corrosion due to the formation of faster growing, porous sulfide scales with high defect structures. In addition to the gaseous corrosion found in Low NOx burners, sulfur rich slag deposits accumulate on the boiler tube walls. The sulfides found in these slag deposits are in intimate contact with the boiler tube material. Therefore, at high temperatures, rapid diffusion between the slag components and the substrate can contribute to the accelerated wastage found in these types of combustion burners.

Since the clean air regulations, corrosion resistant alloys have been considered as replacement materials for the steel tubes and as coatings to protect the underlying burner walls. Replacing the burner walls with a corrosion resistant alloy is a long and expensive process, so coatings such as weld overlays and thermal sprays have been the focus of research. Typically, superalloys and stainless steels have been used as weld overlay coatings[1,2]. These coatings are known to be expensive and form a brittle interfacial layer, which can be detrimental to corrosion resistance under thermal cycling conditions where differences in thermal expansion coefficients could cause the coatings to flake off[1]. Recently, much work has been done investigating iron-aluminum based alloys as coatings. Iron-aluminum alloys have demonstrated lower oxidizing and sulfidizing corrosion rates than traditional stainless steel coatings due to the formation of

aluminum rich scales rather than iron or chromium rich scales[3]. Iron-aluminum alloys are also less costly than stainless steels due to the major alloying element being aluminum rather than chromium[4]. Ternary additions to iron-aluminum based alloys are now being investigated to help improve thermal cycling and overall corrosion behavior[5,6].

Iron-aluminum alloys have demonstrated a sharp decrease in strength at approximately 600°C and are difficult to form due to low ductility at room temperature[1]. These alloys are therefore poor choices for structural applications but are potentially good candidates for coatings. Weld overlays up to 10wt%Al have been shown to be readily weldable and resistant to hydrogen cracking, which occurs above 10wt%Al[7]. These weld overlays have also demonstrated superior corrosion resistance to commercial coatings[3,8]. Thermal sprays utilizing the High Velocity Oxy-Fuel (HVOF) procedure have resulted in good quality coatings as well. HVOF thermal sprays have demonstrated low porosity and oxide inclusions in contrast to Arc Plasma Sprays (APS), which usually contain high amounts of oxides and interconnected porosity [9]. Weld overlays have a better bond to the substrate than thermal sprays due to a metallurgical bond during mixing. On the other hand, thermal sprays do not crack due to hydrogen embrittlement unlike the weld overlay coatings. Iron-aluminum coatings must be extensively studied to determine the best candidate alloy and coating process to protect the boiler walls.

This review will focus on the problem of accelerated corrosion of waterwalls due to the Low NO_X combustion process. General high temperature gaseous corrosion will be reviewed. Thermodynamics will be discussed with respect to phases that may form on pure iron, binary iron-aluminum alloys, and iron-aluminum alloys with ternary additions in these environments. General kinetics of corrosion will be discussed and related to the types of scales that may form. Literature pertaining to the corrosion of pure iron, binary iron-aluminum alloys, and iron-aluminum based alloys with ternary additions will be reviewed in the final sections of this chapter.

1.2 Low NOx Combustion Process

Burning coal in coal-fired power plants can result in very dynamic environments. Traditionally, the environments seen in these coal-fired burners consisted mainly of SO_2 and NOx (a collective term for NO and NO_2 compounds). Emission of NOx compounds from these burners has been identified as a health hazard for a long time[10]. Identifying and controlling the amount of SO_2 given off is a relatively easy process. NOx gases, on the other hand, are difficult to identify and are therefore more difficult to control.

A product from burning coal is nitric oxide (NO), which oxidizes very easily to nitrogen dioxide (NO_2). The latter has been identified as a carcinogen as well as a large contributor to air pollution as it is the major component to smog[10]. Clean Air Act regulations have focused on reducing the amount of NOx gasses that are released into the atmosphere. Industrial fossil-fueled power companies primarily use two ways to reduce the amount of NOx emissions. One method is to add post-combustion equipment to the furnace to chemically remove the NOx. The other method involves adjusting the burner parameters and the combustion process so that the NOx gasses reduce to safe compounds.

The first method consists of removing the NOx compounds by chemically treating the gas stream after the combustion process is complete. There are many techniques of chemically removing the NOx from the flue gas, but most of these methods can be generally grouped as selective catalytic reduction (SCR)[10]. These SCR methods are very efficient, as up to 80% of the NOx gas can be removed, but they are also very costly. Not only is this type of process expensive to operate, but extra equipment must be installed into the boiler, which adds to the overall cost.

Rather than add new control equipment to the furnace, many plants realized the operation conditions of the furnace could be modified to lower the amount of NOx that is formed during combustion. This method consists of adjusting the air/coal ratios, the burner placement, and the

timing of mixing air and fuel[10]. There are two sources of nitrogen in the combustion process: the coal and the air used for combustion. The furnace conditions will control the nitrogen reaction and form either NO or N_2, the first being very reactive and the later being a non-reactive compound. The amount of NOx that comes from the nitrogen in air can be controlled fairly easily by delaying the mixing of the fuel and the air[10]. The delaying process must be carefully controlled because too long a delay could reduce the combustion efficiency. In order to eliminate the NOx coming from the coal (the major contributor) a staged combustion reaction can be created within the furnace. This process consists of having a fuel-rich combustion zone initially, and adding air gradually in second and third combustion zones higher up in the furnace so that complete burnout can occur[10]. This process results in the formation of N_2 rather than NO and is utilized in many Low NOx furnaces.

1.2.1 Gas Environment

The staged combustion used in most modified furnaces not only reduces the NOx gases formed during combustion but they also reduce the stable SO_2 gases. The reduction of SO_2 creates a highly reducing environment that has caused accelerated corrosion on the waterwall tubes. Previously, the waterwall tubes showed corrosion due to oxidation, but the oxide scales that formed provided a protective layer, which reduced the corrosion rate. After modifications, the atmosphere in the furnace changes from an oxidizing environment to a sulfidizing environment and instead of forming a protective oxide layer, an iron-sulfide scale dominates the surface of the waterwall tubes[11]. The iron-sulfide scale is less protective than the iron-oxide scale so corrosion rates are accelerated. In fact, waterwall tubes that previously had operating lives of 12-15 years are now failing after only four years in service[11].

Initially, when the coal and air are mixed, the fuel/air ratio is high and a reducing atmosphere is present along the walls of the burner. This section of the furnace is where most

waterwall wastage occurs due to the high amount of sulfur from the coal and the low amount of oxygen that is present in the atmosphere. The reducing environment seen in this area can contain H_2S, CO, and chlorine gas[12]. Gabrielson and Kramer measured the amount of reducing gasses that can be found adjacent to the waterwall tubes in a typical furnace[13]. They found that the atmosphere at the furnace walls consisted of high amounts of CO (11-12%), high amounts of H_2S (up to 1000ppm), and low amounts of O_2 (less than 0.1%).

The amount of H_2S, CO, and chlorine will vary depending on the furnace conditions and the makeup of the coal used as fuel[14]. The gasses present can change dramatically even within the same furnace as test probes directly next to each other produced different results. Although Gabrielson and Kramer measured the reducing gasses, they only used 12 test probes and the data varied from point to point along the wall. Therefore, the atmosphere reported above should be used only as a reference and not for quantitative analysis of the environment.

1.2.2 Slag Deposits

High temperature corrosion can be accelerated due to ash deposits and molten slag that can accumulate on the boiler tube walls. Flame impingement from the burner can increase the amount of ash and unburned coal reaching the furnace walls, which can further accelerate the waterwall wastage. The accumulation of these deposits transforms into a layer of slag, which can contain various reactive species. For example, slag can contain chlorine and sulfur from the unburned coal as well as excess carbon from ash[14]. In contrast, furnaces prior to retrofitting were found to have slag accumulations that consisted mainly of ash deposits and contained little or no chlorine and sulfur[14].

Slag collections from actual boilers have shown that FeS (troilite) can be found in areas where corrosion losses were high[15]. FeS will form due to incomplete decomposition of pyrite (FeS_2) during the combustion process. Pyrite, which is found in coal, may not be able to reduce

completely to FeO, due to a low amount of oxygen in the atmosphere, and instead form FeS[15]. Upon combustion, flame impingement could possibly deposit all three of these compounds: pyrite (FeS_2), troilite (FeS), and wustite (FeO) on the boiler tube walls.

Sulfates and chlorides of alkaline metals (Na, K) and alkaline earth metals (Ca) can also be found deposited on the walls in some coal combustion furnaces. The specie that forms will depend primarily on the coal makeup and the conditions of the boiler[16]. The high temperatures present in the furnace may be high enough to partially melt the slag deposit. The waterwall tube temperature (~ 450-700°C) is not high enough to form a liquid slag adjacent to the tubes, but an outer layer of liquid slag could result[11]. The presence of alkaline sulfates and chlorides can contribute to reducing the melting point of the ash deposits by 300-550°C[16]. An outer layer of molten slag will influence the chemical composition and can increase the solid-state reactions occurring along the waterwalls.

1.2.3 Summary

Attempting to alter the burner conditions to reduce the amount of NOx emissions from coal-fired power plants has resulted in unacceptable corrosion rates along the furnace walls. The main contributor to these accelerated corrosion rates is the furnace atmosphere changing from an oxidizing to a reducing environment. The reducing atmosphere seen in most retrofitted furnaces contains H_2S, CO, and chlorine gas (HCl). Slag consisting of ash, unburned coal, sulfides, and chloride deposits on the furnace walls can increase the reaction rates at the surface of the substrate. In order to understand the reactions that take place during exposure, it is important to discuss the factors that influence the corrosion behavior of an alloy. Therefore, in the next section general high temperature corrosion will be discussed and the factors affecting the high temperature corrosion will be considered in detail.

1.3 High Temperature Corrosion

There are various ways that a corrosive species can attack a material. For high temperature applications, such as furnace wall coatings, the types of corrosion that must be considered are gaseous, solid-state, and mixed gaseous/solid-state corrosion. The first involves a reactive gas, such as oxygen, sulfur, or nitrogen, coming in contact with a solid material at high temperature. Solid-state corrosion involves a reactive solid species, such as a sulfide or chloride, in contact with a metal. When both types of corrosion occur, reactions between the gas and slag could contribute further to waterwall wastage. Diffusion plays an important role in both gaseous and solid-state corrosion. Therefore the diffusion of metal and reactive specie through the scale is an important consideration during corrosion. Although the mechanism for each type of corrosion may be different, the main factors influencing the corrosion resistance of a material are thermodynamics, kinetics, and morphology of the corrosion products present on the alloy. The scale that forms will be governed by the thermodynamics of the system. How fast the scale covers the material is controlled by the kinetics of the scale growth. How protective the scale is to the material depends not only on what type of scale is present, but also on the morphology of the scale. Therefore, the following sections will outline the diffusion mechanisms for scale growth, the thermodynamics of systems of interest, kinetics of scale growth, and scale morphologies that can form.

1.3.1 Diffusion Controlled Corrosion

As previously mentioned, gaseous corrosion occurs when a reactive gas comes in contact with a solid at an elevated temperature. The gas adsorbs to the solid and they react to form a scale at the gas-solid interface. A general reaction between a metal and oxygen can be seen as:

$$M(s) + \tfrac{1}{2}O_2(g) = MO(s) \qquad (1)$$

where the oxide (MO) acts as a barrier between the metal (M) and the oxygen gas (O_2). If the reaction is to occur any further, either oxygen or metal ions must travel through the oxide scale to react at either the gas-oxide interface or at the metal-oxide interface. Therefore, ionic transportation paths used by the metal and reactive specie are important factors when considering the mechanisms of high temperature corrosion. The basic transportation mechanisms for cations and anions through the oxide scale are diffusion controlled. Fast transportation of metal cations and gas anions can also occur along oxide grain boundaries or at macroscopic scale defects, such as cracks. These sites act as fast diffusion paths, sometimes referred to as short circuit paths[17]. If a crack is present in an oxide scale, the gas can travel into the crack and react directly with the metal. This can increase the corrosion rate substantially. The following will describe the diffusion mechanisms for ion transport in oxides, which apply not only to oxides but to sulfides as well.

There are a few mechanisms available to explain how the metal cations or oxygen anions are transported through the scale. Ions can move through ionic defects, they can move due to varying valency, and through grain boundaries or macroscopic defects. The first mechanism for the transportation of ions applies when there are ionic vacancies within the oxide lattice. There are two main types of defects that can be seen in ionic compounds: Schottky and Frenkel defects. Schottky defects have an equal number of cation and anion vacancies in order to maintain electrical neutrality. If Schottky defects are present, it can be assumed that both cations and anions will be mobile. Frenkel defects assume a perfect anion lattice where cation vacancies are present. If Frenkel defects are present, it can be assumed that only cations will be mobile. Although, defects are found predominately in stoichiometric compounds, they can also be seen in non-stoichiometric ionic compounds as well. The second mechanism for ion transportation in non-stoichiometric compounds comes from the fact that the metal to non-metal ratio does not exactly match the chemical equation, even though the compound has no electric charge. This can

be explained by assuming that either the cation or anion has variable valency. For example, $Fe_{1-\delta}O$ is a non-stoichiometric ionic compound but it is electronically neutral due to Fe^{2+} and Fe^{3+} ions being present in the lattice. Although both cations and anions can diffuse through the scale, most common metals grow oxides primarily by the outward diffusion of metal cations[18].

1.3.2 Thermodynamics

Thermodynamics play an important role in determining what type of oxide may form in a high temperature, corrosive environment. Although thermodynamics alone will not predict what oxide will form in a certain environment, it can tell what reactions are possible and therefore what oxide species may be present. There are various tools that can be used to determine what phase may be present in a given environment. The two most commonly used diagrams are the equilibrium phase diagram and phase stability diagrams.

1.3.2.1 Equilibrium Phase Diagrams

Equilibrium phase diagrams can give a large amount of information about a system including what stable phases can be present, solubility limits, melting and solidification temperatures. Equilibrium phase diagrams are limited though, as they provide no information on how rapid a phase will form. Binary equilibrium phase diagrams plot temperature versus composition on the axes and the possible phases are displayed within the graph. Typically, binary equilibrium phase diagrams can be constructed for an alloy with two components or a pure metal and one reactive species. Ternary equilibrium phase diagrams are typically isothermal sections of phases that may be present in a system with three elements. Ternary equilibrium phase diagrams can be constructed for an alloy with three components, a binary alloy and one reactive species, or a pure metal and two reactive species. Because ternary phase diagrams are typically isothermal

sections, they must be specific to the temperature of the system. Otherwise, the phase coexistence lines may shift, resulting in an inaccurate depiction of the system.

Various binary and ternary equilibrium phase diagrams will be reviewed in the following sections to describe the iron-aluminum system and the significant phases that may be seen during corrosion studies. First the pure iron system will be considered, followed by binary iron-aluminum system, and then the iron-aluminum system with ternary alloy additions will be covered. These diagrams and phases will be used later to describe the corrosion behavior of these alloys.

Fe-O Equilibrium Phase Diagram[19]

Prior to the burner parameter changes that decreased the amount of NOx emissions in coal-fired boilers, the environment in the burner was predominately an oxidizing environment (high Po_2, low Ps_2). Considering the iron-oxygen equilibrium phase diagram (Figure 1), only a few reaction products are stable phases at temperatures below 800°C. The three dominant phases that are stable at lower temperatures are $Fe_{1-\delta}O$ (wustite), Fe_3O_4 (magnetite), and Fe_2O_3 (hematite). Wustite is stable only until 570°C, whereas magnetite and hematite are stable to room temperature.

Fe-S Equilibrium Phase Diagram[20]

A change in furnace conditions resulted in an environment shift from an oxidizing to a predominately sulfidizing environment (high Ps_2, low Po_2). The Fe-S equilibrium phase diagram, seen in Figure 2, shows the various types of iron-sulfide scales that may form in these types of environments. $Fe_{1-\delta}S$ (pyrrhotite) is a non-stoichiometric compound with a few polymorphs. Higher sulfur concentration gives rise to FeS_2, which is either pyrite or marcasite depending on whether it has a simple cubic or orthorhombic crystal structure, respectively.

Fe-Al Equilibrium Phase Diagram[21]

When adding aluminum to iron, multiple iron-aluminum phases can be present over a wide range of aluminum concentrations. The iron-aluminum equilibrium phase diagram (Figure 3) shows a number of phases that can be present. At low aluminum concentrations, a disordered solid-solution known as (αFe) can be seen up to around 11wt%Al. At higher aluminum concentrations, the disordered solid-solution will transform into either FeAl or Fe_3Al, both of which are ordered bcc structures. At low temperatures, Fe_3Al can be seen between 13-20wt%Al, and FeAl can be present between 20-32wt%Al. At elevated temperatures, FeAl can solely be present and contain up to 37wt%Al. At higher aluminum contents, the phase $FeAl_2$ can be seen at around 49wt%Al, Fe_2Al_5 can be present between 53-57wt%Al, and $FeAl_3$ can be seen between 58-61wt%Al.

Looking specifically around the Fe_3Al phase field, it can be seen that at lower temperatures (<300°C) the disordered α-Fe phase begins to transform into an ordered Fe_3Al ($D0_3$ crystal structure) phase at approximately 10wt%Al (19at%Al). There have been multiple proposed phase diagrams around this region, but the most widely accepted is the diagram proposed by Rimlinger, which can be seen in Figure 4[22]. The two-phase region containing both the disordered α-Fe and the ordered Fe_3Al phase continues from approximately 10wt%Al to 12.5wt%Al (19-23at%Al). At 12.5wt%Al, the two-phase field α + Fe_3Al changes completely to the ordered Fe_3Al phase. The single-phase region of ordered Fe_3Al is present to approximately 17wt%Al (29.5at%Al) when it begins to transform to the ordered FeAl phase (B2 crystal structure). A two-phase ordered region of Fe_3Al + FeAl can be seen up until approximately 22wt%Al (37at%Al) where it completely transforms to the ordered FeAl phase. It should be noted that the dotted lines in Figure 4 represent a magnetic transformation and the subscripts m and n correspond to magnetic and non-magnetic phases.

Al-O Equilibrium Phase Diagram[23]

In order to determine the scales that could be seen in oxidizing and sulfidizing environments, the Al-O and Al-S equilibrium phase diagrams must be considered. The Al-O phase diagram, seen in Figure 5, shows that the only stable phase is α-Al_2O_3. Although this may be the only stable phase for this system, multiple metastable phases have been reported. Upon reviewing alumina scales on high-temperature alloys, Prescott and Graham found that three metastable alumina polymorphs could be found on iron-aluminum based alloys[24]. They reported that alloys in the temperature range of 500-900°C will form primarily a γ-Al_2O_3 scale, whereas θ-Al_2O_3 will form from 900-1000°C. Some authors have reported the detection of δ-Al_2O_3 during the transition from γ-Al_2O_3 to α-Al_2O_3[25-28]. They report that δ-Al_2O_3 can be found within the temperature range of 750-900°C[28]. Above 1000°C, a polymorph will slowly transform to the stable phase α-Al_2O_3, which has a structure based on a hexagonal sub-lattice of oxygen anions with aluminum cations in the interstitial sites. All three alumina polymorphs are based on a fcc sub-lattice of oxygen anions with the aluminum cations arranged differently in the interstitial sites[29]. γ-Al_2O_3 typically can be seen as larger crystals that grow epitaxially from the substrate, whereas α-Al_2O_3 is seen as small crystals, which are randomly oriented[30].

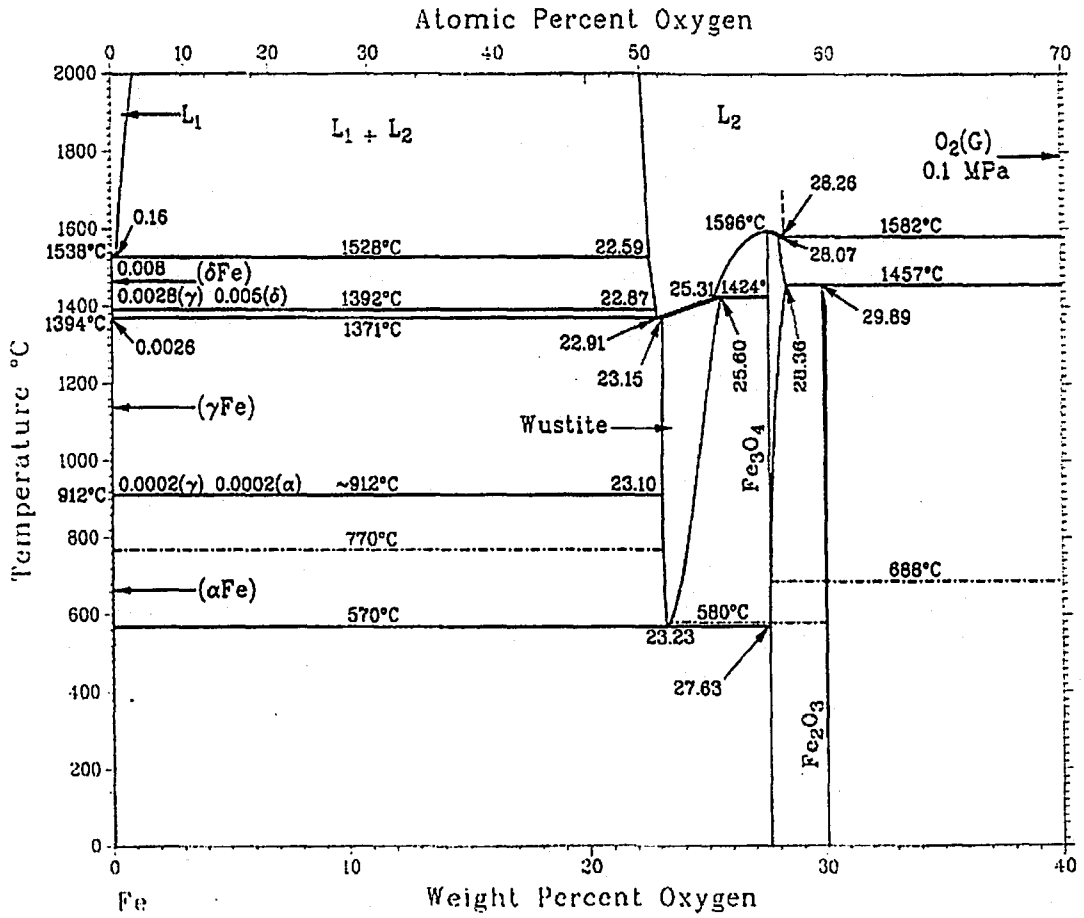

Figure 1 – Fe-O Equilibrium Phase Diagram[19]

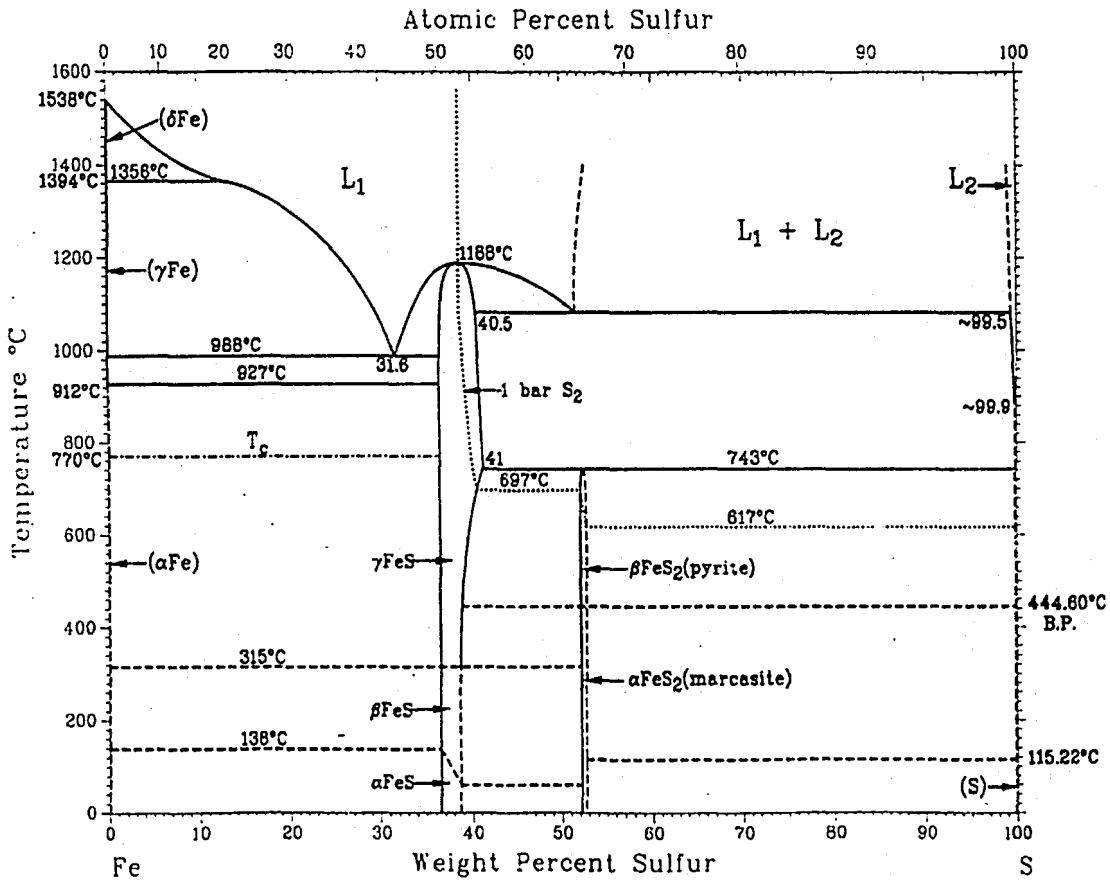

Figure 2 – Fe-S Equilibrium Phase Diagram[20]

Al-S Equilibrium Phase Diagram[31]

When considering a sulfidizing environment, the Al-S equilibrium phase diagram can be seen in Figure 6. At lower temperatures, it can be seen that α-Al_2S_3 is the only stable phase of the Al-S system. α-Al_2S_3 will remain stable up to around 1000°C, where it will transform to γ-Al_2S_3. It should be noted that Al_2S_3 has a relatively low melting point as γ-Al_2S_3 melts at about 1100°C. The low melting point of this phase presents a potential problem, especially at high temperatures where the phase may liquefy and cause rapid diffusion of sulfur into the substrate. At burner temperatures, which is around half the melting point of Al_2S_3 (approximately 450-700°C), the scale will not liquefy but the diffusion of ions will be greatly accelerated, which could lead to more rapid scale growth.

Fe-Al-O Equilibrium Phase Diagram[32]

In order to consider the oxidation behavior of Fe-Al based alloys, it is important to understand the phases that could be present. The ternary equilibrium phase diagram of Fe-Al-O at 700°C can be seen in Figure 7. The only new phase that should be mentioned is a cubic spinel phase known as hercynite ($FeAl_2O_4$), which is commonly referred to as sigma (σ). Although this is the only new phase that may form in this system at this temperature range, multiple phases can coexist with one another. Therefore, many of the phases discussed earlier for the Fe-Al, Fe-O, and Al-O systems may also be present.

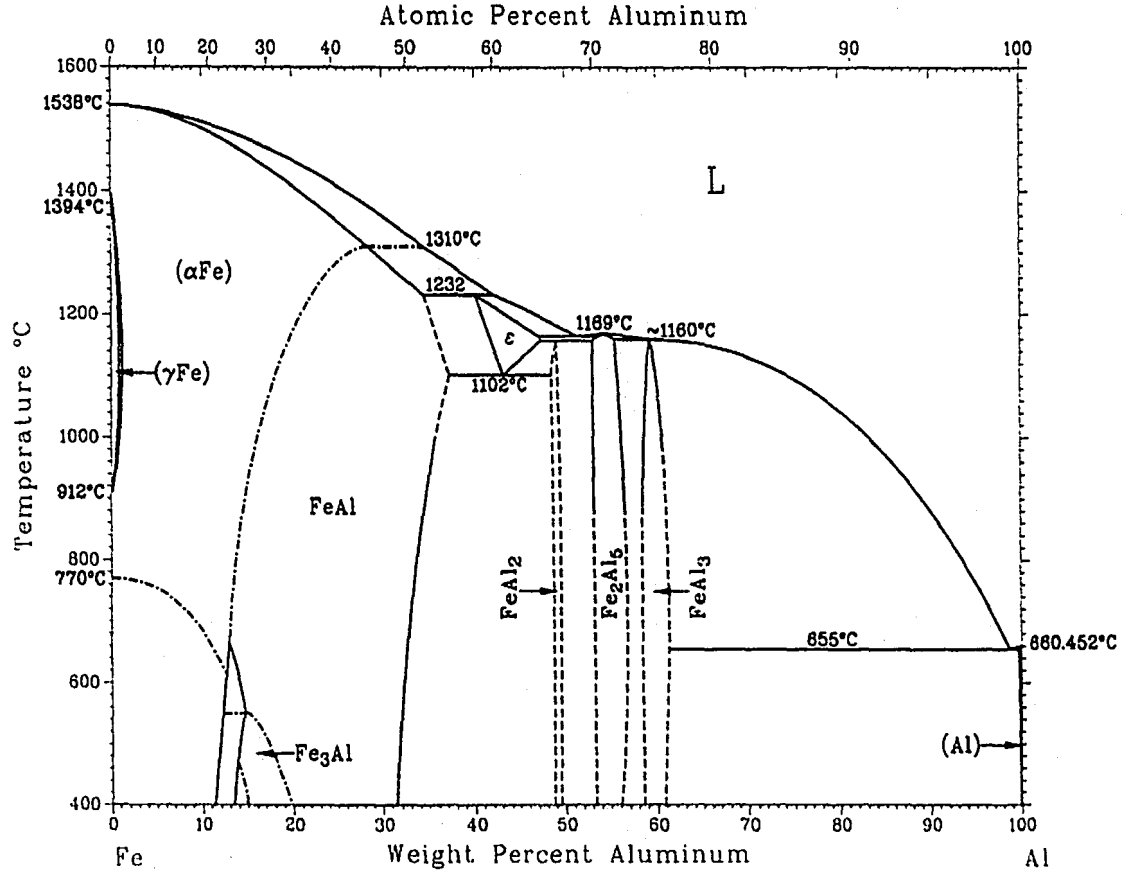

Figure 3 – Fe-Al Equilibrium Phase Diagram[21]

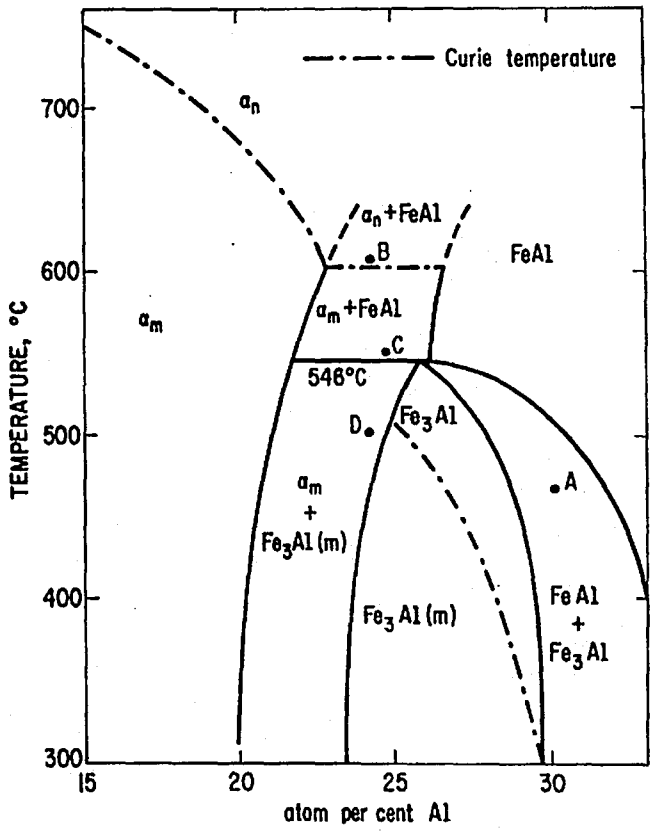

Figure 4 – Iron rich side of the Fe-Al phase stability diagram showing the phases surrounding the ordered Fe_3Al phase.

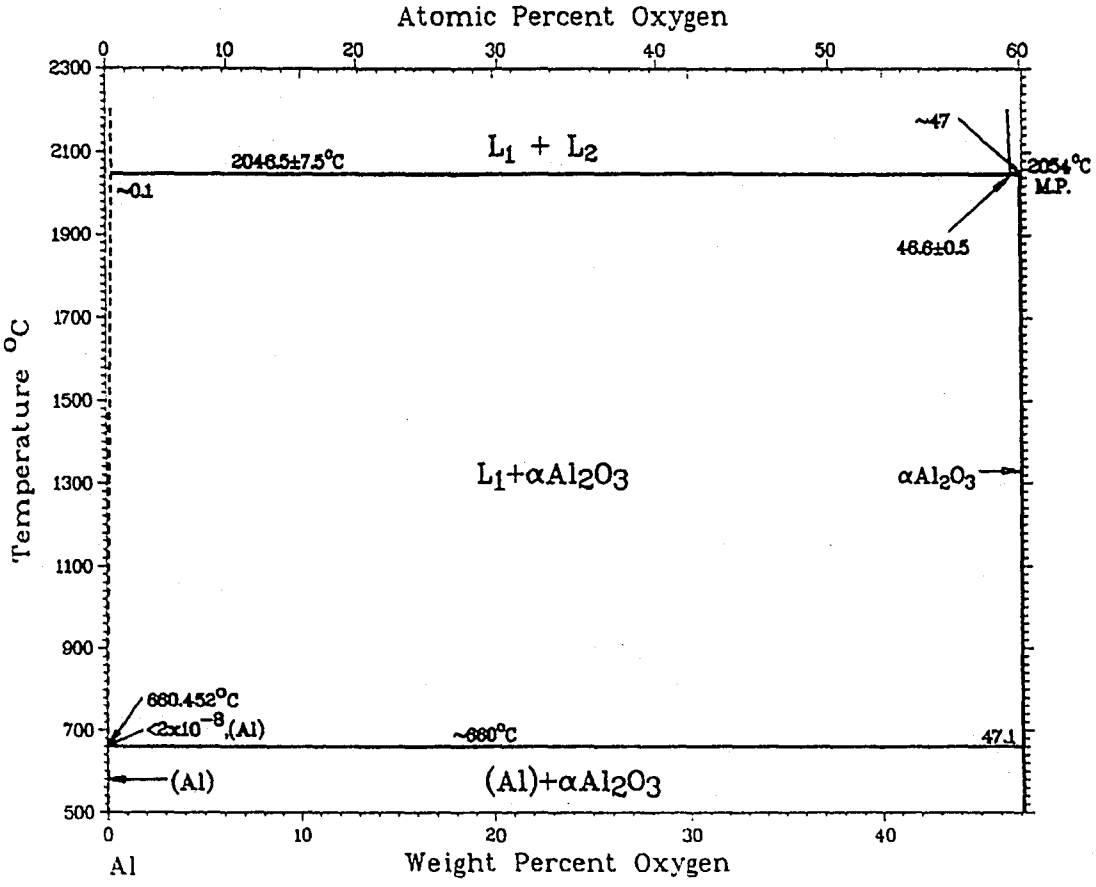

Figure 5 – Al-O Equilibrium Phase Diagram[23]

Fe-Al-S Equilibrium Phase Diagram[33]

The possible phases that could form during the sulfidation of binary iron-aluminum alloys can be seen in the Fe-Al-S ternary equilibrium phase diagram at 900°C (Figure 8). The 900°C isothermal section was used because it provides the best representation of burner conditions out of the available diagrams. Again, only one new phase comes from the addition of sulfur to the iron-aluminum system. Similarly to the Fe-Al-O system, the new phase that can be present in the Fe-Al-S system is the spinel $FeAl_2S_4$ (commonly referred to as τ). As in the Fe-Al-O system, multiple phases can now be present during the sulfidation of binary iron-aluminum alloys.

Cr-O Equilibrium Phase Diagram[34]

Chromium is added to binary iron-aluminum alloys in order to help protect against oxidation attack. It is therefore important to determine possible phases that may form when chromium is exposed to oxygen. The chromium-oxygen equilibrium phase diagram can be seen in Figure 9. The most important phase to note in this partial phase diagram is the line compound Cr_2O_3. This phase is stable over a wide range of temperatures and has an hcp crystal structure, similar to α-Al_2O_3. Less common phases that could possibly form and are not shown on the diagram are Cr_3O_4, CrO_2, Cr_5O_{12}, Cr_6O_{15}, and CrO_3.

Cr-S Equilibrium Phase Diagram[35]

There are several chromium sulfides that could possibly form when chromium is exposed to a sulfidizing environment. According to the chromium-sulfur equilibrium phase diagram (Figure 10) a number of phases are stable at low temperatures. These include $Cr_{1.03}S$, Cr_3S_4, Cr_2S_3, Cr_5S_8, Cr_2S_5, and CrS, which is stable over a wide range of temperature but begins to decompose at around 580°C.

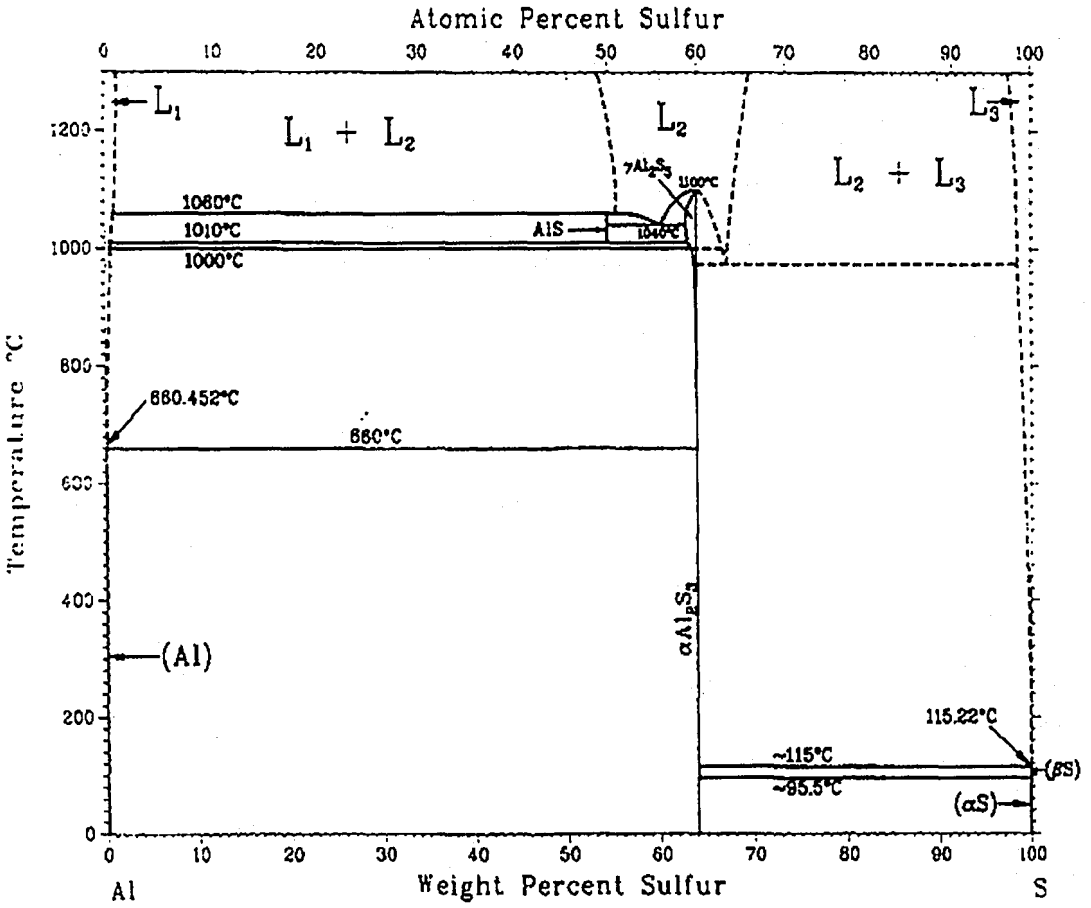

Figure 6 – Al-S Equilibrium Phase Diagram[31]

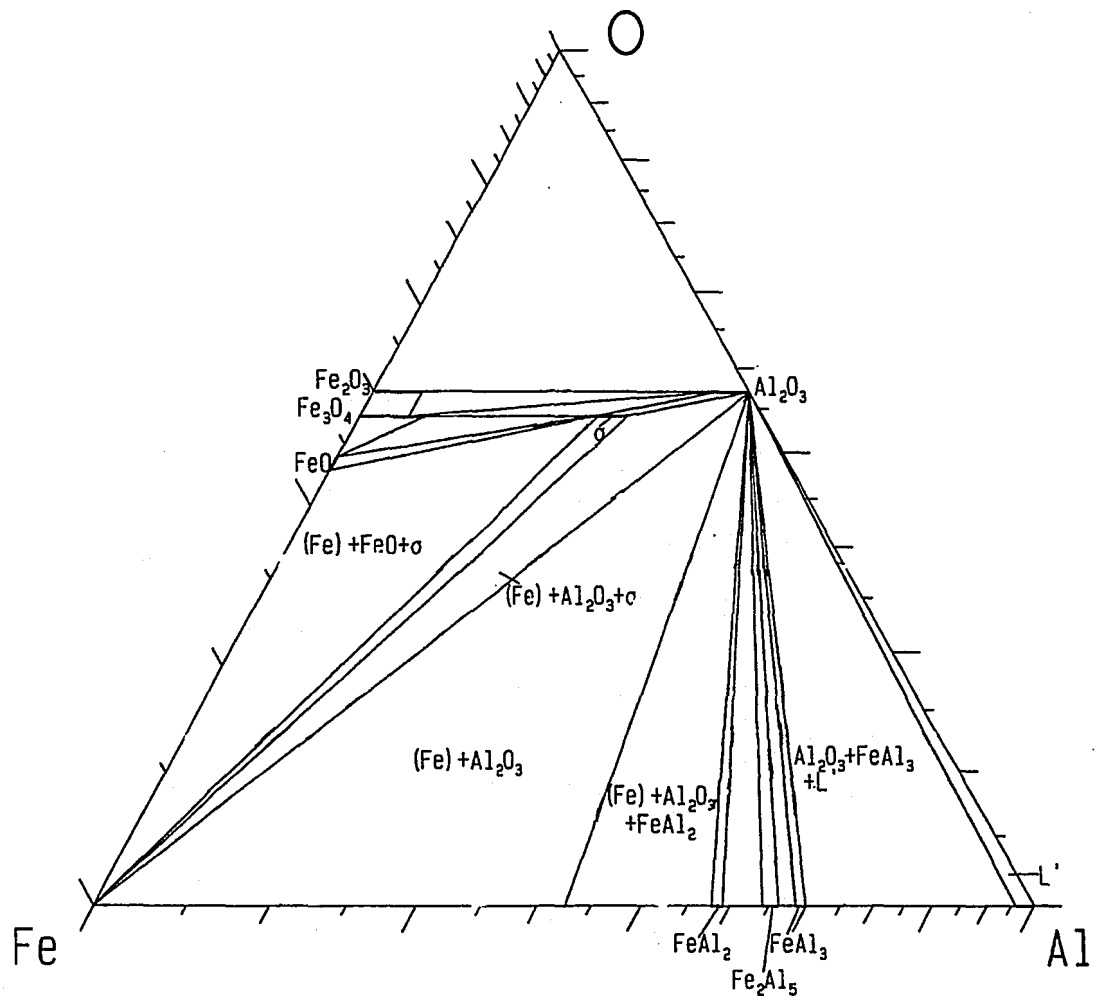

Figure 7 – Fe-Al-O Equilibrium Phase Diagram[32]

Ti-O Equilibrium Phase Diagram[36]

Titanium traditionally has been added to iron-based alloys to improve oxidation resistance. Therefore the titanium-oxygen binary phase diagram can be seen in Figure 11. When looking at the titanium rich side of the diagram, it can be seen that there are several phases that could be present at lower temperatures. Phases such as Ti_3O, Ti_2O, α-TiO, β-TiO, $Ti_{1-x}O$, and β-Ti_2O_3 some phases that could form. Probably the most commonly seen titanium oxide is rutile (TiO_2), which is a line compound with a composition of 40wt%O.

Ti-S Equilibrium Phase Diagram[37]

Although the Ti-O equilibrium phase diagram has been studied in some detail, not much work has been done on the titanium-sulfur binary phase diagram. The published Ti-S equilibrium phase diagram can be seen in Figure 12, but it should be noted that the equilibrium coexistence lines between phases are very uncertain. It is noted in the literature that the solid lines shown on the diagram are to enhance clarity rather than indicate a definitive phase boundary. Although the exact phase boundaries are unknown, the stable phases that have experimentally been observed at lower temperatures can still be seen. Some of these phases include Ti_6S, Ti_3S, Ti_2S, TiS, Ti_8S_9, TiS_2, and TiS_3, but other non-stoichiometric phases can be seen between 47-54wt%S.

1.3.2.2 Phase Stability Diagrams

Phase stability diagrams serve a similar purpose to equilibrium phase diagrams, as they show what phases are stable in a specific isothermal environment. Phase stability diagrams are used primarily for gaseous environments because they plot phases with respect to partial pressures of reactive species. Stability diagrams are typically two-dimensional, isothermal diagrams that can plot the stable phases for one metallic element and two reactive elements. Typically, two-dimensional phase stability diagrams for pure elements are used because they are

easiest to interpret and can be superimposed to show possible phases that may be present for alloys. Three-dimensional phase stability diagrams for binary alloys may be more representative of binary systems, but are difficult to construct and interpret. Phase stability diagrams for multicomponent alloys are currently being explored through the use of the Thermo-Calc computer program[38]. Producing multicomponent alloy phase stability diagrams would be very beneficial as they would be the most representative diagrams obtainable for alloys in corrosive environments.

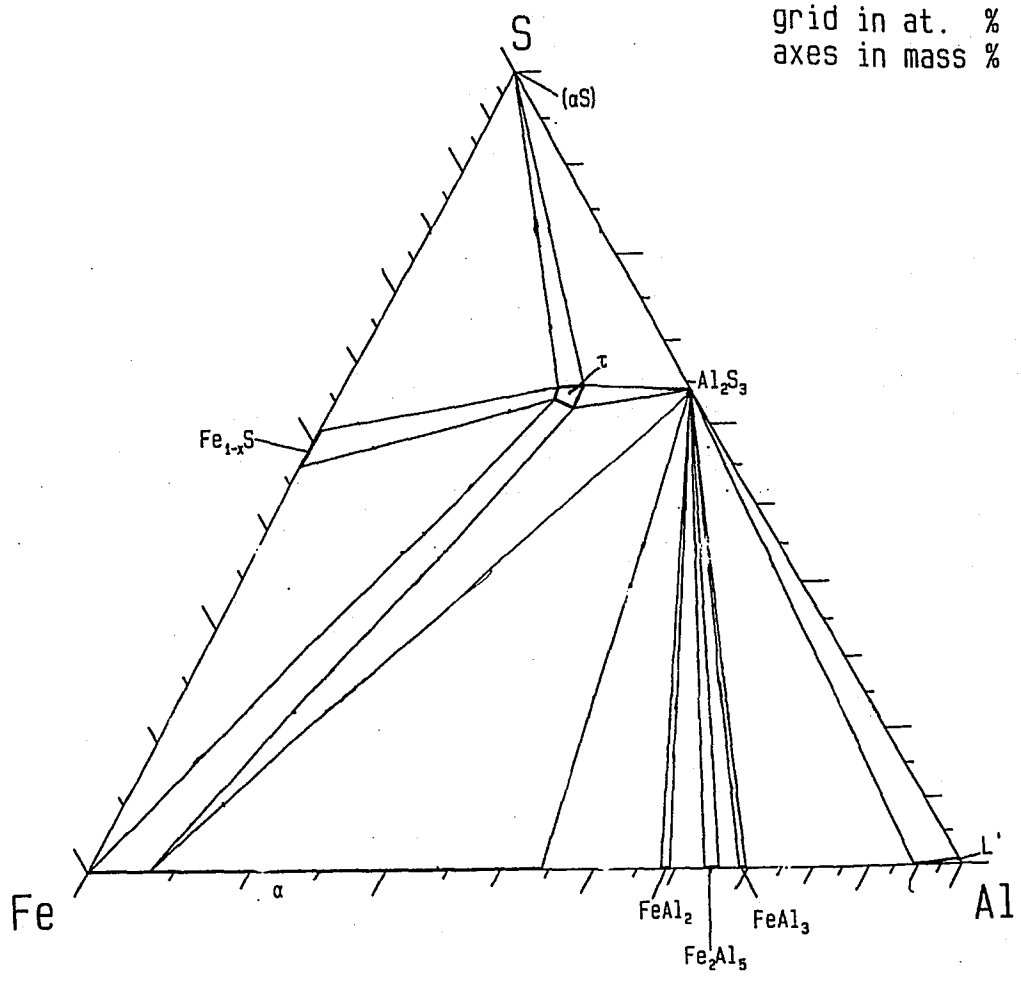

Figure 8 – Fe-Al-S Equilibrium Phase Diagram[33]

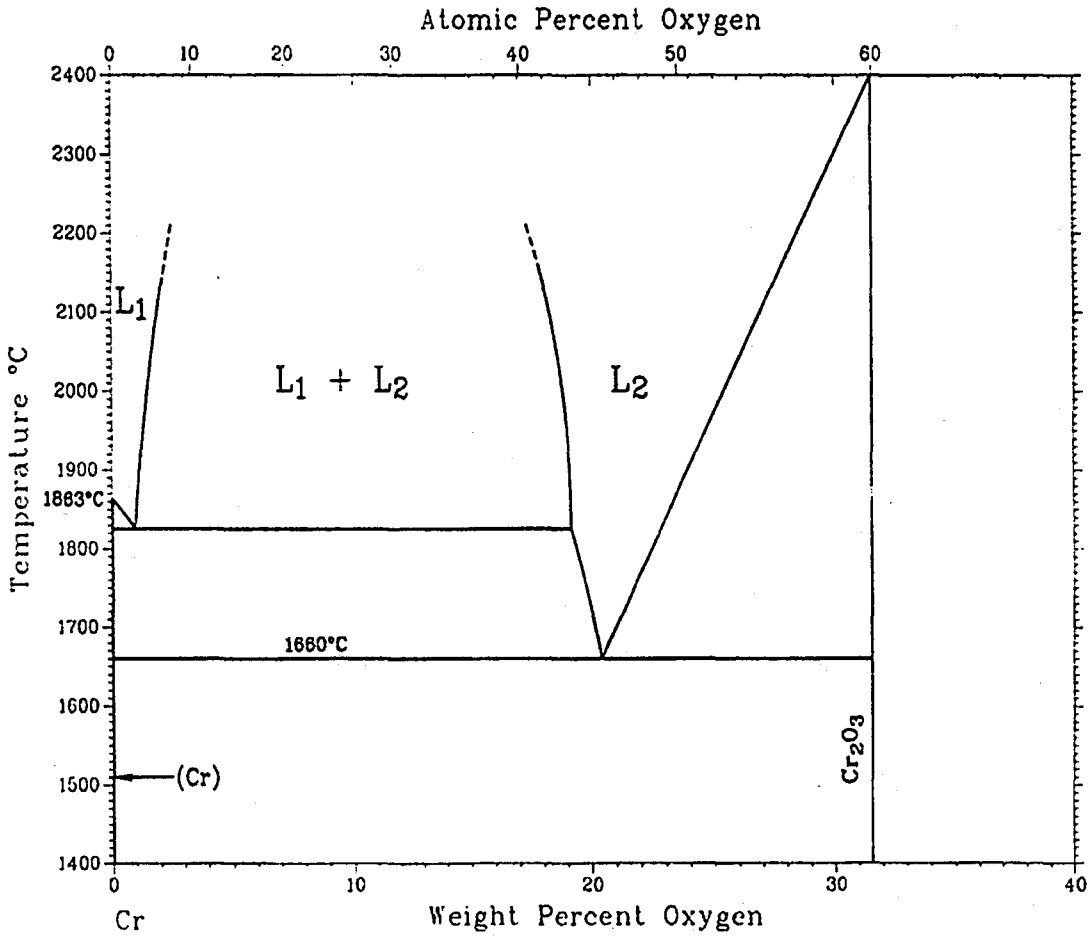

Figure 9 – Cr-O Equilibrium Phase Diagram[34]

Two-dimensional phase stability diagrams can be constructed using the software program HSC Chemistry for Windows[39]. Stability diagrams can also be constructed by plotting the equilibrium coexistence lines between two condensed phases using equilibrium equations. A general equilibrium equation can be written as:

$$4MS + 3O_2 = 2M_2O_3 + 2S_2 \quad (2)$$

The activities of the condensed phases (a_{MS}, a_{M2O3}) and the partial pressures of the gaseous phases (Po_2, Ps_2) can then be used to create the equation:

$$K = \frac{(a_{MS})^4 * (Ps_2)^2}{(a_{M2S3})^2 * (Po_2)^3} \quad (3)$$

where K is an equilibrium constant. If the assumption that the condensed phases are in their standard states is made, the activities are equal to one and equation (3) simplifies to:

$$K = \frac{(Ps_2)^2}{(Po_2)^3} \quad (4)$$

The total free energy of the reaction (ΔG) is then given with respect to K as:

$$\Delta G = -RT * \ln(K) \quad (5)$$

where R is the universal gas constant and T is the absolute temperature. Equation (5) can then be rearranged in terms of K so that it is given with respect to known values (ΔG, R, and T):

$$K = \exp(-\Delta G/RT) \quad (6)$$

Equation (6) can then be substituted into equation (4) and rearranged to obtain an expression for Ps_2 in terms of Po_2:

$$Ps_2 = \exp(-\Delta G/RT) * (Po_2)^{3/2} \quad (7)$$

This expression can then be used to obtain the phase stability diagram for the two condensed phases. Some important phase stability diagrams are briefly discussed in the next section.

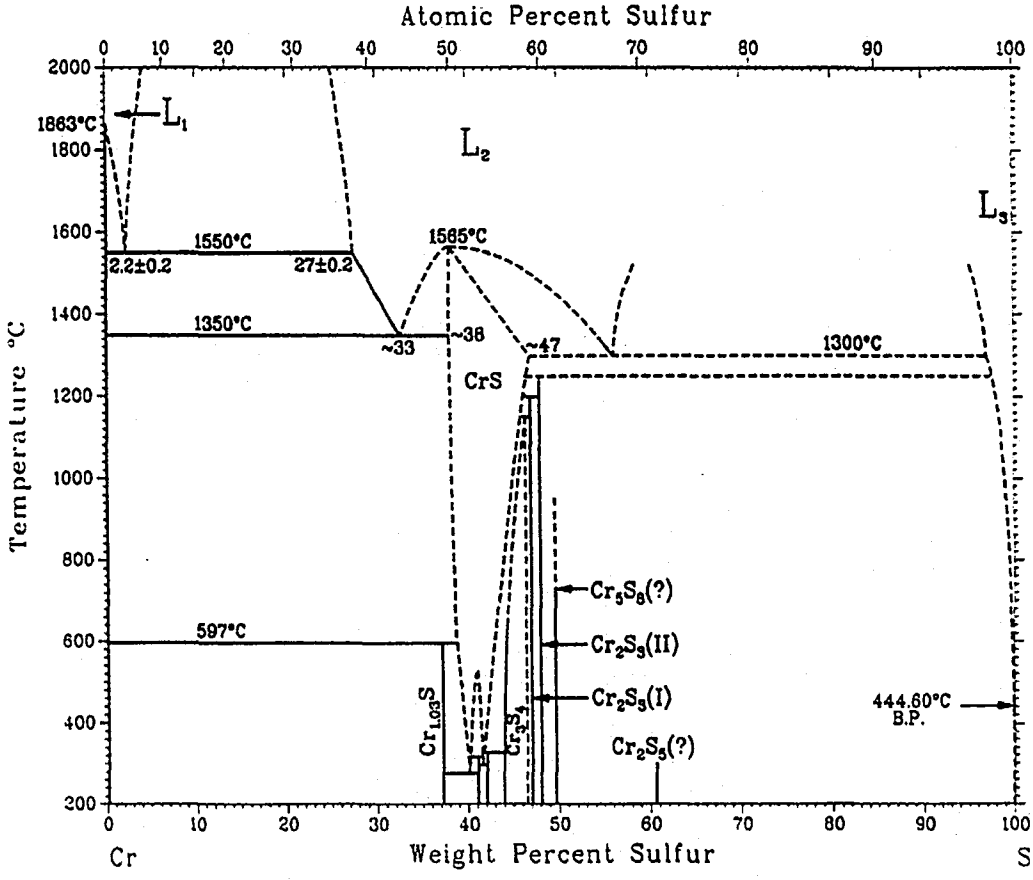

Figure 10 – Cr-S Equilibrium Phase Diagram[35]

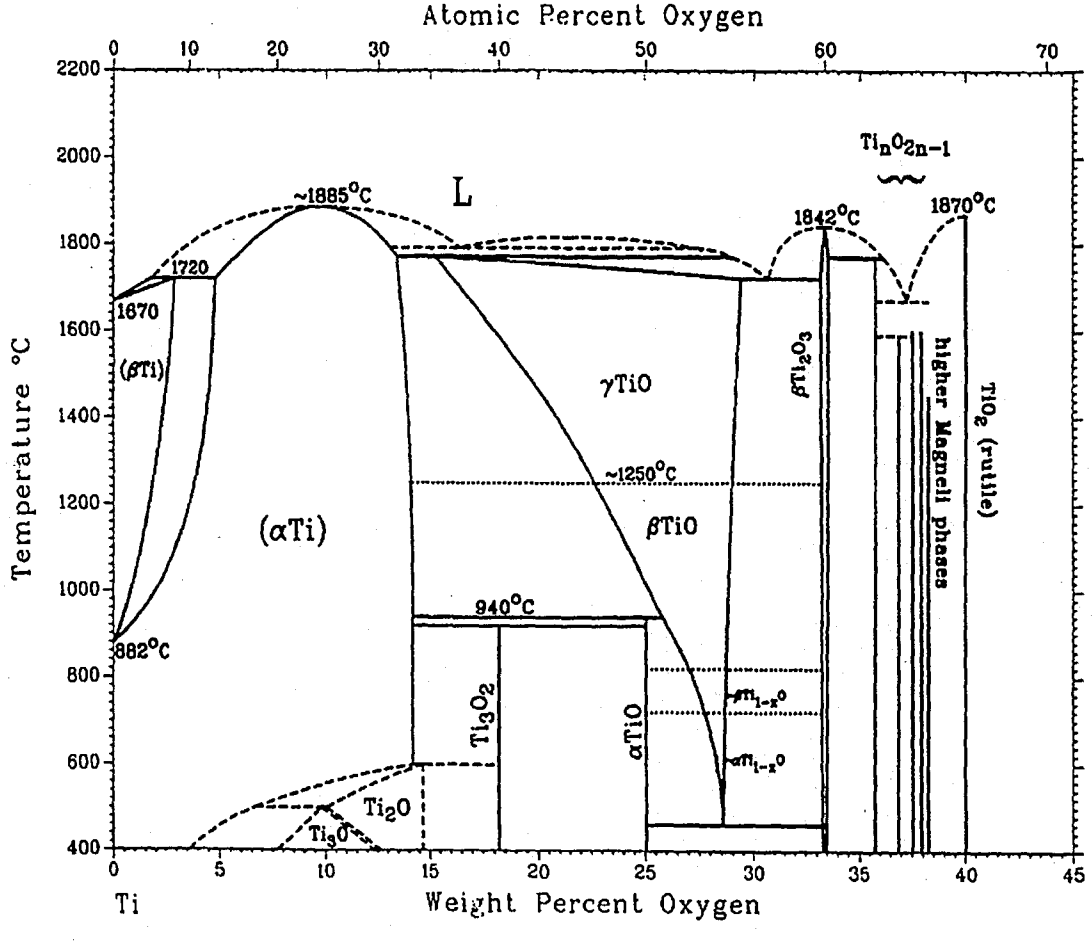

Figure 11 – Ti-O Equilibrium Phase Diagram[36]

Fe-O-S Phase Stability Diagram[39]

Considering the Fe-O and Fe-S equilibrium phase diagrams, there are a number of phases that could possibly be present at furnace temperatures. Overall, the phases that could be present include $Fe_{1-\delta}O$, Fe_3O_4, Fe_2O_3, FeS, $Fe_{1-\delta}S$, and FeS_2. In order to determine what phases will likely be seen in the furnace environment, a phase stability diagram can be constructed for the Fe-O-S system. The Fe-O-S phase stability diagram at 500°C can be seen in Figure 13. It can be seen from this diagram that at a high oxygen partial pressure and low sulfur partial pressure, $Fe_{1-\delta}O$ and Fe_3O_4 can be present (depending on the overall partial pressure of oxygen). On the other hand, as the sulfur partial pressure increases and the oxygen partial pressure decreases, $Fe_{1-\delta}S$ becomes the dominant phase. At a very high oxygen partial pressure Fe_2O_3 is stable, whereas at very high sulfur partial pressure the environment is sulfidizing and FeS_2 is stable. It is important to note that the sulfates $FeSO_4$ and $Fe_2(SO_4)_3$ are stable at high oxygen and high sulfur partial pressures.

Al-O-S Phase Stability Diagram[39]

It is important to comment on the stability of Al_2O_3 over Al_2S_3 in mixed oxidation/sulfidation environments. Aluminum's affinity for oxygen in higher than it's affinity for sulfur, so Al_2O_3 is stable instead of Al_2S_3 even to very high sulfur and low oxygen partial pressures[40]. This can clearly be seen in the Al-O-S phase stability diagram shown in Figure 14. As can be seen by this diagram, Al_2O_3 will be the stable phase in a mixed environment up until there is almost a purely sulfidizing environment. Although Al_2O_3 is the stable phase in these environments, it is a slow forming scale and if sulfides are present they may outgrow and consume the Al_2O_3 phase. Again it is important to note the aluminum sulfate, $Al_2(SO_4)_3$, is stable at high oxygen and sulfur partial pressures.

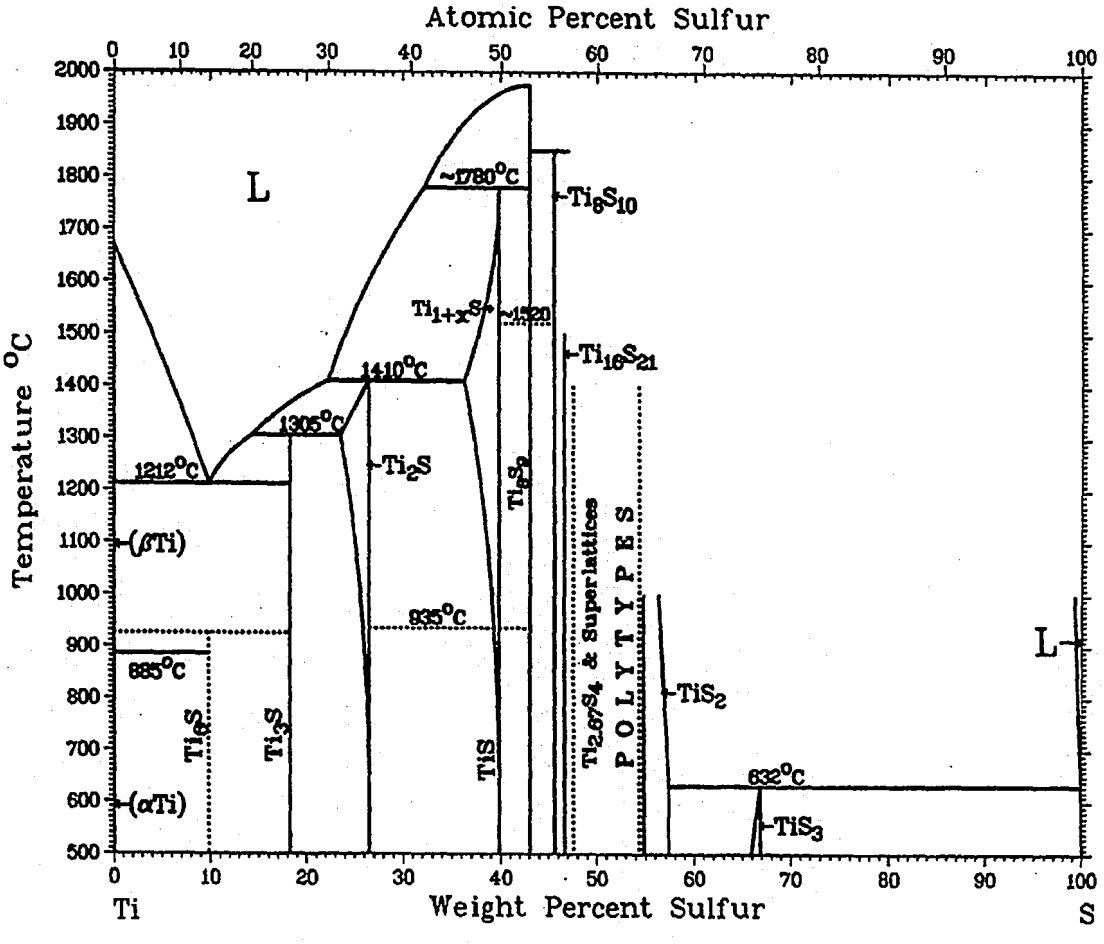

Figure 12 – Ti-S Equilibrium Phase Diagram[37]

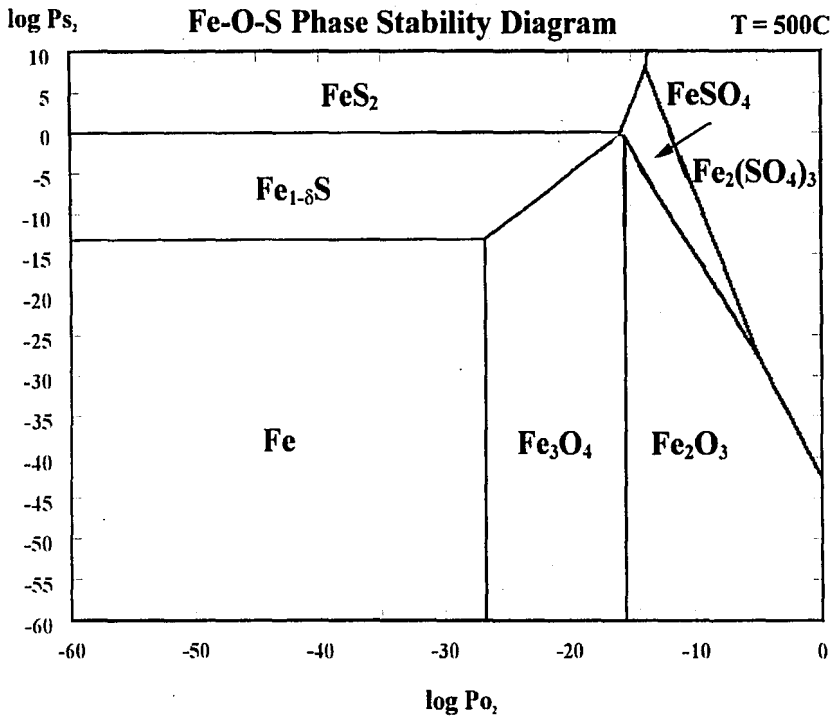

Figure 13 – Fe-O-S Phase Stability Diagram[39]

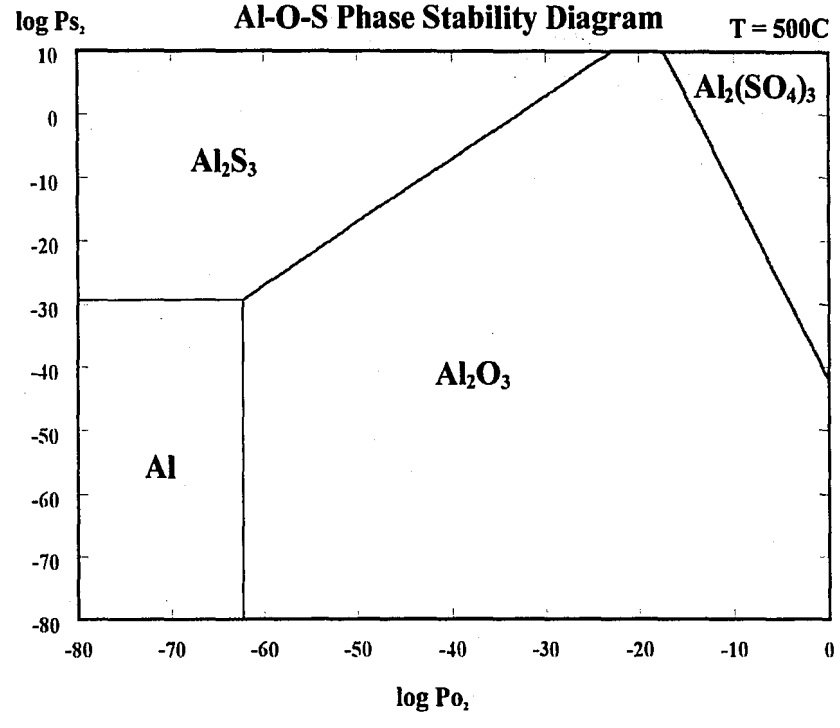

Figure 14 – Al-O-S Phase Stability Diagram[39]

Cr-O-S Phase Stability Diagram

The Cr-O-S phase stability diagram at 500°C can be seen in Figure 15. As can be seen by the diagram, various phases can be stable depending on the environment. At high sulfur pressures sulfides, such as CrS or Cr_2S_3, can be stable. On the other hand, at high oxygen partial pressures, chromium oxides, such as Cr_2O_3 and CrO_2, are the stable phases. Again at high oxygen and sulfur partial pressures the sulfate $Cr_2(SO_4)_3$ is the stable phase.

Ti-O-S Phase Stability Diagram

The Ti-O-S phase stability diagram at 500°C can be seen in Figure 16. It can be seen from this figure that there are several titanium sulfides that can be stable at high sulfur partial pressures and low oxygen partial pressures. Some of these stable titanium sulfide phases at 500°C are TiS, $TiS_{1-\delta}$, TiS_2, and TiS_3. On the other hand, at higher oxygen partial pressures and lower sulfur partial pressures there are several titanium oxides that are stable. These include TiO, Ti_2O_3, Ti_4O_7, and TiO_2.

Although thermodynamics may determine the oxide phases that could possibly be present, it alone cannot fully predict what may be present. Thermodynamically, multiple oxides may be stable at a certain temperature and composition, but only one oxide may be seen. This could occur if one oxide overgrows a second oxide and prevents rapid diffusion or if the oxide that forms has macroscopic cracks and another oxide can form within the cracks. There would be no way to predict this type of behavior from thermodynamics alone because thermodynamics gives no information about how fast each oxide will grow. In order to better predict the scales that may form during high temperature corrosion, kinetics of the system must also be incorporated.

1.3.3 Kinetics

Kinetics describes the rate at which a phase will form and grow. Kinetic data can be obtained roughly through measuring scale thickness after a certain exposure time. The thickness of the scale can be compared to the time of exposure to find a corrosion rate. A more accurate method to find kinetic data is to measure the weight change versus time of exposure. Usually, when considering high temperature corrosion, kinetic data is best obtained using a thermogravimetric balance. This plots the weight change of the sample versus time at specific conditions. For most materials, an increase in weight occurs during oxidation (or sulfidation) due to the metal absorbing the reactive gas and forming a scale on the surface of the material. A decrease in weight can be interpreted either as the scale separating from the substrate, known as spallation, or as a volatile reaction product evaporating. In the present case of an iron-aluminum alloy exposed to oxygen and sulfur, a weight loss can be interpreted as spallation because a volatile product is unlikely at the boiler temperatures. Because the amount of oxide is related to the weight gain of the sample, the corrosion rate can be found from these plots as the weight change over time. Generally, the corrosion rate of the material will determine by the slope of the curve.

The rate at which an oxide will grow is primarily based on the barrier between the reactive gas and the metal substrate. The corrosion rate depends on the rate-limiting step of the reaction. If the metal and gas are in direct contact with one another, the corrosion rate will be relatively constant and the oxide will grow directly with time. If a continuous, dense, and uniform oxide scale is present between the metal and gas, the corrosion rate will be fast initially and then decrease as the scale thickness increases. Taking this approach, the rate of corrosion can be generalized into three types: linear, parabolic, and logarithmic.

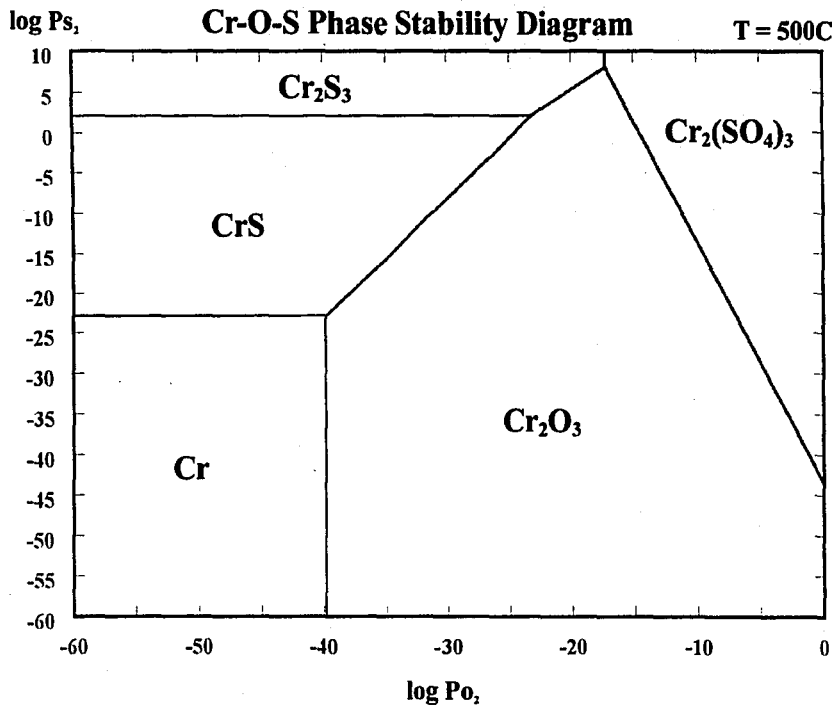

Figure 15 – Cr-O-S Phase Stability Diagram[39]

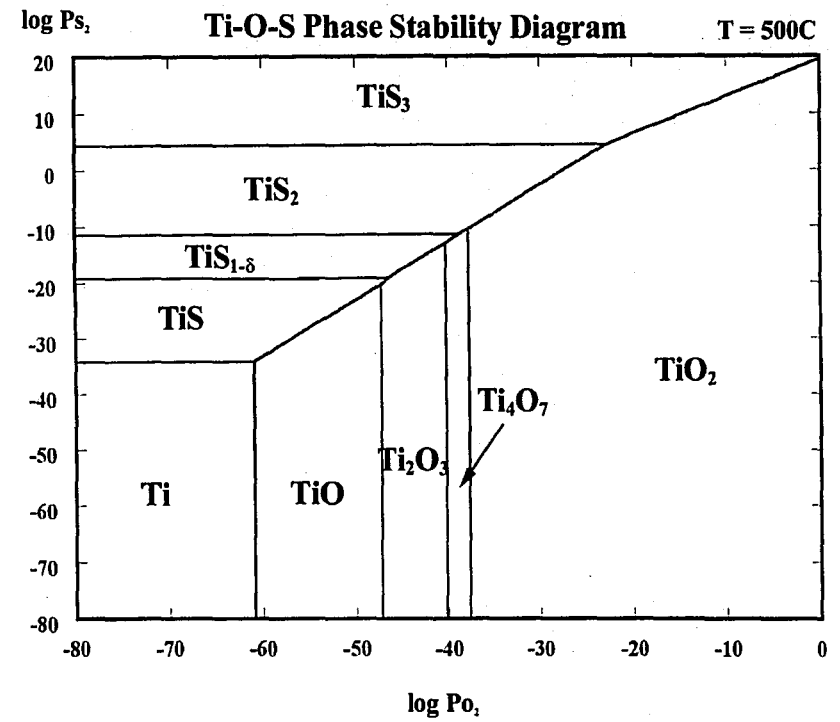

Figure 16 – Ti-O-S Phase Stability Diagram[39].

As mentioned above, if the metal and reactive gases are in direct contact with one another, the corrosion rate is constant. This means that the weight gain of the sample will increase linearly with time. This can be represented by the general equation:

$$w = k_l(t) + C \tag{8}$$

where w is the weight gain per area, t is time, k_l is the linear rate constant, and C is an integration constant. This type of corrosion can be considered to follow linear kinetics and an example of weight gain corresponding to linear scale growth can be seen in Figure 17. Linear growth kinetics are typically seen at the beginning of oxidation where a uniform scale has yet to form and completely cover the sample. This type of growth kinetics can also sometimes be seen if the scale is non-adherent and spalls, if a sufficient amount of cracks or macroscopic defects are present in the scale, or if the oxide scale is porous. Generally, when there is direct contact between metal and gas, linear kinetics can be expected.

Assuming a uniform, continuous, and dense scale completely surrounds the metal substrate, diffusion through the scale will be the rate-limiting step. As the scale increases in thickness the corrosion rate will decrease because ions have farther to diffuse through the scale. This type of corrosion is considered to follow the parabolic rate law, which can be represented as:

$$w^2 = k_p(t) + C \tag{9}$$

where k_p is the parabolic rate constant. An example of parabolic scale growth can also be seen in Figure 17. Note that equation (9) is in a similar form as a solution to Fick's second law for diffusion:

$$X^2 = Dt \tag{10}$$

where X is distance, D is the diffusivity, and t is time. Comparing these equations helps to show that diffusion is a limiting step during corrosion that follows the parabolic rate.

The third type of corrosion kinetics that is observed occurs when a protective scale forms after a short amount of time and drastically reduces the corrosion rate. This type of oxidation is considered to follow the logarithmic rate law, which can be mathematically represented as:

$$w = k_e * \log (Ct + A) \quad (11)$$

where k_e is the logarithmic rate constant and A is a constant. Logarithmic scale growth behavior can be seen again in Figure 17 as well. This type of corrosion behavior provides the best protection during oxidation of metals. The oxidation rate is fast initially until a continuous, protective scale can form and prevent rapid diffusion of metal cations or reactive gas anions. Typically, logarithmic kinetics are seen at low temperature exposures and therefore are not usually observed at high temperatures unless a passive oxide forms and successfully protects the underlying alloy. Although these three types of corrosion kinetics can be identified as described, usually two or more of these types of kinetics can be seen during oxidation.

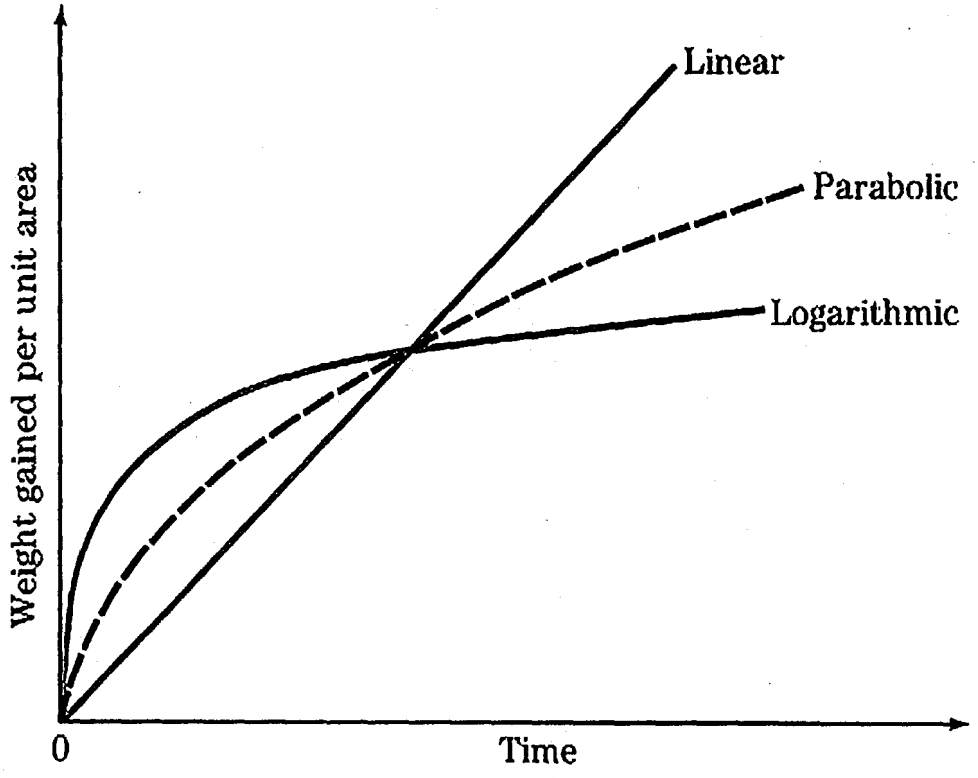

Figure 17 – General Corrosion Rates[41]

As can be seen above, at high temperatures diffusion through the oxide scale is typically the rate-limiting step for oxidation. Diffusion is temperature dependent, so the rate of scale growth can be related to temperature. Increasing the temperature will increase the diffusion rate of the ions through a scale due to an increase in thermal energy[42]. This can be shown using an Arrhenius equation:

$$k \propto \exp[-Q/RT] \qquad (12)$$

where k is the rate constant, Q is the activation energy, R is the universal gas constant and T is the absolute temperature. A graph can be constructed using the rate constant and the absolute temperature by plotting ln k vs. (1/T). The slope of the line will be equal to –Q/R, so the

activation energy can be found for the reaction. As long as the amount of macroscopic defects is limited, the activation energy can be related to the limiting step of the reaction. In most cases, the rate-limiting step will be the scale that forms during oxidation. Therefore, the type and morphology of scales present are very important and will be discussed next.

1.3.4 Scale Type and Morphology

A main contributor to the corrosion protection of an alloy is the type of scale that forms and it's morphology during the reactions between the alloying elements and the reactive gases. Ideally on a pure metal substrate with one reactive gas, one uniform scale will form across the entire substrate. Most metals oxidize and sulfidize by cation transportation through the scale[43]. Therefore, in this ideal situation the scale will grow away from the substrate, known as external oxidation.

Unfortunately, most metals do not form protective single layer scales. Instead most metals and alloys will form two- or multilayered scales during oxidation (Figure 18a). During the initial stage of oxidation, the scales that form are relatively flat and thin. Upon prolonged oxidation, between the primary oxide layer and the metal substrate, a porous inner layer of the primary oxide can form due to outward metal cation transport (Figure 18b). An alloy with multiple oxidizing alloy components can form various oxide phases. If the oxide of the alloy component A and the oxide of alloy component B are completely miscible, one oxide containing both elements (ABO_x) can form (Figure 18c). On the other hand, if there is no mutual solubility between the oxide of element A and the oxide of element B, selective oxidation of one element can occur. Selective oxidation occurs when one element forms a continuous oxide layer and the other remains passive (Figure 18d). Multiple oxide layers could still be seen during selective oxidation as oxide phases of various stoichiometric ratios. For example, iron can selectively oxidize and form FeO, Fe_2O_3, and Fe_3O_4[44].

Internal oxidation of an element could also occur in alloys and increase the overall oxidation rate. If the partial pressure of the reactive species is too low to form an oxide of element A, but is high enough to form an oxide of element B, internal oxidation of element B will occur. Internal oxidation can also occur if oxygen anions are able to diffuse through a porous scale of element A and reach an A-depleted substrate, where internal oxidation of element B can occur. During internal oxidation, oxide precipitates nucleate either at the scale-metal interface or within the metal matrix. These precipitates are commonly spherical or shaped as plates. A schematic representation of internal oxidation can be seen in Figure 19.

Equations describing the internal oxidation phenomena have been proposed a number of years ago by Wagner[45]. In this classic work Wagner used copper, iron, and zinc samples to derive general internal oxidation equations that can be applied to a large number of metals. Wagner assumed for internal oxidation to occur at a distance δ from the metal surface, the inward flux of oxygen molecules (j_{O_2}) must be equal to the outward flux of metal atoms (j_{m_e}) and can be written as:

$$j_{Me} = \frac{D_{Me} P^{\circ}_{Me}}{\delta * RT} = \frac{2}{v} j_{O_2} = \frac{2 D_{O_2} P^{\circ}_{O_2}}{v(\Delta - \delta) RT} \qquad (13)$$

where v is the number of oxygen atoms reacting with one metal atom when forming the oxide, D_{Me} and D_{O_2} are the diffusivities of the metal and oxygen molecules, respectively, P°_{Me} is the metal vapor pressure at the metal surface, $P^{\circ}_{O_2}$ is the oxygen partial pressure of the atmosphere, and Δ is the effective thickness of the diffusion boundary layer.

Assuming that $D_{Me} \cong D_{O_2}$, $P^{\circ}_{O_2} >> P^{\circ}_{Me}$, and that $\delta << \Delta$ (indicating that the internal oxidation occurs in the region directly adjacent to the metal surface) the critical oxygen partial pressure $P^{\circ}_{O_2}$ (critical) required for internal oxidation to occur can be written as:

$$P^{\circ}_{O_2}(critical) \leq \frac{v\Delta P^{\circ}_{Me}(RT)^{1/2}}{2D_{O_2}(2\pi M_{Me})^{1/2}} \qquad (14)$$

where M_{Me} is the atomic weight of the metal.

When $P^{\circ}o_2$ is greater than $P^{\circ}o_2$ (critical), the internal oxidation mechanism no longer governs the formation of internal oxide particles. Instead the oxygen partial pressure is high enough to form a uniform protective oxide layer on the surface of the metal. Therefore, Equation 14 can be used to find the oxygen partial pressure required to prevent unwanted internal oxidation and promote the formation of a passive oxide layer.

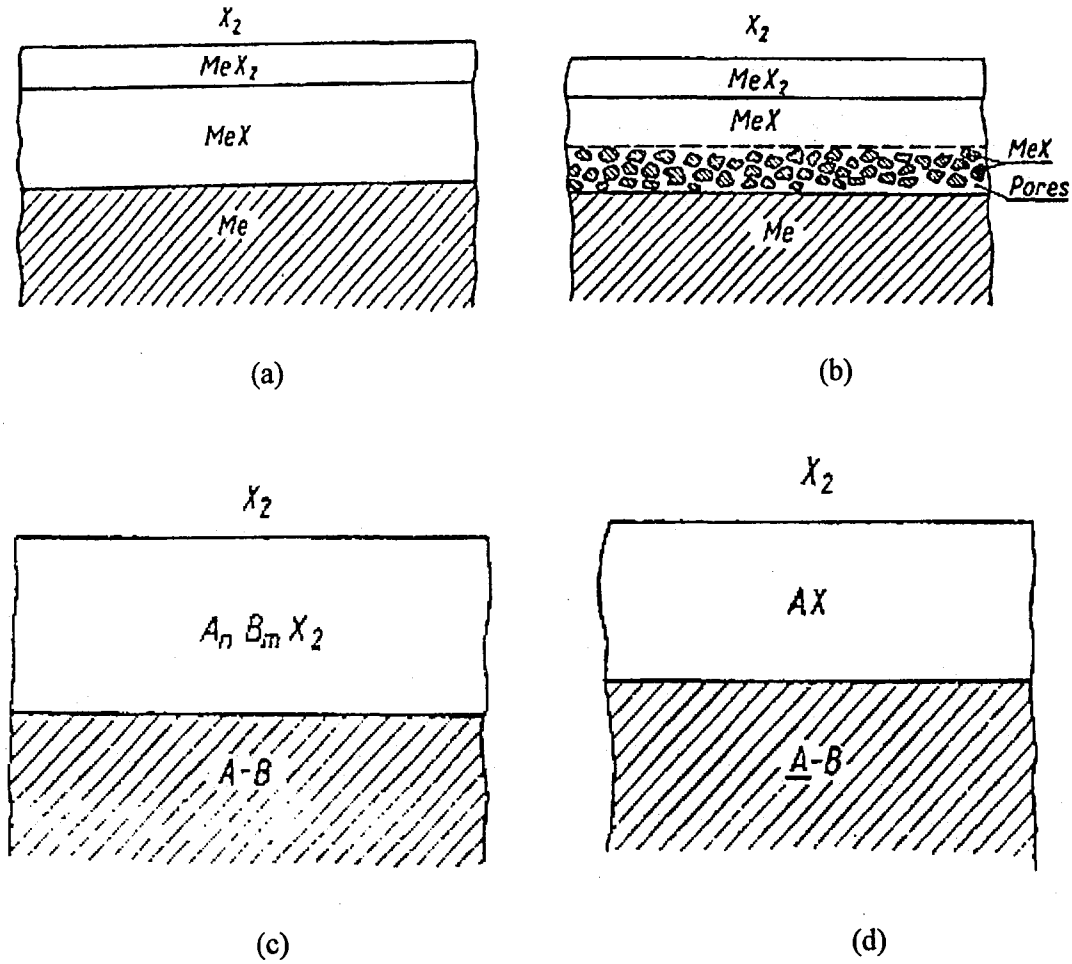

Figure 18 – Various types of scales including an example of a multilayered scale (a), a multilayered scale after long oxidation time where a porous inner layer is present (b), a completely miscible oxide layer (c), and selective oxidation of element A (d)[46].

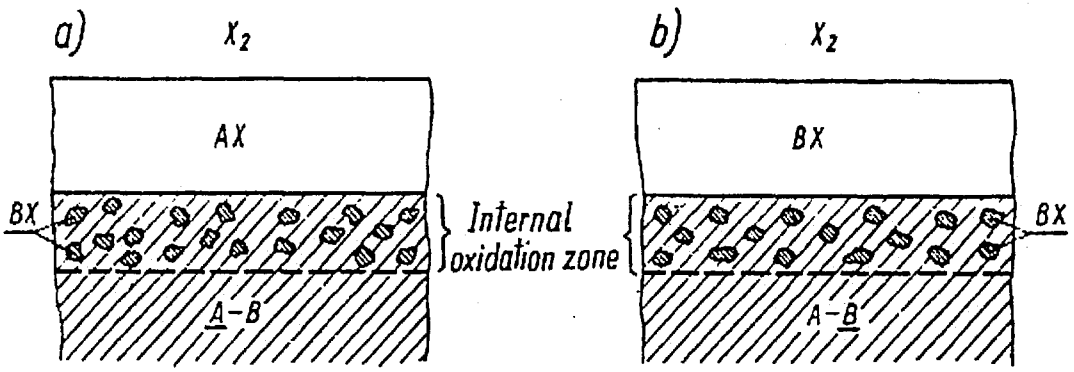

Figure 19 – Schematic representation of internal oxidation of element A (a) and B (b)[46].

Another scale morphology that is commonly seen in both oxidizing and sulfidizing environments is a uniform scale with nodules growing at selective spots across the scale. Typically, nodules can form when a macroscopic defect is present in the scale, such as a crack, or they can selectively oxidize at the onset of exposure and continue to grow as a continuous scale forms around it. The growth of nodules can also increase the overall corrosion rate of the alloy as faster growing oxides can overgrow the protective scale and allow for rapid diffusion and growth of the external scale. The formation of nodules on iron-aluminum alloys during initial stages of oxidation was described in detail by Tomaszewicz and Wallwork and can be seen schematically in Figure 20[47]. This explanation holds only for oxidation and if there is enough aluminum to form a continuous Al_2O_3 scale. The process begins with the initial stages of oxidation, when alumina (Al_2O_3) and iron oxides (FeO) simultaneously nucleate at the surface of the sample (Figure 20a). The alumina continues to form until a uniform Al_2O_3 layer almost completely covers the sample, while the iron oxide nodules remain at random sites and continue to grow into the alloy (Figure 20b). The FeO nodules continue to grow outward from the alloy and form various iron-oxide species (Figure 20c). At the nodule-alloy interface the alumina reacts with the FeO to form the spinel $FeAl_2O_4$, while the iron continues to oxidize into Fe_3O_4 and Fe_2O_3 at the nodule-gas interface. Internal oxidation continues through the nodules and alumina becomes

more stable at the nodule-alloy interface where the oxygen partial pressure is very low (Figure 20d and e). Finally, the oxygen partitial pressure can become too low at the nodule-alloy interface to form any iron-oxide compounds so a continuous layer of Al_2O_3 can form at the base of the nodule to prevent any further nodule growth (Figure 20f).

Another proposed explanation for the formation of nodules was given by Banovic et. al.[48]. This alternative explanation, shown in Figure 21, considers nodules that form after a protective alumina layer has already formed on the alloy. The process begins with the continuous passive alumina layer forming on the alloy, keeping reactive oxygen or sulfur gases from reaching the metal (Figure 21a). During further exposure, the passive Al_2O_3 layer breaks down either by cracks forming through the protective layer due to scale stresses or through fast diffusion pathways such as grain boundaries (Figure 21b). Once the passive layer breaks down, the reactive gases can travel through the cracks and come in direct contact with the alloy. If the alloy cannot reform the passive layer fast enough, iron-rich oxides can form rapidly and grow both inward and outward form the metal substrate (Figure 21c). Eventually, these nodules can meet up and overgrow the protective Al_2O_3 layer forming a thick non-protective corrosion scale (Figure 21d).

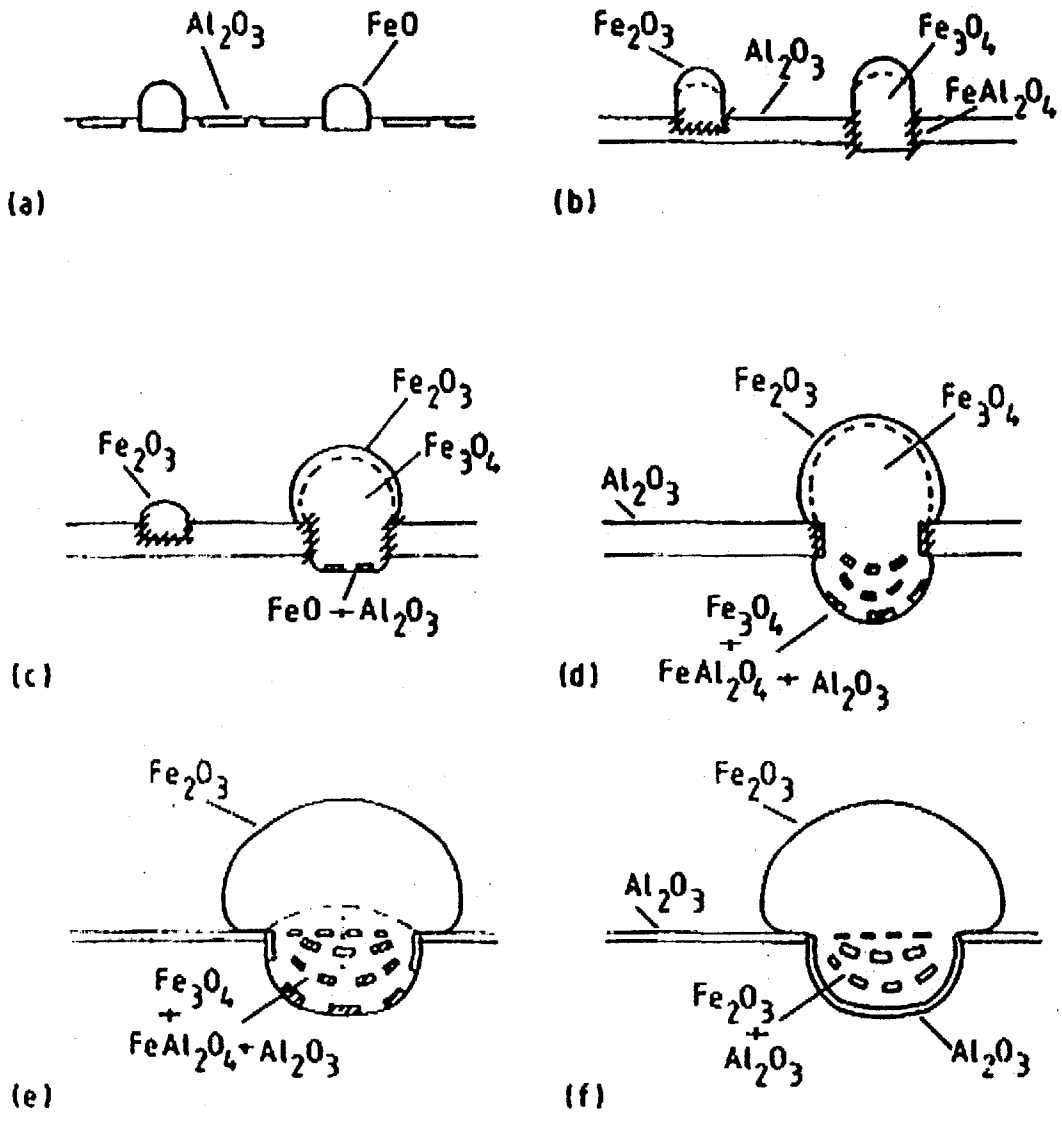

Figure 20 – Schematic of nodule formation and growth[47].

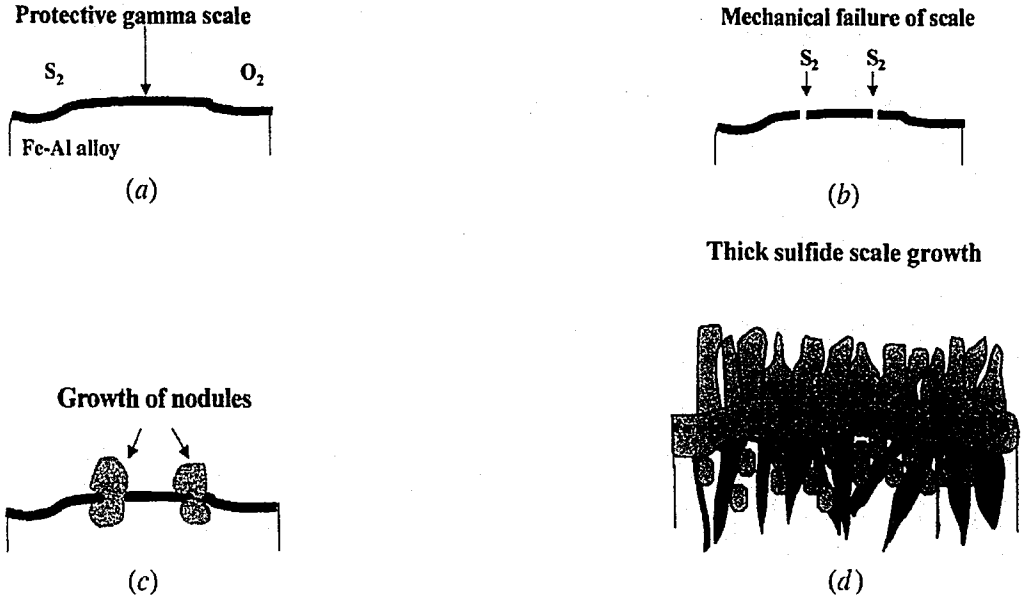

Figure 21 – Schematic of passive layer breakdown and subsequent nodule growth[48].

1.3.5 Summary

There are many factors that effect the high temperature corrosion resistance of an alloy. Diffusion plays an important role during high temperature corrosion. Once an initial scale covers the substrate, the oxide grows by ion diffusion through the scale. Thermodynamics are also important to consider during corrosion studies. Equilibrium phase diagrams can be used to predict all the possible phases that could be present during corrosion. Phase stability diagrams can also be used to determine which phases are stable in a specific gaseous environment. Kinetics should also be used along with thermodynamics to determine how rapidly phases form. Corrosion rates can be determined using a thermogravimetric balance. The activation energy can be calculated and used to determine if the rate-limiting step changed. Although thermodynamics and kinetics give a lot of information about a system, the scale that forms is a very important aspect to corrosion. A single layered uniform, dense, compact scale is ideal, but rarely occurs. Usually, multilayer scales form on alloys and can have complex morphologies. Internal oxidation

and nodule growth can increase the corrosion rate of the alloy as well. Now that the important aspects of corrosion have been reviewed, the corrosion behavior iron-aluminum alloys will be discussed in the following section.

1.4 Corrosion Literature

Corrosion resistant materials have been under investigation as coatings for waterwall tubes since the retrofitting of burners in Low NOx furnaces. Although various materials such as Inconel alloys, stainless steels, and FeCrAl alloys have been used as coatings for the boiler tubes, iron-aluminum alloys have received a great deal of attention. The main attraction of iron-aluminum alloys is that they demonstrate excellent corrosion resistance in furnace atmospheres and they are also less expensive than the other candidate materials because they use aluminum as the critical element rather than chromium or nickel[4]. Alloy development has produced binary iron-aluminum alloys that show excellent corrosion properties[3]. Attempts to increase the corrosion resistance of iron-aluminum alloys are being made by the additions of ternary elements[6]. This section will review the alloy development process from pure iron, to binary iron-aluminum alloys, and finally to iron-aluminum alloys with ternary additions.

1.4.1 Pure Iron Oxidation and Sulfidation

Although oxidation and sulfidation are governed by the same mechanisms, oxidation and sulfidation rates of pure iron are very different. At a given temperature, the sulfidation rate for pure iron is much higher than the oxidation rate for pure iron. The difference in corrosion rates can be attributed to the scales that form in each environment[18]. Typically, sulfides have a much higher defect concentration than oxides, which allows for more rapid diffusion of ions through the scale[18].

The oxidation performance of pure iron has been studied extensively for many years over a wide temperature range[49,50]. Saegusa and Lee studied the oxidation behavior of pure iron between 500-700°C[44]. They found that two types of scales can be seen over this temperature range. Below 600°C, a uniform single layer scale of Fe_3O_4 was present across the specimen. On the other hand, above 600°C, a duplex scale was present consisting of both $Fe_{1-\delta}O$ and Fe_3O_4. They attributed this scale change on the instability of wustite ($Fe_{1-\delta}O$) at 570°C. Above 570°C, wustite is stable with Fe_3O_4 and therefore a duplex scale can form, whereas below 570°C wustite becomes unstable and transforms into Fe_3O_4.

The sulfidation of pure iron has also been studied in a large extent[42,51,52]. In a purely sulfidizing environment, scales that form could be either single layer or duplex iron-sulfide scales[42]. Strafford and Manifold found that at short exposure times a large grained single layer of porous sulfide formed[42]. At longer exposure times, they found that a duplex layer formed, where the outer layer consisted of large grains and the inner layer was comprised of small grains. The growth of the inner layer was reported to initiate at stress concentrations such as corners and then completely cover the sample at longer exposures. This is consistent with results of Meussner and Birchenall who proposed that the large grained outer iron sulfide scale grows epitaxially from the inner scale, which is comprised of small grained sulfides[52]. The sulfidation rate of iron increases with an increase in the partial pressures of either H_2S or S_2, as well as an increase in temperature[51].

1.4.2 Iron-Aluminum Alloys: Oxidation

When reviewing the literature for the oxidation of binary iron-aluminum alloys, it is easiest to begin at low aluminum concentrations and move into alloys with high aluminum contents. Also, gaseous corrosion will exclusively be discussed as little literature has been published on slag corrosion in these environments. When considering iron-aluminum alloys with

low concentrations of aluminum, Saegusa and Lee oxidized binary iron-aluminum alloys from 0-5wt%Al[44]. They found that 1wt%Al slightly improved the oxidation resistance of iron, but aluminum concentrations greater than 1wt%Al improved the oxidation resistance of iron dramatically. It was also seen that at a given temperature, the overall oxidation decreased with increasing aluminum content[30,44].

At lower temperatures (500-700°C) the increase in oxidation resistance was attributed to a duplex scale where the inner scale consisted of a mix of both iron and aluminum oxides[30]. Between 700-900°C, multilayered scales were found to completely cover the samples. At low aluminum contents, two layers formed and at higher aluminum contents, three layers formed. For the two layer scales, the outer layer was found to be iron rich whereas the inner layer was aluminum rich. Scales with three layers showed that the outermost scale was Fe_2O_3, the middle scale consisted of Fe_3O_4, and the inner scale was comprised of the spinel $FeAl_2O_4$[30]. Over this higher temperature range, the limiting step to oxidation was diffusion through the inner layer of $FeAl_2O_4$. At even higher temperatures (900°C) iron oxide nodule growth was seen sporadically across the surface of the specimen. The formation of the nodules was attributed to simultaneous internal and external oxidation at highly stressed areas, due to the tendency for them to form at corners or edges[30].

Increasing the aluminum content in these alloys has resulted in an increase in oxidation protection. Although at 800°C iron oxide nodules can be seen up to around 7wt%Al, the area covered by these nodules decreases with increasing aluminum content[53]. Tomaszewicz and Wallwork found that an alloy with 2.5wt%Al, oxidized at 800°C, resulted in 50% of the surface covered by nodules. Between 3-7wt%Al, the specimen had few, randomly distributed nodules across the surface. Above 7wt%Al, no nodules could be seen after exposure at 800°C. The nodules formed during this study consisted primarily of Fe_2O_3 (sometimes with Fe_3O_4), with a thin layer of either $FeAl_2O_4$ or Al_2O_3 at the base of the nodules[53].

The minimum amount of aluminum needed to form a uniform, protective coating of Al_2O_3, known as the critical aluminum concentration, has been found to depend on temperature. In a review conducted by Tomaszewicz and Wallwork they summarized the proposed critical aluminum contents at different temperatures[54]. The value of critical aluminum content ranged from 5wt%Al at 1000°C to 12wt%Al at 600°C. A summary of reported critical aluminum concentrations by various authors is given in Table 1. Above 12wt%Al, binary iron-aluminum alloys form a protective Al_2O_3 scale that reduces the oxidation rate. The addition of aluminum above 12wt% provides the alloy with a higher abundance of aluminum to reform a protective scale if the Al_2O_3 scale cracks or spalls due to stresses generated within the sample. If the conditions are kept the same, the higher the aluminum concentration is within the alloy, the longer the service lifetime of the part[55].

Table 1 – Reported critical aluminum concentrations for oxidation protection.

Author	Temperature (°C)	Wt % Al
Tomaszewski and Wallwork[54]	600	12
Boggs[30]	600	10
Tomaszewski and Wallwork[53]	800	7.5
Wallwork and McGirr[56]	800	7.8

1.4.3 Iron-Aluminum Alloys: Sulfidation

The sulfidation resistance of iron improves with the addition of aluminum to the system[57,58]. Strafford and Manifold compared the sulfidation resistance of Fe–5wt%Al to that of pure iron[57]. They found that the sulfidation rate for pure iron is around ten times that of the alloy. The iron-aluminum alloy displayed parabolic kinetics during the initial stage of growth and then

followed linear kinetics during subsequent growth. The scale that formed during the initial stage of sulfidation was thin (~10μm) and consisted solely of FeS. During the stage where linear growth kinetics was observed, a duplex scale formed. The outer layer was comprised primarily of FeS, with a small amount of aluminum near the inner layer. The inner layer was found to be made up of FeS with small amounts of Al_2S_3[57].

When the aluminum concentration is increased even further to around 10-20wt%Al, the alloy demonstrates slower corrosion rates than that of 5wt%Al[58]. In a purely sulfidizing environment between 800-1000°C, the scales that form on the 10 and 20wt%Al alloy are very similar to those found on the 5wt%Al alloy. At short exposure times small nodules, made up of two layered scales, could be detected at stress concentrations. After longer exposure times, the nodules seemed to completely cover the sample as a duplex scale. Again, the outer layer consisted of FeS, while the inner layer was comprised of a fine dispersion of FeS and Al_2S_3[58]. Others found that on alloys with ~10wt%Al, the outer layer was comprised of FeS, but the inner layer was a mixture of FeS and $FeAl_2S_4$ where plates of Al_2S_3 and $FeAl_2S_4$ penetrated into the substrate[59]. Alloys with ~20wt%Al had the same outer and inner layers as the 10wt%Al alloy, but also formed continuous layers of $FeAl_2S_4$ and Al_2S_3, and plates from the Al_2S_3 layer penetrated into the substrate[59-62]. At temperatures below 750°C, it was found that alloys with aluminum contents greater than 10wt% provide relatively good sulfidation resistance[62].

Although the corrosion rates decrease when increasing the aluminum concentration, increasing the temperature counteracts the beneficial effects of higher amounts of aluminum. Strafford and Manifold proposed three possible reasons as to why the scales formed on alloys with high amounts of aluminum (10-20wt%Al) at high temperatures were not protective[58]. First, it has been shown that at high temperatures (900-1000°C) the amount of Al_2S_3 increased with increasing weight gain. Al_2S_3 has a high molecular volume and increasing the thickness of the scales creates more porosity within the scales, thus allowing more rapid diffusion and therefore

higher corrosion rates. Another possible reason deals with the amount of internal sulfidation that takes place during exposure. Large amounts of internal corrosion could be seen in alloys with high aluminum contents at high temperatures. A main contributor to the accelerated amount of internal sulfidation is the growth of Al_2S_3, which was seen to grow as "needles" into the substrate (evident in 20wt%Al alloy). The needles could contribute to developing small cracks in the substrate, increasing the paths for internal sulfidation. Finally, and most importantly, at high temperatures (>800°C) the reaction product Al_2S_3 allows for rapid ionic diffusion due to its low melting point of around 1100°C. As the temperature increases, the sulfide gets closer to its melting point so sulfur is able to rapidly diffuse through this phase into the substrate[58]. It is possible that all three mechanisms contribute to the high rate of scale growth. Most likely the needles that form during internal oxidation combined with the temperature being over half the melting temperature of Al_2S_3 are the main causes for the accelerated growth rate[58].

1.4.4 Iron-Aluminum Alloys: Mixed Oxidation/Sulfidation

Binary iron-aluminum alloys provide better corrosion properties than pure iron, but their rate of sulfidation is still too high for applications as coatings. In order for iron-aluminum alloys to be protective, preferential oxidation of aluminum must occur so that a uniform Al_2O_3 scale completely covers the substrate. Although this is not possible in a purely sulfidizing environment, exposure to a mixed oxidizing/sulfidizing environment could produce this protective alumina scale as Al_2O_3 is stable with respect to Al_2S_3 to very low oxygen partial pressures (see Figure 14). Low NOx coal-burners create an environment that has a high sulfur partial pressure and a low oxygen partial pressure so the possibility of forming Al_2O_3 is good.

Corrosion resistance of iron-aluminum alloys in mixed oxidizing/sulfidizing environments has been studied extensively by DeVan and Tortorelli[3,63,64]. They report that at 800°C in an atmosphere representative of furnace conditions ($Po_2 = 10^{-22}$ atm, $Ps_2 = 10^{-6}$ atm), the

corrosion rate was significantly higher for an alloy with 8.4wt%Al (16at%Al) than for an alloy containing 9.6wt%Al (18at%Al). They concluded that a minimum aluminum concentration of 9.6wt%Al (18at%Al) is needed at 800°C to provide long-range corrosion protection[65,66]. Others have found similar results, as alloys with aluminum contents below this critical amount displayed duplex scales, where the outer layer was Fe_3O_4 and the inner layer was a mixture of FeS and Al_2S_3[67]. Plate-like precipitates of (Fe, Al)S were also found to extend into the substrate. Above the critical amount of aluminum, again the scales had an outer layer of iron oxides and the inner layer contained a high amount of aluminum sulfates, which attributed to the reduction in corrosion rate[67].

In a study performed by Kai and Huang, they found that in a mixed environment ($Po_2 \cong 10^{-22}$, $Ps_2 \cong 10^{-7}$) at 700°C alloys with aluminum contents between 9.6 and 16wt% formed scales that consisted of FeS, $FeAl_2S_4$, and Al_2O_3[68]. The alumina phase was identified as α-Al_2O_3, even though the temperatures fell within the range of γ- or δ-Al_2O_3 and the scales were in the form of needles. The amount of Al_2O_3 increased with the aluminum content of the alloy up to around 16 wt% where the scales were mostly α-Al_2O_3 with small amounts of FeS and $FeAl_2S_4$ present. The amount of Al_2O_3 again increased with aluminum content up to around 25wt%Al where Al_2O_3 was the only scale present. The corrosion rates were reduced by a factor of about five when a continuous Al_2O_3 layer forms over the substrate.

The corrosion kinetics for binary iron-aluminum alloys with sufficient amounts of aluminum follows the parabolic rate law for temperatures between 700-900°C, indicating that solid-state diffusion is the limiting step during corrosion. Two-stage parabolic behavior can be seen regardless of temperature where an initial stage is followed by a steady-state stage[68]. It can be seen that the duration of the initial stage decreases with increasing aluminum concentration.

1.4.5 Ternary Alloy Additions

Although binary Fe-Al based alloys in general have demonstrated good corrosion resistance in oxidizing, sulfidizing, and mixed environments, even better resistance to corrosion in specific environments can be achieved by adding ternary elements. The effects of ternary elements have been studied over the last few years. Many studies have been conducted with respect to improving the mechanical properties of iron-aluminum based alloys[69]. Others have concentrated on the improvement of corrosion resistance in specific environments and on the improvement of thermal cycling conditions [70-72]. This section will review the effects of specific elements, namely chromium and titanium, on isothermal corrosion resistance.

1.4.5.1 Effect of Chromium

Chromium has played an important role in corrosion resistance for many years as a primary oxidizing agent. This is especially true when considering the oxidation resistance of stainless steels. Stainless steels utilize high levels of chromium in order to form a passive chromia layer on the surface of the substrate[73]. Chromium has also played an important role in corrosion resistance of alumina forming alloys. Traditionally, these alloys have made use of a low concentration of aluminum (less then 10wt%) and high amounts of chromium (greater than 10wt%). Recently, the effects of small additions of chromium on the corrosion resistance of alloys with higher aluminum concentrations have been studied. This section will outline the role of chromium in the oxidation and sulfidation resistance of iron-aluminum based alloys.

The primary role of chromium in binary iron-aluminum alloys is to act as a secondary oxygen "getter" to avoid internal oxidation[45]. In binary iron-aluminum alloys, aluminum has a higher affinity for oxygen than iron and would therefore be expected to form an aluminum oxide before forming an iron oxide. Similarly, a high Al/Cr ratio will most likely favor the formation of a continuous Al_2O_3 layer on the alloy due to aluminum having a higher affinity for oxygen than

chromium. This alumina layer is expected to provide protection from the reactive gas, but if oxygen anions diffuse through the scale they can form chromium-oxides rather than fast growing iron oxides. Chromium therefore acts as a secondary oxide former in the alloy; helping to prevent unwanted iron oxides to form.

Another possible role chromium may play in promoting corrosion resistance was proposed by Brumm and Grabke[74]. They describe the initial stage of oxidation when the oxygen partial pressure is high enough that each alloying element forms oxides at the alloy surface. Once a continuous layer of mixed oxides forms, the oxygen partial pressure is low at the scale-metal interface such that only Al_2O_3 will form. The other oxides are stable only at the scale-gas interface so a continuous layer of Al_2O_3 will grow under the oxides at the metal-scale interface. Cr_2O_3 and α-Al_2O_3 are both hexagonal structures and form a totally miscible solid solution. The reaction of Cr_2O_3 and either γ- or θ-Al_2O_3 will result in the formation of $(Al,Cr)_2O_3$ crystals, which can then act as nucleation sites for α-Al_2O_3 at temperatures below that at which α-Al_2O_3 typically begins to form. These results are consistent with others who observed that chromium additions decrease the temperature at which α-Al_2O_3 forms[49,75]. A schematic diagram of chromium's effect on the nucleation of α-Al_2O_3 at lower temperatures can be seen in Figure 22. The left half of the diagram shows the initial oxidation of a Ni-Al alloy and the right half compares that with the initial exposure of a Ni-Al-Cr alloy to an oxidizing atmosphere. During the initial exposure, selective oxidation of each oxidizing element occurs (Figure 22a). The Ni-Al alloy initially forms NiO and Al_2O_3, while the Ni-Al-Cr alloy forms NiO, Al_2O_3, and Cr_2O_3. After longer exposure, the θ-Al_2O_3 phase completely covers the alloy and begins to react with the other oxides. The θ-Al_2O_3 reacts with NiO to form the spinel $NiAl_2O_4$ on both alloys, but it also reacts with Cr_2O_3 to form a solution of $(Al,Cr)_2O_3$ on the chromium containing alloy (Figure 22b). Because the $(Al,Cr)_2O_3$ phase has a similar crystal structure to α-Al_2O_3, it helps to nucleate

α-Al_2O_3 grains so a relatively continuous α-Al_2O_3 scale can form at lower temperatures than α-Al_2O_3 normally forms (Figure 22c)[74].

Additions of chromium are also beneficial because they decreases the critical aluminum concentration needed to form a uniform protective Al_2O_3 layer. This effect also comes from the fact that chromium will act as a secondary oxidizer, helping to reduce the amount of internal oxidation of aluminum. Wagner explains that during the initial stage of oxidation, iron, chromium, and aluminum oxides will begin to nucleate at the surface of the alloy[45]. The formation of chromium oxides keeps the oxygen from penetrating the alloy and forming Al_2O_3 precipitates under the surface. This, in turn, allows aluminum atoms to diffuse to the surface where reactions similar to:

$$2Al + Cr_2O_3 = 2Cr + Al_2O_3 \quad (15)$$

$$2Al + 3FeO = 3Fe + Al_2O_3 \quad (16)$$

can occur at the surface. Thus the formation of a continuous Al_2O_3 scale is possible at aluminum contents lower than the critical concentration needed in the binary iron-aluminum alloy.

1.4.5.1.1 Fe-Al-Cr Alloys: Oxidation

Chromium additions have shown both beneficial and detrimental effects to the oxidation resistance of iron-aluminum alloys. Beneficial effects have been observed when chromium concentrations are low relative to the aluminum concentration. Fe_3Al (15.8wt%Al) with chromium concentrations of 1-5wt%, oxidized from 700-900°C, showed mixed results[6]. The alloys containing chromium concentrations less than 2wt% between 700-900°C demonstrated low weight gains, whereas concentrations greater than 4wt% showed increased weight gains and faster oxidation rates during the initial exposure. In addition, the alloy with 2wt%Cr had a parabolic rate constant ten times less than the rate constants of alloys with higher concentrations

of chromium. At 900°C, the oxidation rates remained relatively the same, but the initial weight gains increased as the amount of chromium increased (Figure 23).

Chromium can also improve the thermal cycling properties of iron-aluminum alloys in an oxidizing atmosphere. Binary alloys containing 8.4-11wt%Al showed that increasing the aluminum concentration resulted in lower weight gains in cyclic oxidation environments. The addition of 5wt%Cr to the 8.4wt%Al alloy resulted in better protection than both binary alloys[5]. This increase in cyclic oxidation protection was attributed to chromium promoting fast healing of the protective Al_2O_3 scale. When a crack forms in the Al_2O_3 layer, the chromium helps prevent unwanted corrosion products from forming in the crack and the Al_2O_3 scale has a greater chance of re-healing itself faster. The rapid recovery of the Al_2O_3 scale keeps unwanted products, such as iron oxide nodules, from forming in these cracks and overgrowing the passive layer[3].

1.4.5.1.2 Fe-Al-Cr Alloys: Mixed Oxidation/Sulfidation

The addition of chromium to binary iron-aluminum alloys in mixed oxidizing/sulfidizing ($P_{O_2} \cong 10^{-20}$, $P_{S_2} \cong 10^{-4}$) environments has had similar effects to additions in purely oxidizing environments. Additions of more than 2wt%Cr to Fe_3Al alloys over the range of 700-900°C resulted in increased weight gains due to the formation of sulfides[1,6,71]. The increase in weight gain at greater chromium concentrations was attributed to excess chromium accelerating the nucleation and growth of iron and chromium sulfides[1,3,76]. During exposure a protective layer of Al_2O_3 formed, but iron sulfides grew as flat needles out of the scale as macroscopic defects occurred in the scale at highly stressed corners and edges. The scales that formed after long exposure times consisted of a thick outer layer of sulfides (mainly iron), a thin middle layer comprised of iron and aluminum oxides, and an even thinner inner layer of Al_2O_3[71]. On the other hand, it has been found that the detrimental effects from higher chromium concentrations can be

negated in these environments by increasing the aluminum concentration[3,6]. Therefore, it is important to keep the Al/Cr ratio high for adequate protection in mixed gas environments.

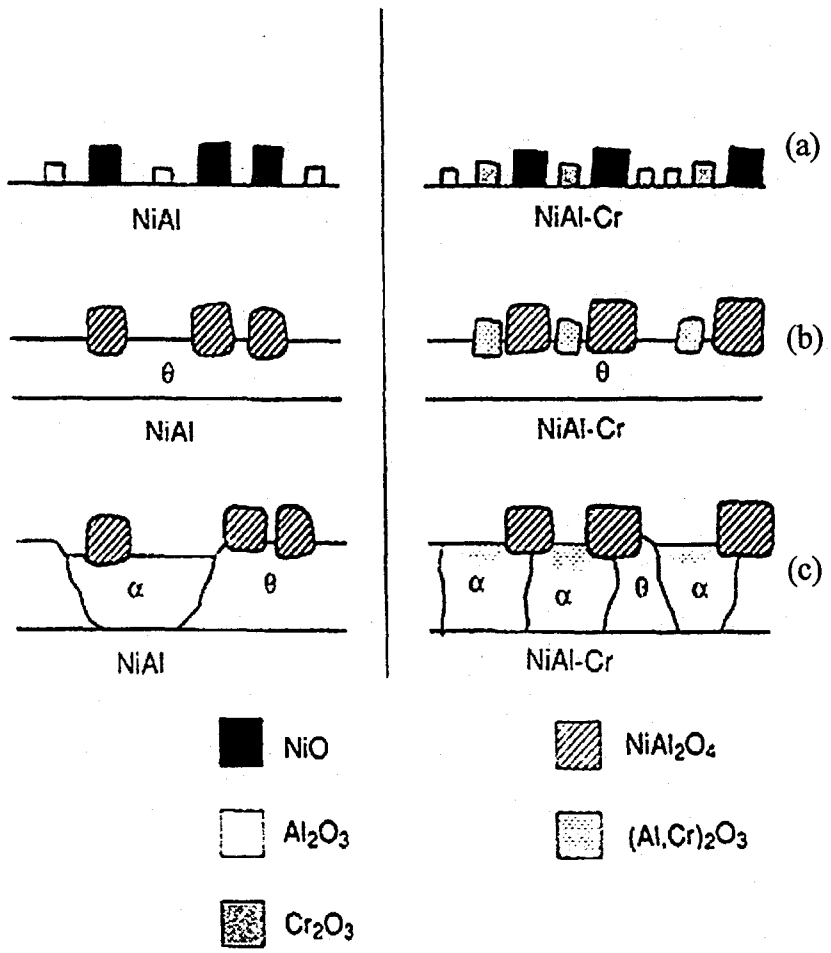

Figure 22 – Schematic diagram of chromium's effect on the formation of alumina[74].

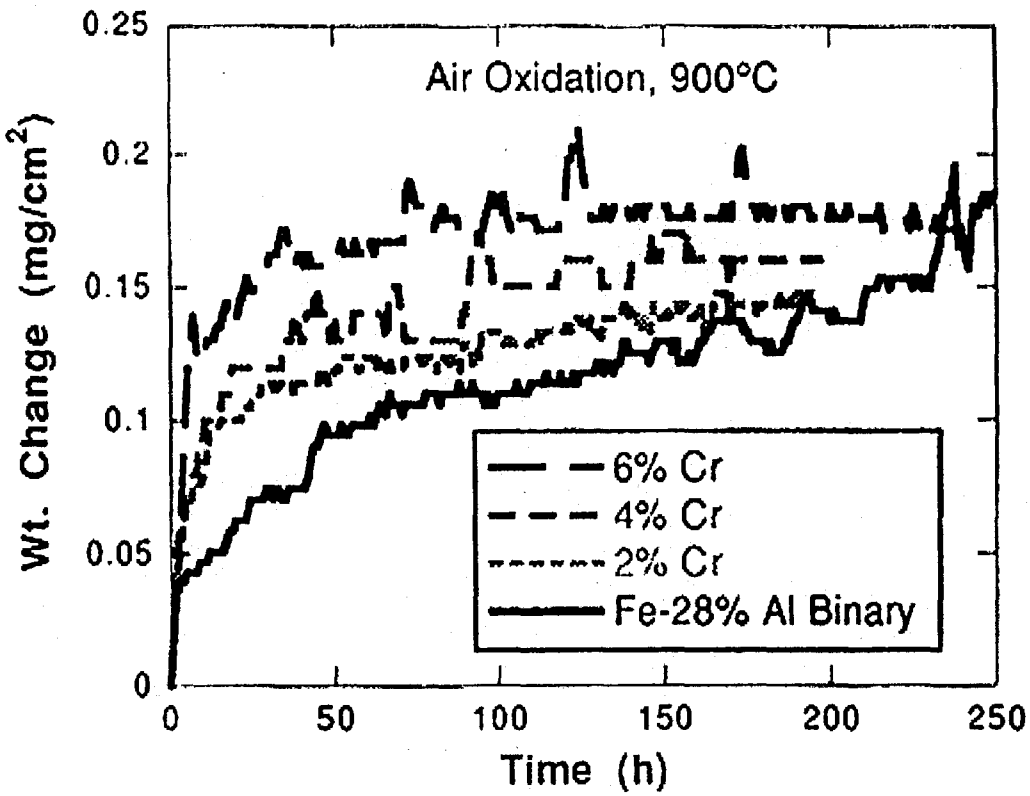

Figure 23 – Weight gain data showing the effect of chromium on weight gain[6].

1.4.5.2 Effect of Titanium

Titanium has been used in a variety of corrosion resistant applications primarily due to its excellent oxidation resistance. Many of these applications use titanium based alloys such as Ti-Al because of their good corrosion resistance and their relatively low weight[77-79]. Limited work has been conducted dealing with the effects of titanium on iron-aluminum based alloys. Studies that have been done on titanium additions to iron-aluminum based alloys have primarily focused on improvement of the mechanical properties at room temperature[80-82]. Some work done on ternary additions of titanium to iron-aluminum alloys has focused on the effect on high temperature corrosion behavior of these alloys[83,84]. The following section will outline the relevant research conducted on the effect of titanium on the high temperature corrosion resistance of iron-aluminum based alloys.

1.4.5.2.1 Oxidation

The primary goal of adding small amounts of titanium to iron-aluminum based alloys is to increase the alloy's corrosion resistance by acting as a secondary oxygen "getter". As discussed previously for chromium additions, if oxygen penetrates through the passive scale on the surface of a relatively protective alloy, the secondary oxidizing element can react with the oxygen to "getter" the oxygen and form slower growing corrosion products. By forming slower growing titanium oxides, this can hopefully prevent iron-rich oxides from forming and overgrowing the passive Al_2O_3 scale. Although some work has been performed on the effect of titanium additions on high temperature oxidation of Fe-Al based alloys, very little has been done on the sulfidation of these alloys. This being the case, the oxidation behavior of Fe-Al alloys containing Ti will be reviewed.

Early work utilizing titanium additions was conducted by Giles and Marder who studied the effect of titanium additions on the thermal cycling oxidation resistance of iron[83]. The iron

based alloys they studied contained aluminum, chromium, and titanium additions and the alloys were thermally cycled between approximately 1200°C to 200°C until a significant amount of corrosion took place. They found that a critical compositional value, based on regression analysis, could be achieved where compositions above the critical value resulted in a dramatic increase in the oxidation lifetime (time until breakaway corrosion occurred). The critical compositional value that was based on regression analysis included aluminum, chromium, and titanium additions. The key point to this study though was that all alloys above the critical value contained titanium additions, between 0.28 and 1.02wt%Ti, with the exception of two alloys. These two alloys had oxidation lifetimes much less than other alloys containing titanium. It was therefore concluded that titanium helped improve the cycling oxidation resistance of iron aluminum alloys.

Since then, others have performed more comprehensive studies involving the additions of titanium to iron-aluminum based alloys. Culbertson and Kortovich found that additions of 5at%Ti to the intermetallic Fe_3Al resulted in a decrease in the oxidation resistance when exposed to air at 816°C[85]. On the other hand, a recent study has shown that titanium additions up to 2at% have had a beneficial effect on the corrosion behavior of Fe-Al based alloys[84]. In this study it was found that alloys containing titanium additions had significantly lower corrosion rates in air at 1000-1100°C. Alloys without titanium additions were observed to form a much finer α-Al_2O_3 scale on the surface than the alloy with Ti additions. Alloys containing titanium additions formed some titanium-oxides, in the form of TiO, on the surface along with α-Al_2O_3. The thicker alumina scale observed on the alloy without titanium additions was attributed to the presence of more grain boundaries acting as fast diffusion sites for more rapid oxidation rates. Scale adhesion was observed to increase with the additions of 2at%Ti as well[84]. This effect was attributed to the TiO phase that formed on the surface along with the protective alumina scale. The authors made several possible explanations as to why the adhesion of the protective scale is better with titanium

present. The most reasonable explanation was that the coefficient of thermal expansion for TiO (~10 X 10^{-6}/°C) is between that of α-Al_2O_3 (~6 X 10^{-6}/°C) and FeAl (~21 X 10^{-6}/°C) so the TiO phase reduces the difference in the coefficient of thermal expansion of the passive oxide layer and the underlying alloy.

1.4.6 Effect of Water Vapor

When considering the environments that are present within fossil-fueled furnaces, one component that is always present but often times gets overlooked is water vapor. Water vapor has been identified in several different combustion environments found in fossil-fueled power plants at levels ranging from 3-25%H_2O[15]. Although it has been documented that water vapor is almost always present in these furnace atmospheres, it is rarely used when simulating burner conditions for high temperature corrosion testing. Many researchers use simple dry gas mixtures consisting of only a few components, such as using H_2-H_2S mixtures when simulating a sulfidizing environment and dry air when simulating oxidizing conditions[6,8,44,58]. This is commonly done because the mechanisms behind the effect of water vapor on high temperature corrosion are poorly understood. Therefore, available theories on the mechanism of water vapor will briefly be discussed in this section.

There have been a few proposed theories dealing with the effect of water vapor on high temperature corrosion, but the theories lack consistency between each other do not always correlate with observations made from other alloy systems. The bulk of the work on this topic has been done in Japan, but unfortunately very little has been translated into English for interpretation. When considering this phenomenon, some authors feel that the main effect of water vapor on high temperature corrosion behavior is that it alters the passive scale that forms during oxidation[86-88]. Exactly how the water vapor effects the scales is not well understood. Some claim that the oxide scales that typically form in dry oxidizing environments change to

hydroxide scales when exposed to oxidizing atmospheres containing water vapor[86]. These hydroxide scales have been reported to be porous and easily permeable by corrosive species[87]. Others have made observations that correlate with the theory that H_2O in the gas will alter the corrosion scale morphology of non-protective corrosion products that form once the passive layer breaks down[89-91]. Some agree that the water vapor affects the surface conditions during the initial stages of oxidation, but they propose that the resultant oxide to form is a function of the surface acidity, which changes with the addition of water vapor[92]. It can be seen that although it is well established that corrosion rates increase with the presence of water vapor and that the morphology of the scale changes from dry to wet oxidizing conditions, the mechanisms behind the water vapor effect are not clear and are currently being explored further.

1.4.7 Summary

The addition of aluminum increases the high temperature corrosion resistance of iron in oxidizing, sulfidizing, and mixed environments. The increase in corrosion resistance comes from the formation of aluminum rich scales, in particular Al_2O_3, which acts as a barrier to metal and oxygen ion diffusion. Depending on the temperature (between 600-800°C) and the type of environment, the critical aluminum concentration needed to form a uniform, protective Al_2O_3 layer on binary iron-aluminum alloys ranges from 5-12wt%Al. Adding small amounts of chromium to binary iron-aluminum alloys is beneficial as it helps prevent internal oxidation and decreases the critical aluminum concentration. Excess chromium concentrations are detrimental though as they can increase the corrosion rates of Fe-Al alloys in mixed oxidizing/sulfidizing atmospheres. Titanium additions have been shown to improve the oxidation resistance of Fe-Al based alloys, possibly by helping to increase the adhesion of the passive oxide scale. The effect of water vapor on high temperature oxidation is known to be detrimental to the corrosion resistance of the alloy. Although it is known that water vapor increases the corrosion rates of

alloys, the mechanisms involved with the decrease in protection are not very well understood and need to be explored further.

1.5 Fe-Al Based Coatings

Iron-aluminum based alloys have been shown to exhibit excellent corrosion resistance in a variety of high temperature environments. Unfortunately, iron-aluminum intermetallics (FeAl and Fe_3Al) are inherently brittle at room temperature and the material shows a drastic decrease in strength at temperatures above 600°C[1]. Although iron-aluminum alloys may be a poor choice as a structural material, their use as a coating is now fully being discovered. Two main coating techniques that are being investigated are weld overlay and thermal spray coatings.

1.5.1 Weld Overlay

The main concept behind weld overlay coatings is that an aluminum or iron-aluminum alloy is used as filler metal and is deposited on a higher strength substrate. As seen above, composition plays an important role in the corrosion resistance of the coating. Unfortunately, iron-aluminum alloys are susceptible to hydrogen induced cracking at higher aluminum concentrations[8,93,94]. One possible explanation to the susceptibility of Fe-Al alloy to hydrogen cracking is that the hydrogen that is released when water vapor combines with molten aluminum to form Al_2O_3[94]. A comprehensive weldablility study was conducted by Banovic, who discovered that welds with aluminum concentrations up to around 10wt% were completely crack free, whereas welds above 10wt%Al cracked readily[95]. This composition is approximately the border between the disordered iron solution and the ordered Fe_3Al at lower temperatures. It is therefore very important to control processing parameters during the welding process in order to control the composition of the weld overlay.

1.5.2 Thermal Spray Coatings

Thermal spray coatings consist of spraying iron-aluminum based powders at high temperatures onto a substrate. Two techniques, air plasma spray (APS) and high-velocity oxygen fuel (HVOF), were compared by Luer et.al. in a sulfidizing environment. APS coatings contained aluminum depleted regions due to degradation of the powder during application[9]. The coating also contained a high amount of porosity, which may have allowed for sulfur to travel through the coating and attack the substrate. On the other hand, the HVOF coatings contained low porosity and low oxide contents. Sulfidation resistance of the HVOF coating was significantly better than the resistance of the APS coating. This was attributed to the sulfur gas being able to penetrate to the substrate through interconnecting porosity in the APS coating. The HVOF coating was compact enough to prevent the sulfur gas from reaching the iron substrate and therefore controlled the amount of corrosion that occurred[9].

1.5.3 Summary

Weld overlay coatings are advantageous because they provide a relatively uniform coating that bonds to the substrate by mechanical mixing. The disadvantage of using this process is that at high aluminum concentrations (above 10wt%Al), the welds are subject to cold cracking. Welds with aluminum concentration below 10wt% are easily weldable and show good corrosion resistance. On the other hand thermal sprays can incorporate higher aluminum contents because cold cracking does not occur in thermal spray coatings. One disadvantage of thermal spray coatings is that the coating can be porous and contain oxides, which can accelerate corrosion. Another disadvantage is that there is no metallurgical mixing between the coating and the substrate so the coating may flake off due to stresses during service. Thermal spray coatings produced by the HVOF technique have been shown to contain low porosity, low oxide content, and demonstrate good corrosion resistance. Now that the fundamentals of high-temperature

corrosion and the relevant literature on iron-aluminum alloys has been reviewed, the following sections will focus primarily on the recent study performed on the high-temperature corrosion resistance of Fe-Al based coatings.

2. Chapter 2: Gaseous Corrosion Testing

"High Temperature Corrosion Resistance of Fe-Al Based Weld Overlays with Cr and Ti Additions"

2.1 Introduction

It has been seen in the previous sections that various corrosion mechanisms can take place in diverse environments such as Low NOx burners. During the initial exposure of a coating to a Low NOx environment, gaseous corrosion will dominate as the primary corrosion mechanism. After sufficient exposure times, slag can accumulate on the surface of the coatings as un-burnt coal and ash can deposit onto the walls. Therefore, two approaches were taken to simulate Low NOx environments. First, gaseous corrosion testing was performed on the iron-aluminum based coatings. This was done to simulate the initial period of exposure and areas where slag does not accumulate or falls off. The other approach was gas-slag corrosion testing. This involved placing a simulated slag in contact with the coating and setting them in a corrosive gaseous environment. This helped to simulate the situations where significant slag did accumulate on the walls and acts as a barrier between the corrosive gas species and the coating. The present chapter will focus on the gaseous corrosion testing of weld overlay coatings. The following chapters will involve the gas-slag corrosion testing of weld overlay coatings and both gaseous and gas-slag corrosion testing of thermal spray coatings. The final section will discuss the effects of water vapor on high temperature corrosion as well as summarize the results from this investigation.

As was previously mentioned, Fe-Al based weld overlay coatings have recently been considered as corrosion resistant claddings as an alternative to stainless steel or superalloy coatings[1]. Fe-Al based claddings are advantageous because they are corrosion resistant in sulfidizing environments, they are easily weldable with aluminum concentrations up to 10wt%,

and are cheaper than using stainless steel or superalloy coatings[1,3,8,55,76,95]. Binary Fe-Al alloys have been studied extensively in simple sulfidizing and oxidizing environments for years, but less work has been done on ternary or quaternary Fe-Al based alloys. It has been shown that chromium additions to Fe-Al based alloys have helped increase the corrosion resistance in sulfidizing and oxidizing atmospheres[3,66]. Titanium has been known traditionally as an oxide former and has shown to increase the oxidation resistance of iron-aluminum based alloys[83,84]. Therefore, alloys containing chromium and titanium additions were considered for corrosion testing in this study. Traditionally, environments used to study high temperature corrosion behavior in these alloys have been simple gas mixtures, containing relatively few components[96]. To more accurately simulate burner conditions, three complex gases were considered in this particular study, one being a highly sulfidizing gas, another being a mixed oxidizing/sulfidizing gas, and an oxidizing gas.

2.2 Experimental Procedure

Alloys were made by arc-melting high purity components under an argon atmosphere and drop cast into a water-cooled copper mold. Cast alloys were used because it was previously shown that the high temperature corrosion behavior of weld overlays could be explained by using cast alloys of equivalent composition[64]. Alloys contained 7.5wt% or 10wt%Al, chromium levels ranged from 0-5wt%, and two quaternary alloys contained both chromium and titanium additions. All alloy compositions can be seen in Table 2. Corrosion experiments were carried out using a Netzsch STA 409 high-temperature thermogravimetric (TG) balance, which measures changes in weight over time. Samples were ground to 600 grit and measured to the nearest hundredth of a millimeter. They were then weighed to the nearest tenth of a milligram using a digital balance and cleaned using acetone. The specimens were heated at a rate of 50°C/min and were held at 500°C for 100 hours. Water vapor present in the mixed oxidizing/sulfidizing and the oxidizing

environments was injected into the furnace at a controlled rate. The three gas compositions used for this study can be seen in Table 3. The sulfur and oxygen partial pressures were calculated for the gases using the HSC Chemistry computer program[39]. Selected exposed samples were cut approximately 80% through and submersed into liquid N_2. The samples were then cracked and dropped into ethanol to obtain cracked surface images. A JEOL 6300 Scanning Electron Microscope (SEM) was used to obtain surface images as well as images of selected polished cross sections and cracked cross sections. Samples were observed with a 17mm working distance and accelerating voltages of 5keV and 10keV. SEM surface images were used with an imaging program to obtain area fractions.

Table 2– Alloy compositions used for corrosion testing. All values are in weight percent.

Alloy Designation	Fe	Al	Cr	Ti
Fe-7.5Al	Bal.	7.38	--------	--------
Fe-7.5Al-1Cr	Bal.	7.45	0.96	--------
Fr-7.5Al-2Cr	Bal.	7.59	2.09	--------
Fe-7.5Al-5Cr	Bal.	7.77	5.03	--------
Fe-7.5Al-2Cr-1.5Ti	Bal.	7.81	2.19	1.65
Fe-10Al	Bal.	10.04	--------	--------
Fe-10Al-1Cr	Bal.	10.04	0.99	--------
Fe-10Al-2Cr	Bal.	10.19	2.16	--------
Fe-10Al-5Cr	Bal.	10.74	5.18	--------
Fe-10Al-2Cr-1.5Ti	Bal.	10.34	2.18	1.67

2.3 Results and Discussion

2.3.1 Sulfidizing Environment

The kinetic results for the Fe-7.5wt%Al series of alloys exposed to the sulfidizing gas can be seen in Figure 24. All five alloys containing aluminum concentrations of 10wt% showed no weight gain after 100 hours in the sulfidizing environment, and can be seen in Figure 25. Fe-7.5Al, Fe-7.5Al-1Cr, and Fe-7.5Al-2Cr showed weight gains of approximately 0.7 mg/cm^2 after 100 hours. These samples formed a blocky external scale that completely covered the samples. One the other hand, Fe-7.5Al-5Cr and Fe-7.5Al-2Cr-1.5Ti were both protective after 100 hours. Scratch marks could still be seen on these two samples after testing, but it was observed that areas of the blocky external nodules were present on these samples. Polished cross sections were observed for two representative samples, Fe-7.5Al (Figure 26) and Fe-7.5Al-5Cr (Figure 27). The Fe-7.5Al sample formed an external scale over its entire surface and showed signs of substrate corrosion as needles that penetrated into the alloy. The Fe-7.5Al-5Cr sample formed a thin scale that almost completely covered the alloy. It was observed that the scale thickness of Fe-7.5Al (~8μm thick) was significantly thicker than the passive layer formed on Fe-7.5Al-5Cr (~1μm).

Table 3– Gas Compositions used for corrosion testing (vol. %).

Gas Component	Sulfidizing Gas	Mixed Oxidizing/Sulfidizing Gas	Oxidizing Gas
O_2	--------	--------	2
CO	15	10	--------
CO_2	--------	5	15
H_2	3	--------	--------
H_2O	--------	2	6
H_2S	0.12	0.12	--------
SO_2	--------	--------	0.12
N_2	Bal.	Bal.	Bal.
Log Po_2	-28	-19	-2
Log Ps_2	-6	-8	-46

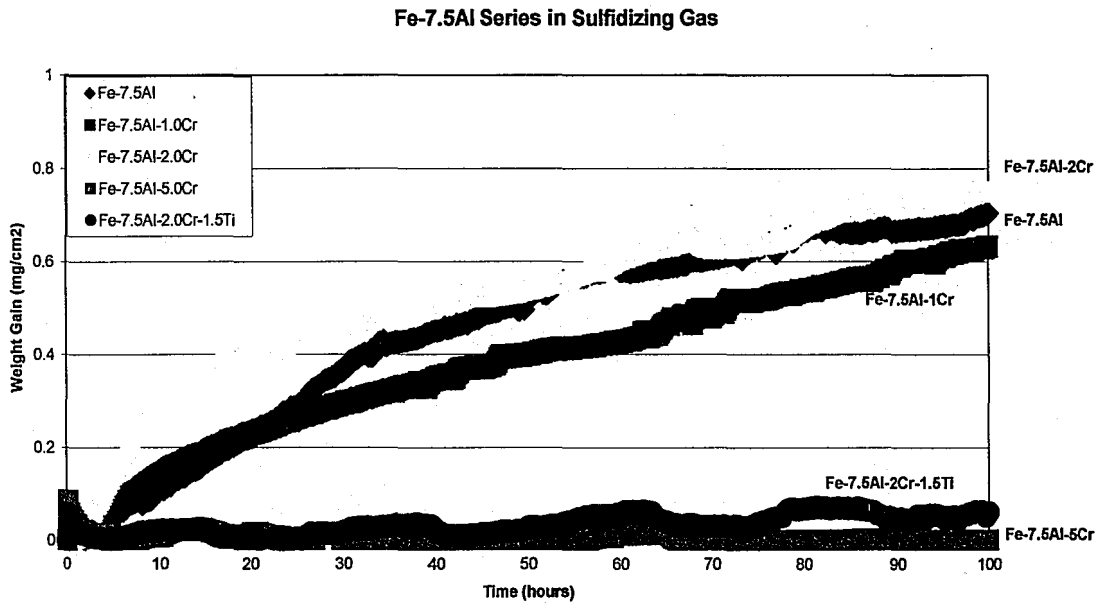

Figure 24 – Kinetic results for the Fe-7.5wt%Al series exposed to the sulfidizing environment.

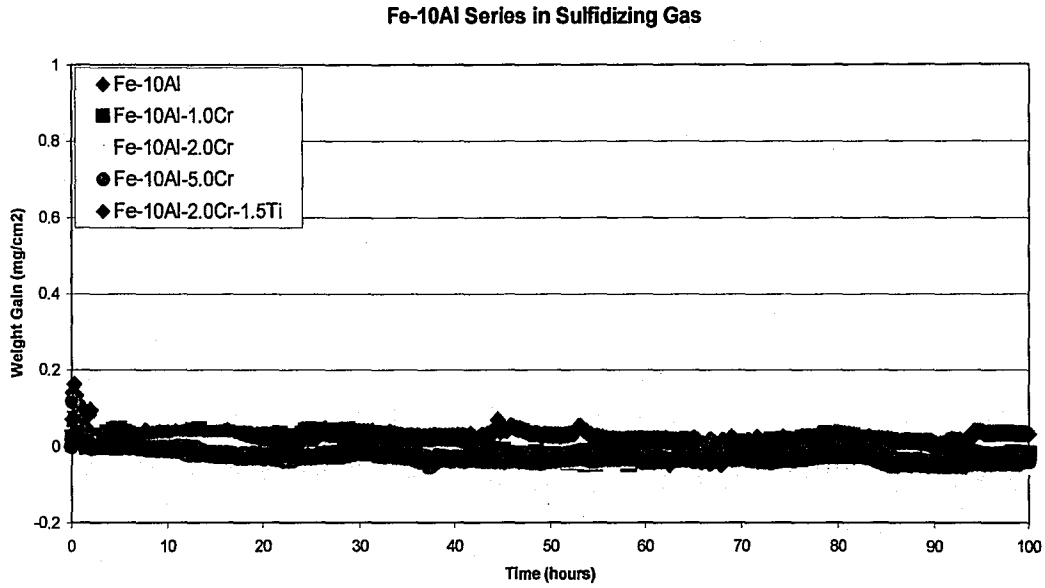

Figure 25 – Kinetic results for the Fe-10wt%Al series exposed to the sulfidizing environment.

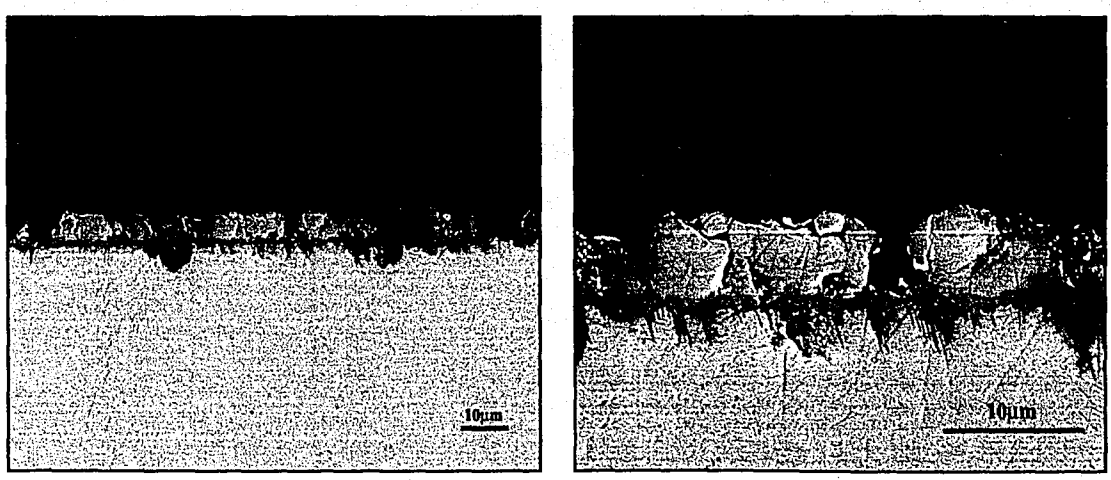

(a) (b)

Figure 26 – Polished cross sections of Fe-7.5Al where thick external scale formed and substrate corrosion was present as needles extending into the alloy.

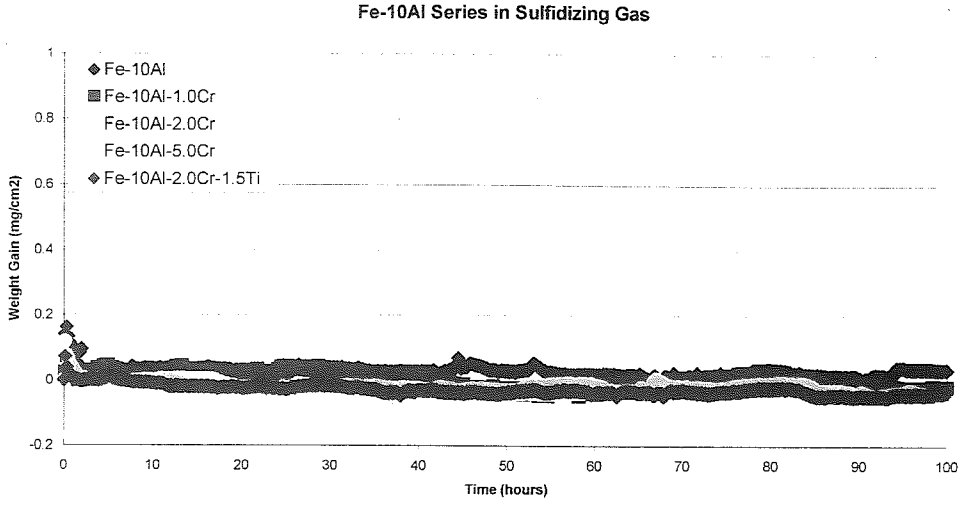

Figure 25 – Kinetic results for the Fe-10wt%Al series exposed to the sulfidizing environment.

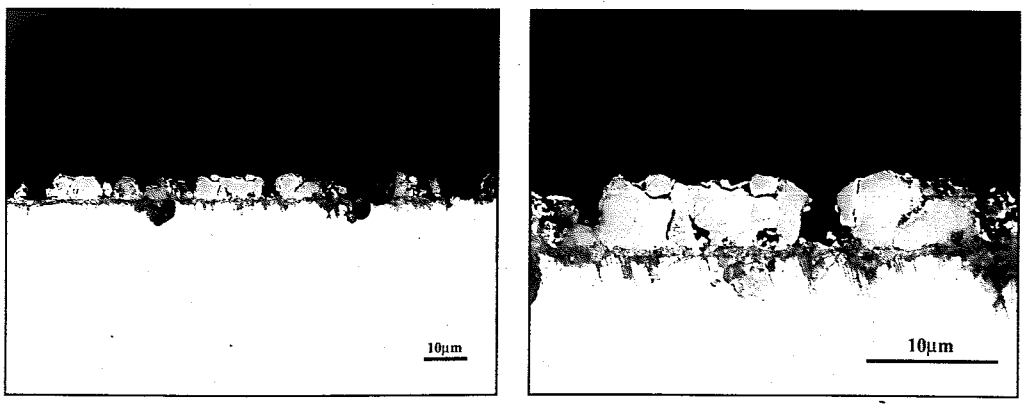

(a) (b)

Figure 26 – Polished cross sections of Fe-7.5Al where thick external scale formed and substrate corrosion was present as needles extending into the alloy.

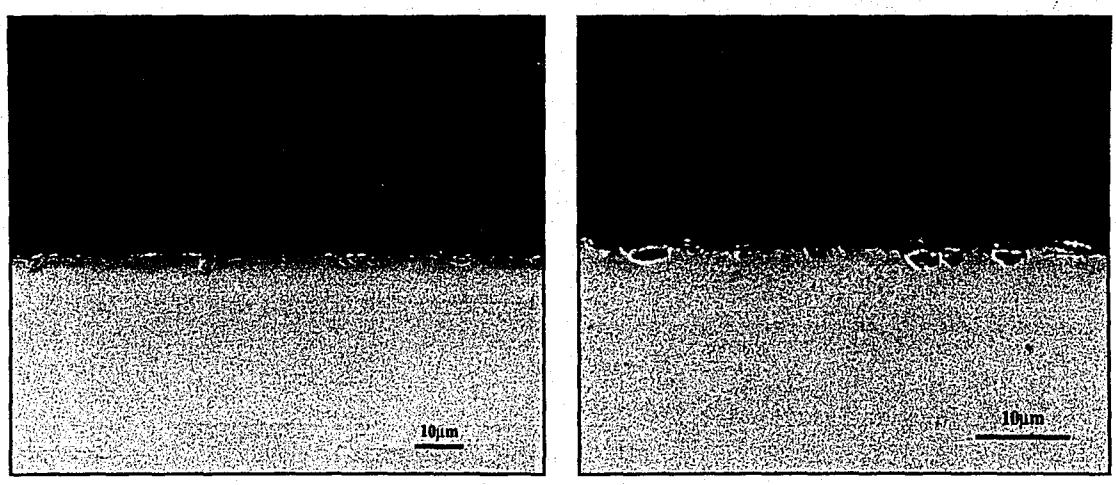

(a) (b)

Figure 27 – Polished cross sections of Fe-7.5Al-5Cr where a thin passive layer covered the entire surface.

2.3.2 Mixed Oxidizing/Sulfidizing Environment

The kinetic results for the Fe-7.5wt%Al series of alloy exposed to the mixed oxidizing/sulfidizing environment can be seen in Figure 28. All the alloys containing 7.5wt%Al exposed to the mixed oxidizing/sulfidizing environment demonstrated large weight gains on the order of 6 mg/cm^2 after 100 hours, and formed a thick scales that cracked and spalled when removed from the furnace. The kinetic results for the Fe-10wt%Al series of alloys exposed to the mixed oxidizing/sulfidizing gas can be seen in Figure 29. The Fe-10Al sample gained approximately 1 mg/cm^2 after 100 hours, and over 75% of the sample was covered by an external scale, whereas the ternary Fe-10wt%Al alloys containing chromium showed no apparent weight gains after 100 hours. Scratch marks could still be observed on these samples after testing and they showed only small areas of external corrosion, which were observed as small groups or single nodules. Polished cross sections of Fe-10Al and Fe-10Al-2Cr exposed to the mixed oxidizing/sulfidizing environment can be seen in Figure 30 and Figure 31, respectively. Figure 30a shows that Fe-10Al had areas where a thick external scale formed (~10μm thick) and

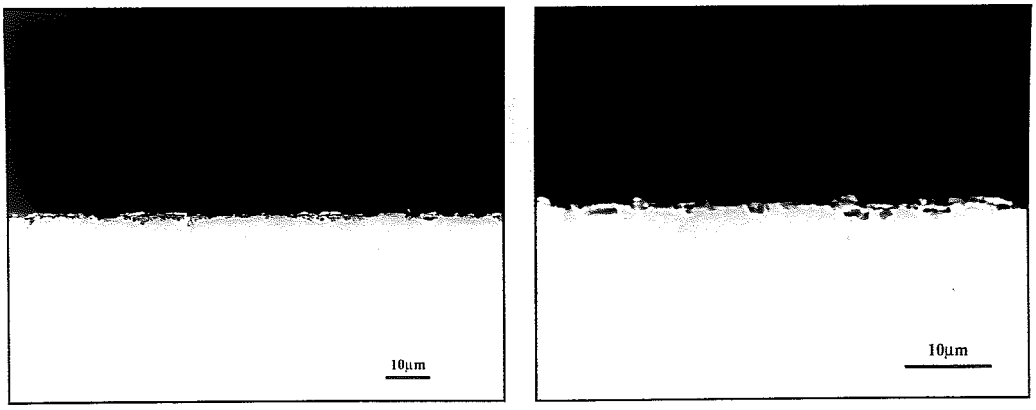

(a) (b)

Figure 27 – Polished cross sections of Fe-7.5Al-5Cr where a thin passive layer covered the entire surface.

2.3.2 Mixed Oxidizing/Sulfidizing Environment

The kinetic results for the Fe-7.5wt%Al series of alloy exposed to the mixed oxidizing/sulfidizing environment can be seen in Figure 28. All the alloys containing 7.5wt%Al exposed to the mixed oxidizing/sulfidizing environment demonstrated large weight gains on the order of 6 mg/cm^2 after 100 hours, and formed a thick scales that cracked and spalled when removed from the furnace. The kinetic results for the Fe-10wt%Al series of alloys exposed to the mixed oxidizing/sulfidizing gas can be seen in Figure 29. The Fe-10Al sample gained approximately 1 mg/cm^2 after 100 hours, and over 75% of the sample was covered by an external scale, whereas the ternary Fe-10wt%Al alloys containing chromium showed no apparent weight gains after 100 hours. Scratch marks could still be observed on these samples after testing and they showed only small areas of external corrosion, which were observed as small groups or single nodules. Polished cross sections of Fe-10Al and Fe-10Al-2Cr exposed to the mixed oxidizing/sulfidizing environment can be seen in Figure 30 and Figure 31, respectively. Figure 30a shows that Fe-10Al had areas where a thick external scale formed (~10μm thick) and

substrate corrosion took place, as well as areas where a thin passive layer was maintained. The external scales that formed were seen as thick blocks, which were consistent with observations from the surface of the specimen. On the other hand, Fe-10Al-2Cr was almost completely covered with a thin passive scale (~1μm thick), but there were a few areas where external nodules could be seen. It should be noted that additions of titanium had no significant affect on the corrosion behavior of the Fe-Al-Cr based alloys in the mixed oxidizing/sulfidizing environment.

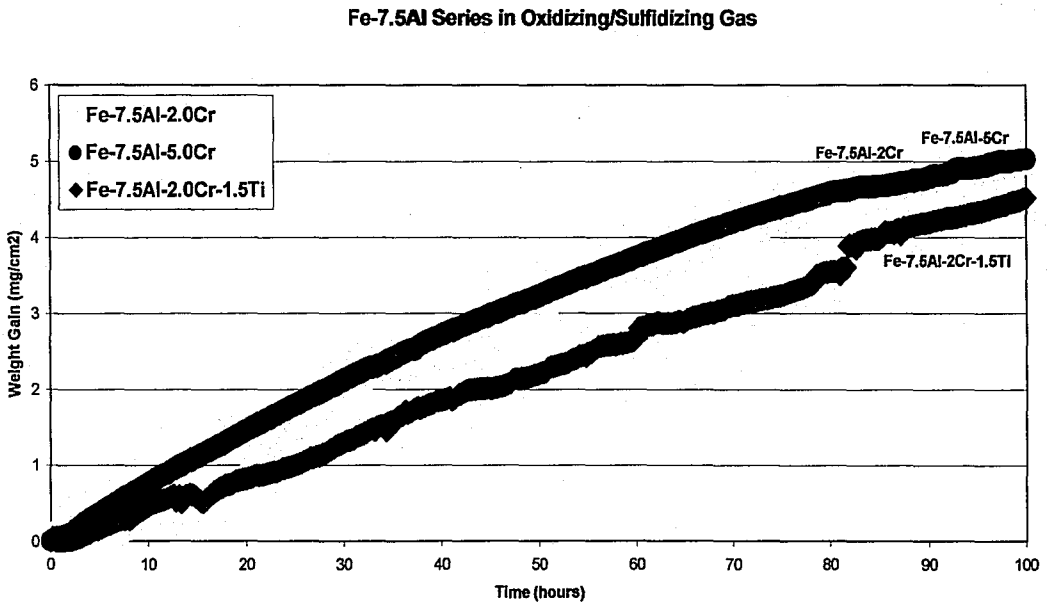

Figure 28 – Kinetic results for the Fe-7.5wt%Al series exposed to the mixed oxidizing/sulfidizing environment.

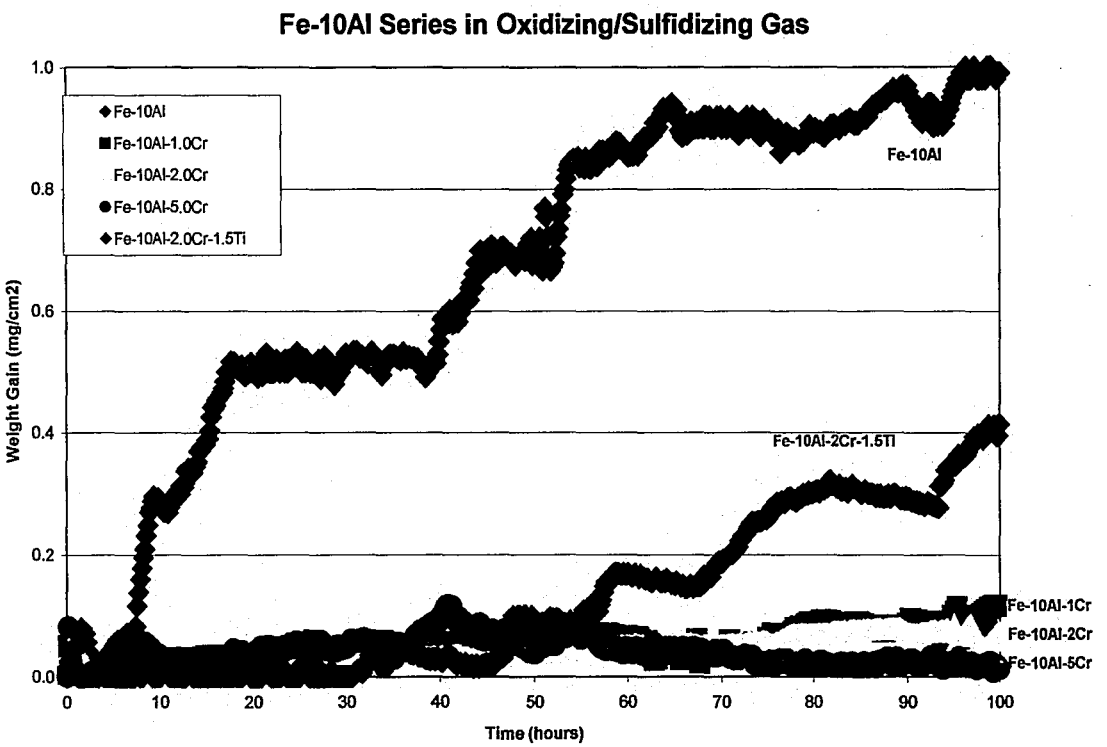

Figure 29 – Kinetic results for the Fe-10wt%Al series exposed to the mixed oxidizing/sulfidizing environment.

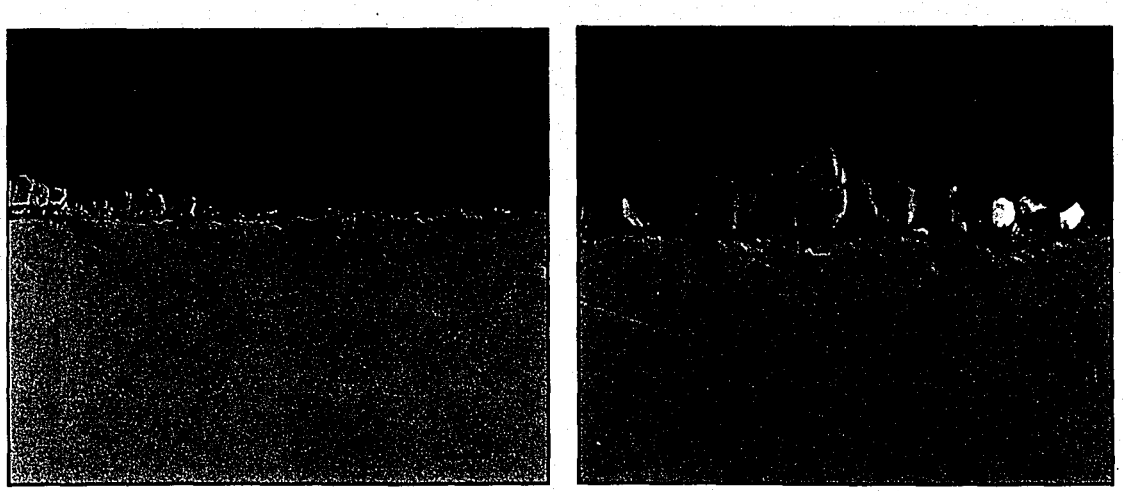

(a) (b)

Figure 30 – Polished cross section of Fe-10Al after exposure to the oxidizing/sulfidizing gas. Two distinct regions can be seen where both external corrosion occurred and where the passive layer was retained (a). Substrate corrosion can also be seen in the regions where external corrosion occurred (b).

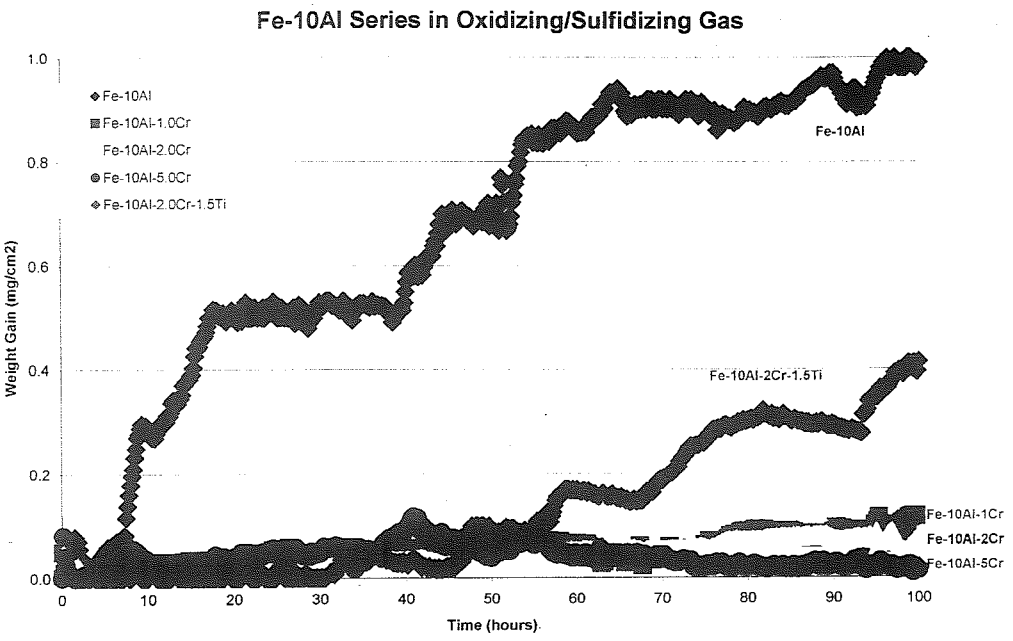

Figure 29 – Kinetic results for the Fe-10wt%Al series exposed to the mixed oxidizing/sulfidizing environment.

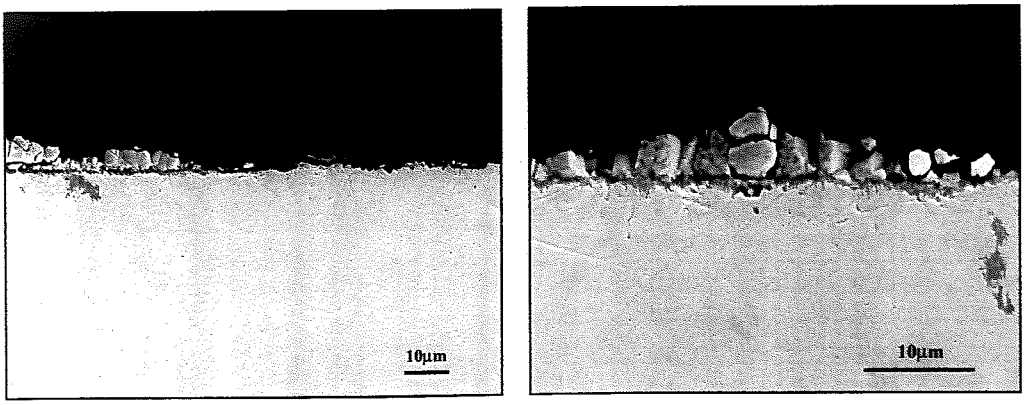

(a) (b)

Figure 30 – Polished cross section of Fe-10Al after exposure to the oxidizing/sulfidizing gas. Two distinct regions can be seen where both external corrosion occurred and where the passive layer was retained (a). Substrate corrosion can also be seen in the regions where external corrosion occurred (b).

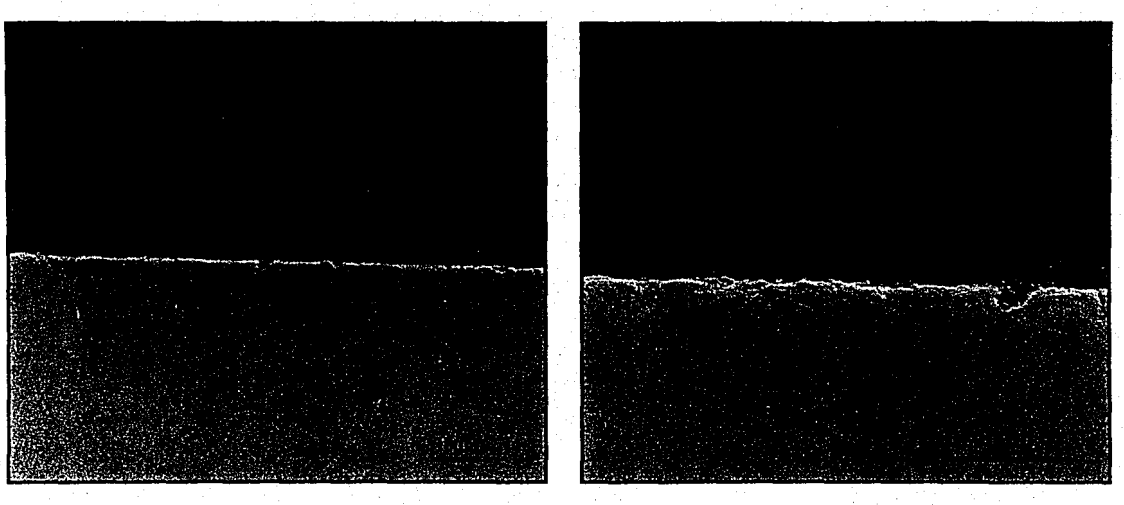

(a) (b)

Figure 31 – Polished cross section of the passive layer formed on Fe-10Al-2Cr after being exposed to the oxidizing/sulfidizing gas.

2.3.3 Oxidizing Environment

The kinetic results obtained for selected alloys exposed to the oxidizing environment can be seen in Figure 32. Alloys containing 7.5wt%Al and chromium additions ranging from 0-2wt%Cr showed weight gains of approximately 1.5 mg/cm^2 during exposure to the oxidizing gas at 500°C for 100 hours. Additions of 5wt%Cr to these alloys helped to retard the corrosion kinetics so that the alloy gained only approximately 0.2 mg/cm^2 during 100 hours of exposure. Alloys containing 10wt%Al showed excellent corrosion behavior in the oxidizing environment. All exposed alloys containing 10wt%Al gained almost no weight during 100 hours of exposure and no significant corrosion product was observed on any of the samples. Observation of the corrosion sample surfaces revealed that the alloys containing 7.5wt%Al had significant corrosion products form over the entire surface. The corrosion product morphology varied with these samples depending on the chromium concentration of the alloy. Figure 33 shows the differences seen in the morphology of the external corrosion scales for Fe-7.5Al, Fe-7.5Al-2Cr, and Fe-7.5Al-5Cr. On the other hand, scratch marks could still be seen on the alloys containing 10wt%Al, indicating that a thin passive layer formed and protected the alloys from rapid

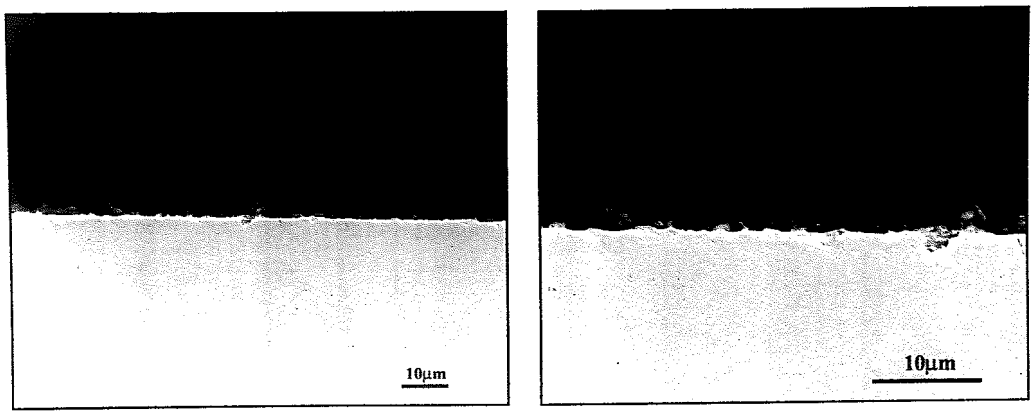

(a) (b)

Figure 31 – Polished cross section of the passive layer formed on Fe-10Al-2Cr after being exposed to the oxidizing/sulfidizing gas.

2.3.3 Oxidizing Environment

The kinetic results obtained for selected alloys exposed to the oxidizing environment can be seen in Figure 32. Alloys containing 7.5wt%Al and chromium additions ranging from 0-2wt%Cr showed weight gains of approximately 1.5 mg/cm^2 during exposure to the oxidizing gas at 500°C for 100 hours. Additions of 5wt%Cr to these alloys helped to retard the corrosion kinetics so that the alloy gained only approximately 0.2 mg/cm^2 during 100 hours of exposure. Alloys containing 10wt%Al showed excellent corrosion behavior in the oxidizing environment. All exposed alloys containing 10wt%Al gained almost no weight during 100 hours of exposure and no significant corrosion product was observed on any of the samples. Observation of the corrosion sample surfaces revealed that the alloys containing 7.5wt%Al had significant corrosion products form over the entire surface. The corrosion product morphology varied with these samples depending on the chromium concentration of the alloy. Figure 33 shows the differences seen in the morphology of the external corrosion scales for Fe-7.5Al, Fe-7.5Al-2Cr, and Fe-7.5Al-5Cr. On the other hand, scratch marks could still be seen on the alloys containing 10wt%Al, indicating that a thin passive layer formed and protected the alloys from rapid

corrosion (Figure 33). Some external nodule growth was seen on the Fe-10Al sample, but additions of chromium prevented any further external growth in the oxidizing environment.

From the kinetic results obtained on the matrix of alloys it can be seen that the aluminum concentration of the weld overlays must be at least 10wt% in order to stifle rapid corrosion kinetics during 100 hours of exposure in the three gases. This can be seen for the sulfidizing gas, the mixed oxidizing/sulfidizing environment, and the oxidizing gas in Figure 34, Figure 35, and Figure 36, respectively. For the sulfidizing gas, two alloys containing 7.5wt%Al were protective after 100 hours, but these two alloys gained a significant amount of weight in the mixed oxidizing/sulfidizing gas. On the other hand, the entire Fe-10wt%Al series was capable of being protective after 100 hours in the sulfidizing gas. In the mixed oxidizing/sulfidizing gas, the binary Fe-10Al alloy showed weight gains that were much less than the 7.5wt%Al series of alloys, but additions of chromium to the alloys containing 10wt%Al stifled the corrosion kinetics and no weight gains occurred. In the oxidizing gas, Fe-10wt%Al alloys faired well and gained relatively no weight after 100 hours. Therefore, in order to obtain a protective coating in these types of environments, at least 10wt%Al is required.

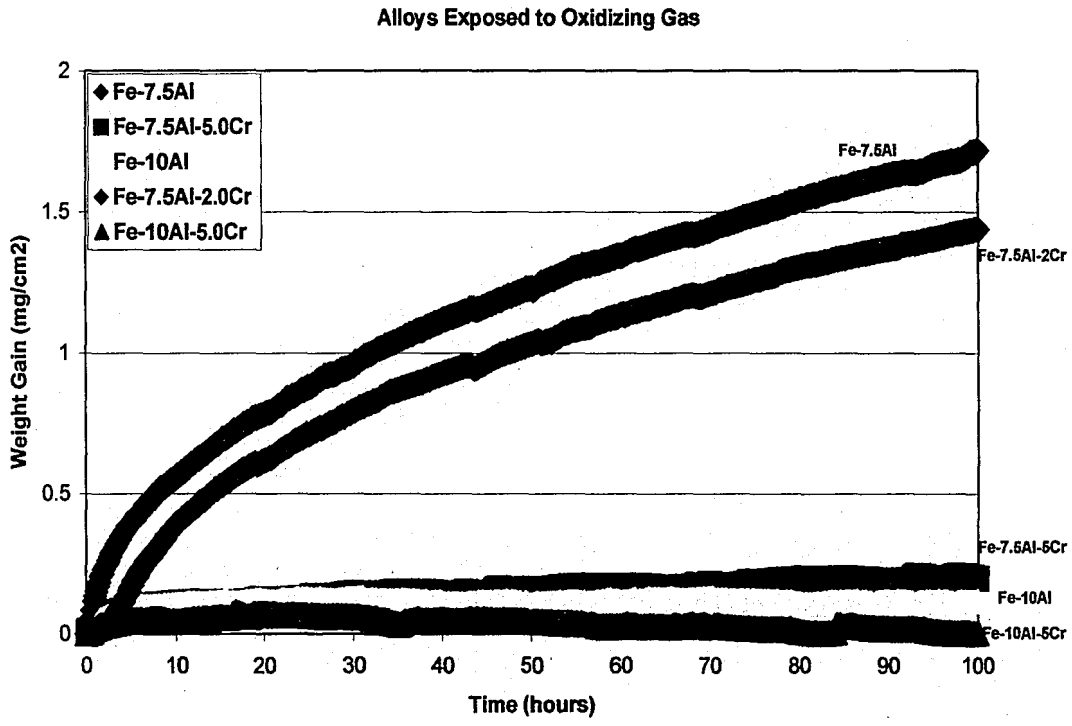

Figure 32 – Kinetic results for alloys exposed to the oxidizing environment.

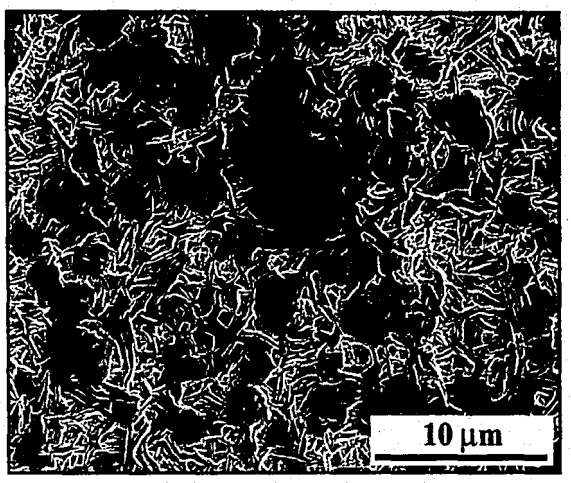

Fe-7.5Al

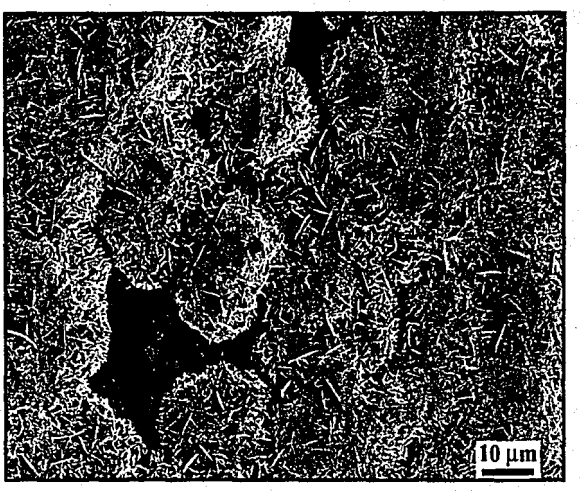

Fe-7.5Al-2Cr

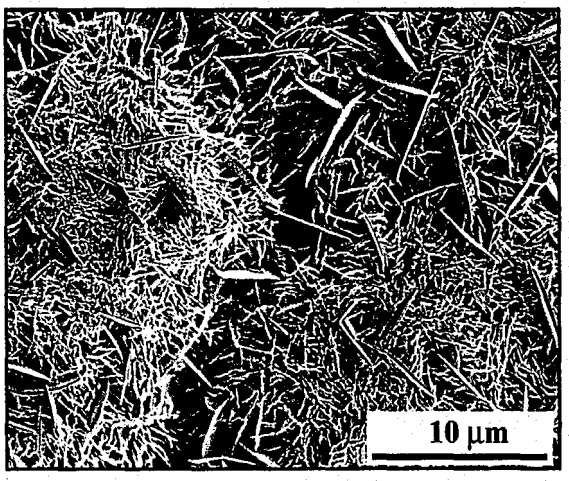

Fe-7.5Al-2Cr

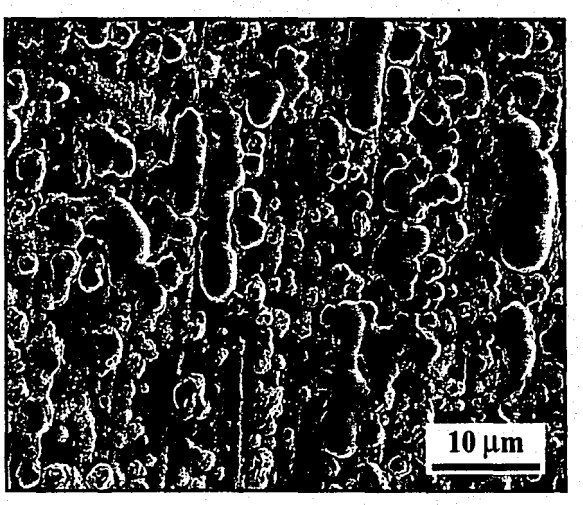

Fe-7.5Al-5Cr

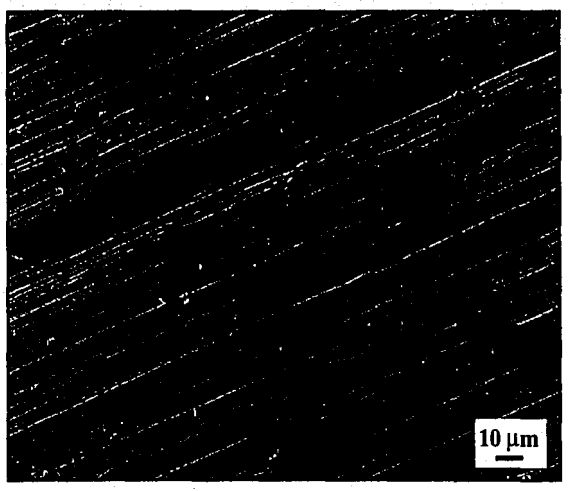

Fe-10Al-5Cr

Figure 33 – Selected samples exposed to the oxidizing environment at 500°C for 100 hours. Notice the differences in external scales that form depending on the alloy concentration.

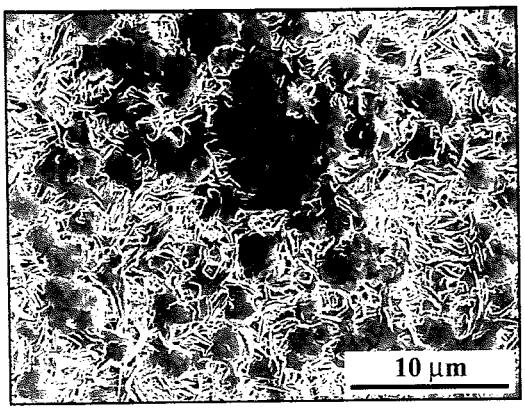

Fe-7.5Al

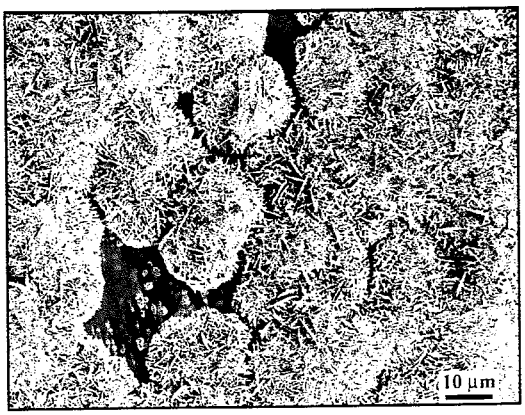

Fe-7.5Al-2Cr

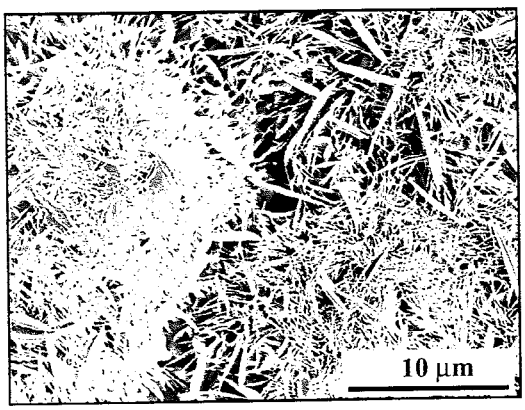

Fe-7.5Al-2Cr

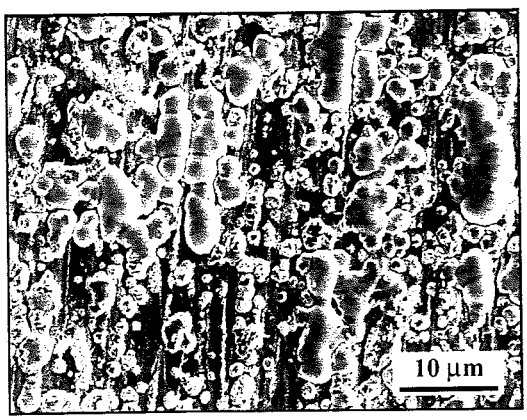

Fe-7.5Al-5Cr

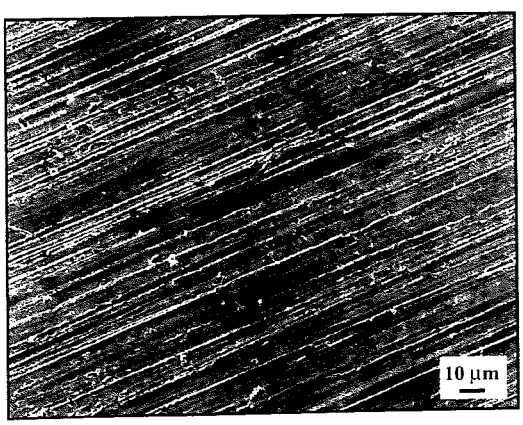

Fe-10Al-5Cr

Figure 33 – Selected samples exposed to the oxidizing environment at 500°C for 100 hours. Notice the differences in external scales that form depending on the alloy concentration.

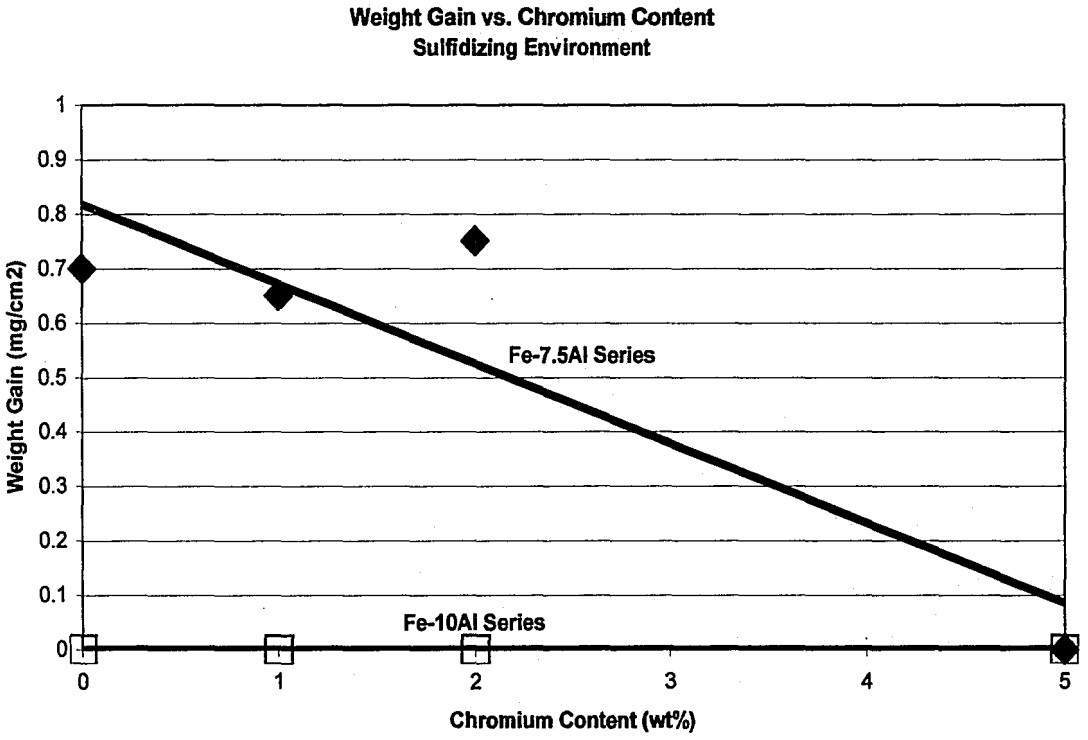

Figure 34 – Effect of chromium on the amount of weight gained after 100 hours of exposure to the sulfidizing gas at 500°C.

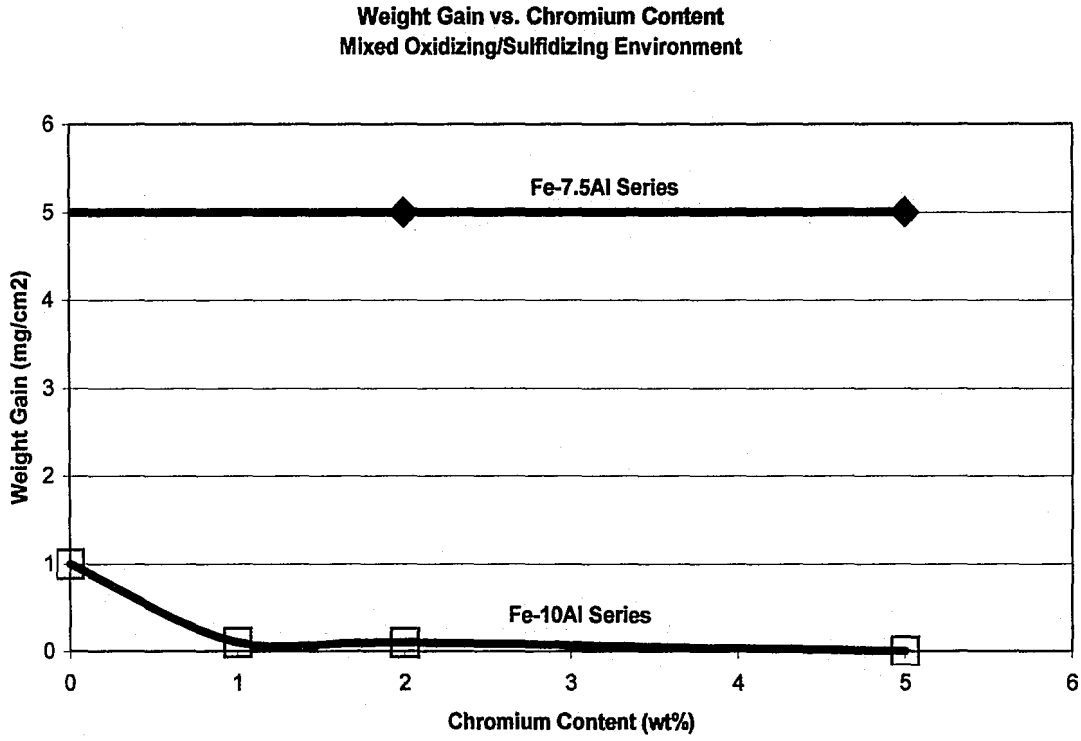

Figure 35 – Effect of chromium on the amount of weight gained after 100 hours of exposure to the mixed oxidizing/sulfidizing gas at 500°C.

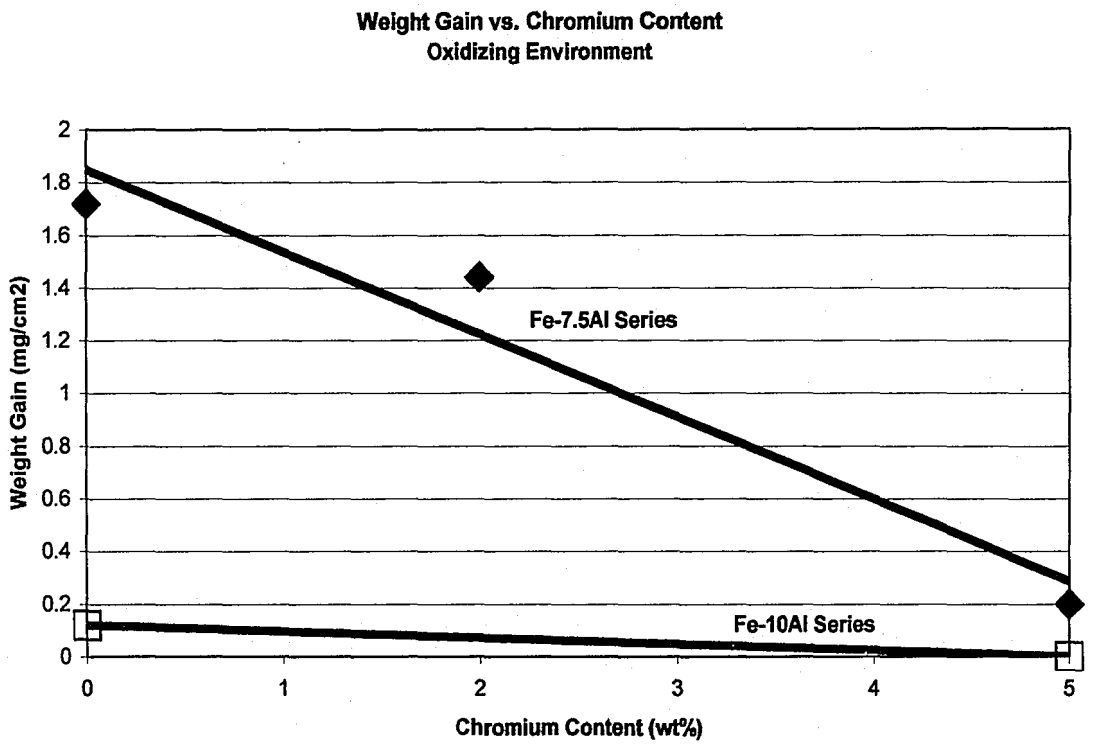

Figure 36 – Effect of chromium on the amount of weight gained after 100 hours of exposure to the oxidizing gas at 500°C.

It can also be seen that there are critical chromium concentrations that need to be met in order to significantly reduce the corrosion rates. These critical chromium concentrations required for protection in the sulfidizing gas, the mixed oxidizing/sulfidizing environment, and the oxidizing gas can be seen in Figure 34, Figure 35, and Figure 36, respectively. In the sulfidizing environment, the critical chromium level needed to be at least 5wt% for a Fe-Al-Cr ternary alloy containing 7.5wt%Al, but could be reduced to 2wt%Cr with the addition of 1.5wt%Ti. Again, alloys containing 10wt%Al were protective both with and without chromium additions in the sulfidizing gas. In the mixed oxidizing/sulfidizing gas, the critical chromium level needed to suppress rapid kinetics was seen to be 1wt%Cr when the aluminum concentration was 10wt%. Additions of chromium to alloys containing less aluminum did not significantly improve the corrosion resistance in this mixed environment. In the oxidizing environment, additions of 5wt% chromium helped to significantly reduce the corrosion kinetics for alloys containing 7.5wt%Al, but alloys containing 10wt%Al gained relatively no weight despite the chromium concentrations. Therefore, thermogravimetric measurements indicated that in order to reduce the corrosion rates in the highly sulfidizing environment alloys with 7.5wt%Al need at least 5wt%Cr and alloys with 10wt%Al require no chromium additions. On the other hand, in the mixed oxidizing/sulfidizing environment, 10wt%Al with 1wt%Cr additions are needed for protection. The oxidizing environment requires the weld overlays to have at least 10wt%Al but no chromium additions are needed to prevent rapid corrosion kinetics.

The integrity of the scales was explored further by observing whether the scale was completely uniform or if breakdown of the passive layer took place during 100 hours of exposure. The sulfidized Fe-10Al-2Cr sample was fractured in liquid N_2 and the surface can be seen in Figure 37. The majority of the surface was covered by a thin (<1μm) uniform layer (Figure 37a), but there were areas where initial stages of external corrosion were observed (Figure 37b). These small external corrosion products could not be seen when observing the surface on the SEM, but

were obvious when looking at the cross sections. Similar results were found for Fe-10Al-1Cr exposed to the mixed oxidizing/sulfidizing gas, which can be seen in Figure 38. It can be seen from these images that a thin passive layer was present over the entire sample surface, but large nodules could be seen protruding from the surface at several areas. When observing a non-protective sample (Fe-7.5Al-2Cr) exposed to the oxidizing environment, the thin passive layer could again be detected in areas where nodule growth did not completely cover the surface (Figure 39).

These results show that a passive layer, less than 1μm thick, formed on the alloys exposed to the three different environments. Non-protective samples, such as the one shown in Figure 39, still formed the passive layer but large areas of nodules were observed to overgrow this layer. Some alloys seemed to be protective according to the kinetic data, but after examination of the scales through microscopy nodules were observed on the samples. This was evident from Fe-10Al-2Cr exposed to the sulfidizing environment and Fe-10Al-1Cr exposed to the mixed oxidizing/sulfidizing gas. Each of these seemed to be protective after 100 hours in their respective environments according to the kinetic data, but small areas where the passive layer broke down resulted in external nodule growth. From these images it was concluded that kinetic data alone was not enough to determine the corrosion resistance of an alloy. The integrity of the passive layer needed to be observed as well in order to determine if nodule formation can occur and overgrow the protective scale after 100 hours, as seen in Figure 39d.

(a) (b)

Figure 37 – Fractured cross section of Fe-10Al-2Cr exposed to the sulfidizing gas. The thin passive layer covered the entire sample (a), but external nodules were sporadically observed across the surface (b).

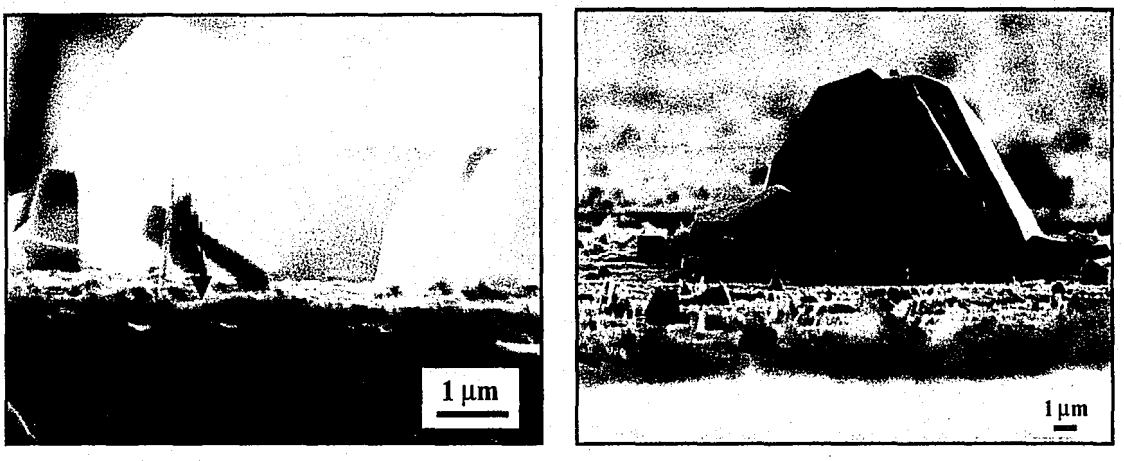

(a) (b)

Figure 38 – Fractured cross section of Fe-10Al-1Cr exposed to the mixed oxidizing/sulfidizing gas. The passive layer was observed over the entire cross section (a), but large nodules were seen protruding from the surface as well (b).

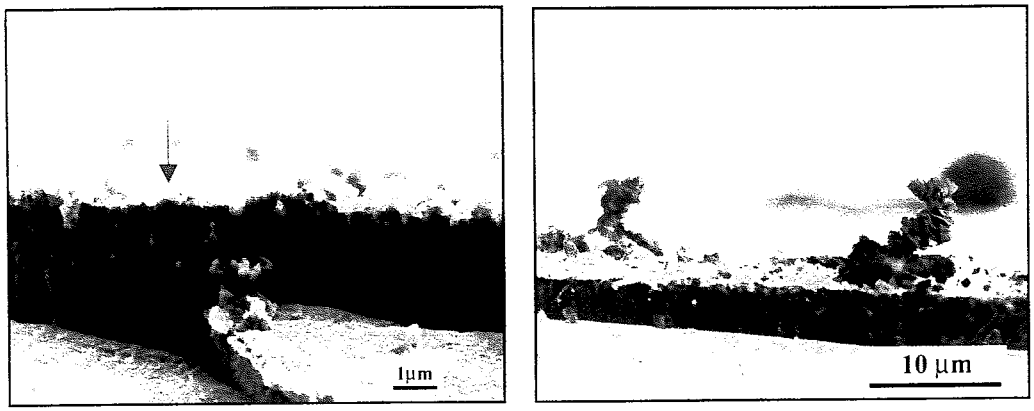

(a) (b)

Figure 37 – Fractured cross section of Fe-10Al-2Cr exposed to the sulfidizing gas. The thin passive layer covered the entire sample (a), but external nodules were sporadically observed across the surface (b).

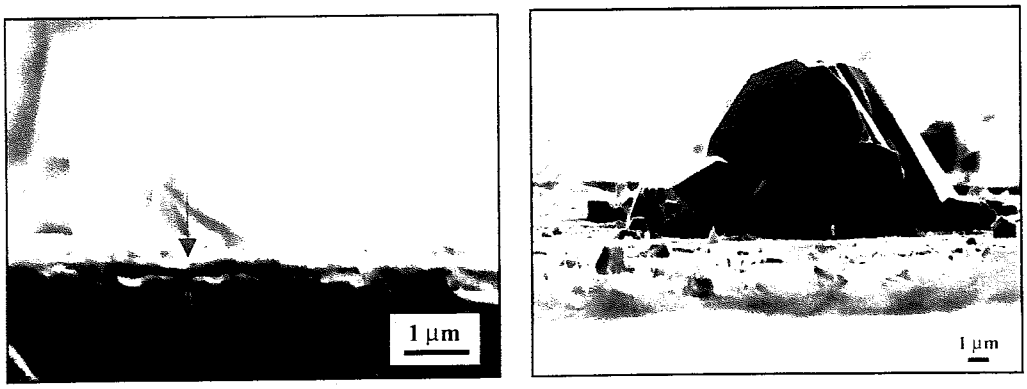

(a) (b)

Figure 38 – Fractured cross section of Fe-10Al-1Cr exposed to the mixed oxidizing/sulfidizing gas. The passive layer was observed over the entire cross section (a), but large nodules were seen protruding from the surface as well (b).

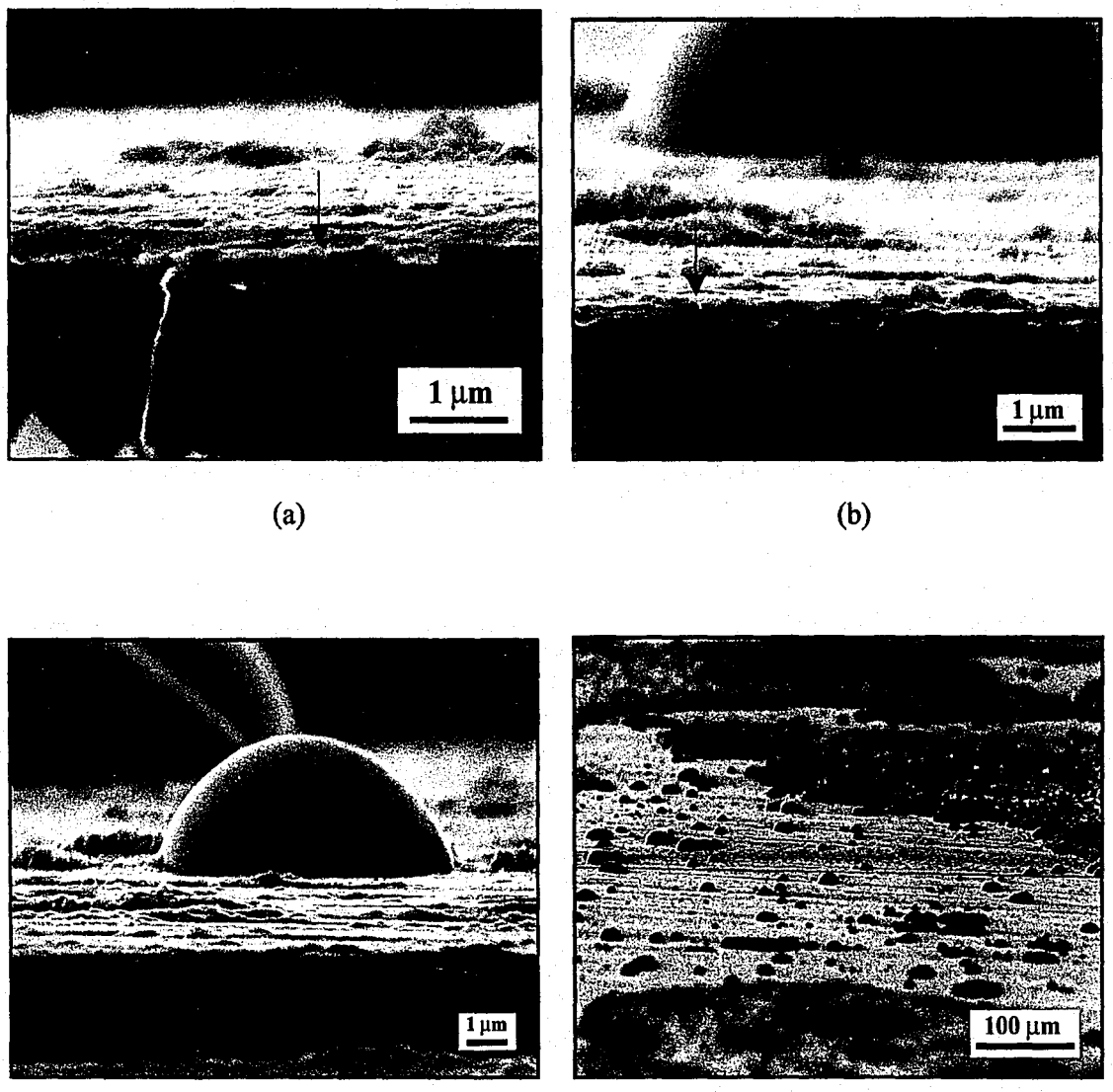

Figure 39 – Fe-7.5Al-2Cr exposed to the oxidizing environment. Note that the passive layer was observed to be less than 1μm thick (a) and (b) and the nodules that formed were several microns in diameter (c). The nodules were also observed to form at random sites and then grow together (d).

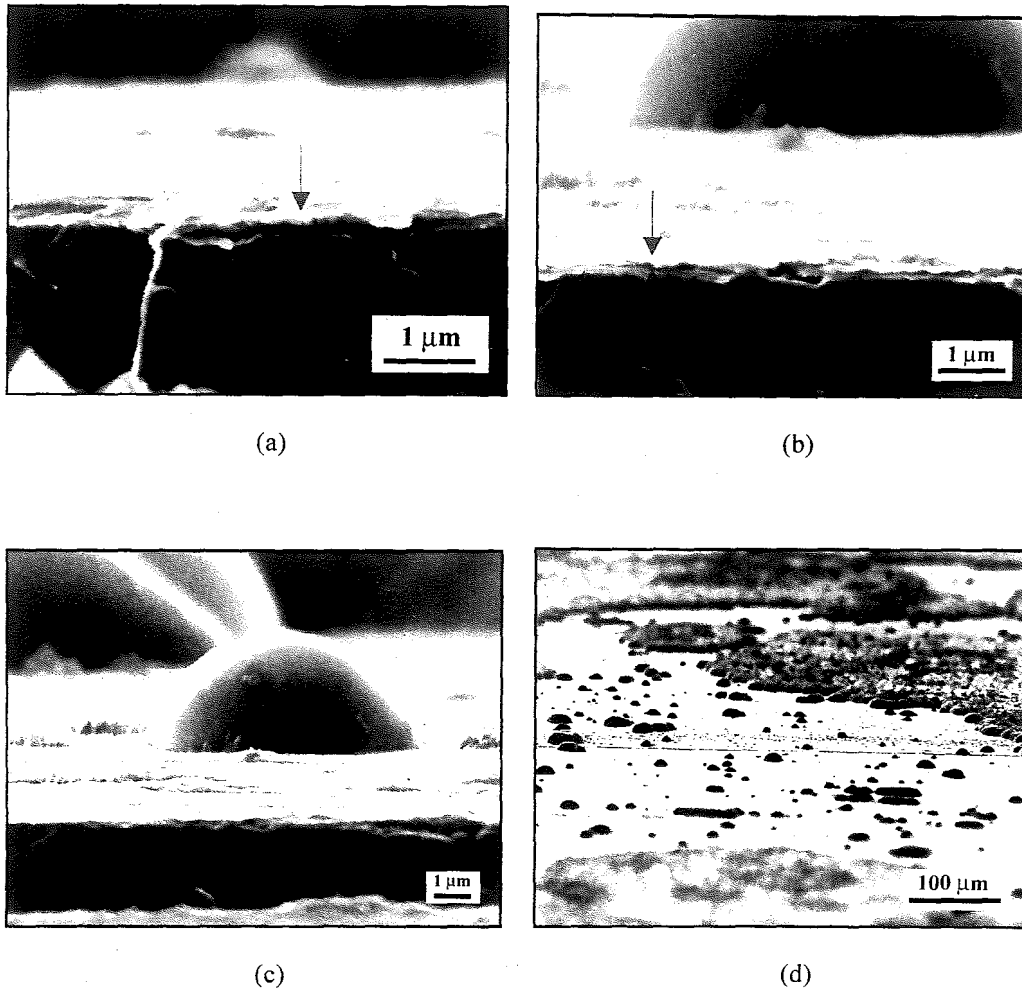

(a) (b)

(c) (d)

Figure 39 – Fe-7.5Al-2Cr exposed to the oxidizing environment. Note that the passive layer was observed to be less than 1μm thick (a) and (b) and the nodules that formed were several microns in diameter (c). The nodules were also observed to form at random sites and then grow together (d).

The formation of nodules through a protective layer has been discussed thoroughly in Chapter 1. Tomaszewicz and Wallwork described in detail the formation of iron oxide nodules on iron-aluminides at the initial stages of oxidation[47] (see Figure 20). Whereas, Banovic et. al. proposed the explanation that the development of nodules involving the mechanical breakdown of the protective layer[48] (see Figure 21). Although the mechanism responsible for the formation of nodules on alloys in these environments could not be determined by kinetic data and microscopy of the exposed samples alone, it was inferred that the amount of surface area covered by nodules was a direct indication of the ability of the passive layer to remain protective on the sample.

Sample surfaces were therefore observed to determine the amount of area covered by external nodule scales. The area fraction covered by nodule growth after 100 hours of exposure was plotted against the chromium content of the alloys to determine if there was an alloying dependence (Figure 40). It was found that alloys containing 7.5wt%Al were almost completely covered with nodules in the sulfidizing environment, but the amount of area covered by nodules decreased with an increase in the chromium concentration. On the other hand, alloys containing 7.5wt%Al exposed to the mixed oxidizing/sulfidizing atmosphere were completely covered with nodules, despite any chromium additions. Alloys containing 7.5wt%Al exposed to the oxidizing environment showed that the area covered by nodules had a chromium dependence, but additions of 5wt%Cr only reduced the amount of area covered by nodules to 60%. The amount of area covered by nodules on alloys containing 10wt%Al was seen depend on the amount of chromium present in the alloy for all three gases. Alloys containing 10wt%Al exposed to the sulfidizing atmosphere had very little area fraction covered by nodule growth on alloys without any chromium additions, and this area covered by nodules was reduced with the addition of chromium. On the other hand, there was a strong influence of chromium concentration in alloys containing 10wt%Al when exposed to the mixed oxidizing/sulfidizing environment. The area fraction covered by nodule growth ranged from approximately 80% for the binary Fe-10Al to 0%

for the ternary Fe-10Al-5Cr. In the oxidizing environment, the binary Fe-10Al alloy was covered by sporatic nodule growth, while adding 5wt%Cr to this alloy prevented any nodules from forming during 100 hours of exposure.

Comparing the kinetic results of the gases to microstructural observations, it can be seen that there is a discrepancy as to the amount of chromium required to obtain a protective coating. Although alloys containing 10wt%Al showed relatively no weight gains after 100 hours in the sulfidizing gas (Figure 24), the microstructure revealed that a small portion of the surface contained nodule growth. The formation of nodules will probably lead to increased corrosion kinetics at times longer than 100 hours. In the mixed oxidizing/sulfidizing gas, Fe-10wt%Al alloys containing at least 1%Cr seemed protective after 100 hours according to the kinetic data (Figure 29), but nodules were found on the surface of alloys containing less than 5wt%Cr. Although only a small number of nodules were present on these samples, at longer times further breakdown of the passive layer would probably occur, leading to rapid corrosion rates. In the oxidizing environment, alloys containing 10wt%Al seemed to be protective despite the chromium concentration in these alloys according to the kinetic data (Figure 32), but microstructural observations revealed that Fe-10Al had small areas where external nodule growth occurred. It was seen that 5wt%Cr was needed to totally prevent external nodules from forming during 100 hours of exposure.

From these results it can be seen that additions of chromium are beneficial to the corrosion resistance of iron-aluminum alloys at 500°C. Kinetic data alone cannot be used to accurately describe the high-temperature corrosion behavior of these alloys. Microstructural analysis must be performed as well, to determine the integrity of the passive scale. Observance of only a few nodules even after 100 hours of exposure could lead to unacceptable corrosion rates at longer times. The kinetic results are valuable as they can be used to find the possible candidates

for protective coatings, but careful microscopy must also be employed to determine if the alloy will continue to be protective at times greater than the exposure time.

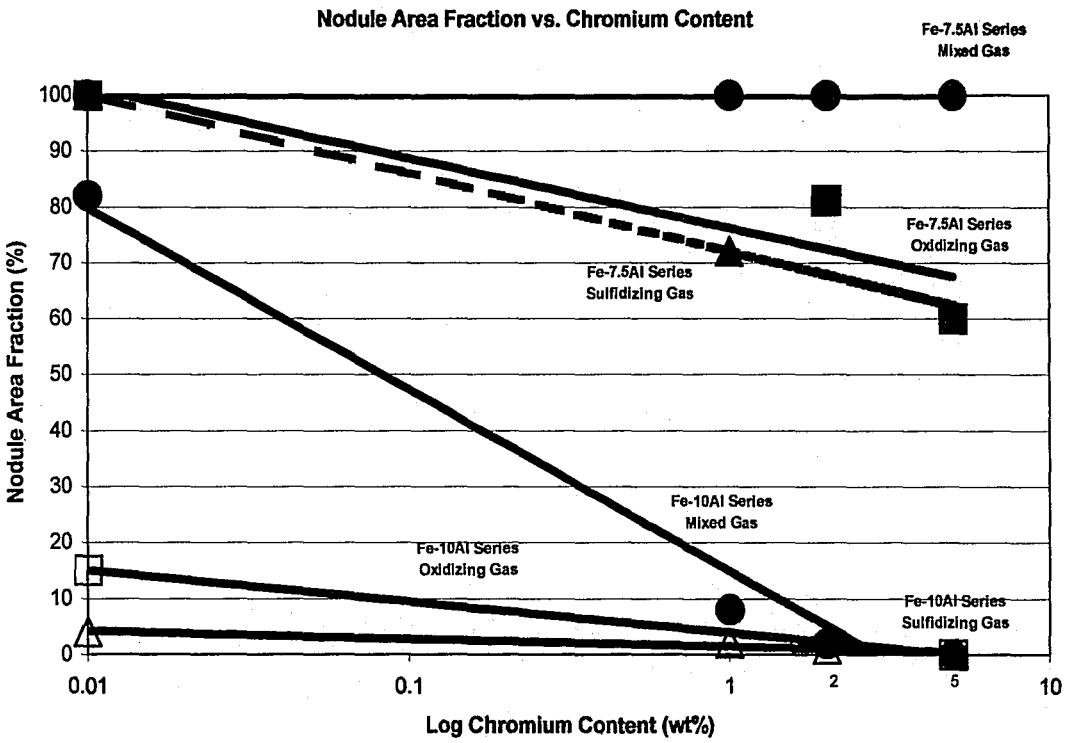

Figure 40 – Nodule Area Fraction vs. Chromium Content.

2.4 Conclusions

Several alloys were exposed to three corrosive environments: a sulfidizing atmosphere, a mixed oxidizing/sulfidizing environment, and an oxidizing environment. It was determined that:

- Aluminum concentrations need to be at least 10wt% in order to prevent rapid corrosion kinetics in all three atmospheres.
- Chromium additions were shown to help enhance formation of a passive layer and inhibit nodule growth for both environments as well.

- Titanium additions to the ternary Fe-Al-Cr alloy were shown to help decrease the corrosion kinetics in the sulfidizing environment, but they showed no significant improvement to the corrosion behavior in the mixed oxidizing/sulfidizing gas.
- A critical chromium concentration was required to change the corrosion kinetics from fairly rapid to sluggish, but this chromium level varied depending on the aluminum concentration and the environment.
- Electron microscopy observations showed that samples which appeared passive from kinetic results could still be problematic at long times due to the formation of nodules.
- The critical chromium level needed to inhibit nodule growth was found to be greater than the apparent critical chromium level needed to suppress weight gains.
- Kinetic data can help to determine likely candidates for protective coatings, but these candidates must be scrutinized using microscopic analysis to determine if nodule formation is prevented as well.

3. Chapter 3: Gas-Slag-Metal Corrosion Testing

"Corrosion Behavior of Fe-Al Based Alloys in Contact with Iron-Sulfide and Exposed to Mixed Oxidizing/Sulfidizing and Oxidizing Environments"

3.1 Introduction

Traditional high temperature corrosion testing has been carried out using gaseous corrosion tests where an alloy is exposed to a corrosive gas at elevated temperatures[1,3,8,66]. Although these tests are extremely valuable to determine potential corrosion resistant coatings, it has been shown that sulfur rich slag deposits can accumulate on the boiler tube walls and accelerate the corrosion rates as well[14]. Flame impingement from the burner can increase the amount of ash and unburned coal reaching the furnace walls. The accumulation of these deposits transforms in to a layer of slag, which can contain various reactive species as described in Chapter 1.2.2. As was previously mentioned, slag collections from actual boilers have shown that FeS can be found in areas where corrosion losses were high[15]. The FeS compounds found in these areas may be due to the decomposition of pyrite (FeS_2), which is found in the coal burnt in the furnace.

Therefore, in order to better simulate actual burner conditions, a relatively new test combining gaseous and solid-state corrosion was preformed on several Fe-Al based alloys. These tests made use of both gaseous and solid-state corrosion environments. The gas-slag-metal experiments were carried out using FeS_2 powder as the simulated slag and exposed to two gaseous environments, a mixed oxidizing/sulfidizing atmosphere and an oxidizing atmosphere.

3.2 Experimental Procedure

Alloys were cast by arc-melting high purity components under an argon atmosphere and drop cast into a water-cooled copper mold. Cast alloys were used because it was previously shown that the high temperature corrosion behavior of weld claddings could be explained by using cast alloys of equivalent composition[64]. Binary Fe-Al alloys, ternary Fe-Al-Cr alloys, and quaternary Fe-Al-Cr-Ti alloys that were used for this study can be seen back in Table 2 (p. 69), which gives the alloy compositions. Quartz ring corrosion experiments[97] were conducted using a Lindberg/Blue Horizontal Tube Furnace. The samples were ground to 600 grit and cleaned using acetone. The setup consisted of a quartz ring being super-glued onto the top of the ground surface. A predetermined amount (1680mg) of FeS_2 powder, supplied by American Minerals, was poured into the quartz ring without being packed and this setup was placed into the furnace. A schematic for the gas-slag-metal samples can be seen in Figure 41. Either the mixed oxidizing/sulfidizing gas or the oxidizing gas was then introduced into the furnace at a flow of 50mL/min. The samples were heated at a rate of 50°C/min and were held at 500°C for 100 hours. Water vapor present in both gases was injected into the furnace at a controlled rate. The components of the mixed oxidizing/sulfidizing and oxidizing gases used for exposure can be seen back in Table 3 (p. 71). The sulfur and oxygen partial pressures were calculated using the HSC Chemistry computer program[39]. Samples were carefully mounted in cold setting epoxy and their polished cross sections were observed using Light Optical Microscopy (LOM). LOM images were taken with an integrated camera on a LECO digital imaging system. The internal corrosion products observed in non-protective alloys were measured using an imaging program interfaced with a Light Optical Microscope. Quantitative chemical analysis data was obtained using a JEOL 733 Microprobe. A phi(ρz) correction scheme was used to correct for absorption and fluorescence of x-rays that occurs during Electron Probe Microanalysis (EPMA).

3.3 Results and Discussion

3.3.1 Mixed Oxidizing/Sulfidizing Environment

Polished cross sections of alloys containing 7.5wt%Al exposed to the mixed oxidizing/sulfidizing gas can be seen in Figure 42. It can be seen from this figure that Fe-7.5Al, Fe-7.5Al-1Cr, Fe-7.5Al-2Cr, and Fe-7.5Al-2Cr-1.5Ti all formed significant substrate and external corrosion scales after 100 hours of exposure. The external corrosion layers formed on these alloys were fairly non-uniform and appeared to be several microns thick. The substrate corrosion products formed on these alloys were uniform and appeared to be made up of multiple corrosion layers. Fe-7.5Al-5Cr formed a significant substrate scale, similar to the aforementioned alloys, but formed a very thin external corrosion layer. All alloys containing 10wt%Al tested in the mixed oxidizing/sulfidizing environment showed no signs of corrosion after 100 hours of exposure. These alloys can be seen in Figure 43.

Thickness measurements were taken of the substrate corrosion scales present on the alloys containing 7.5wt%Al to determine if chromium or titanium additions had any significant effect on the corrosion behavior of these alloys. The thickness measurements can be seen in Table 4. As can be seen from this table, some measured improvement to the substrate scale thickness was made only when 5wt%Cr was added. Although no measurements were made of the external corrosion product thickness, similar results were observed. Referring back to Figure 42, it can be seen that chromium additions of 1-2wt% may have made a slight improvement on the external corrosion layer thickness, but significant improvement occurred when 5wt%Cr was added. Titanium did not seem to make any improvement on the corrosion behavior of these alloys. Unfortunately due to problems with surface roughness within the substrate scale area on gas-slag-metal samples exposed to the mixed oxidizing/sulfidizing atmosphere, quantitative analysis could not be performed to help identify the phases that formed.

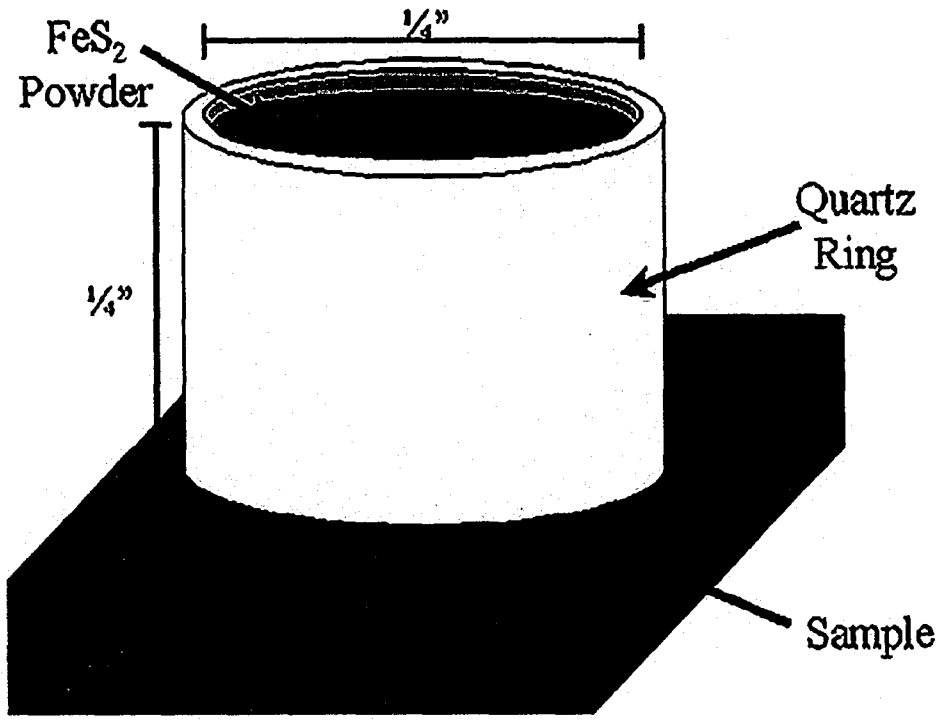

Figure 41 – Schematic diagram of the gas-slag-metal experimental setup.

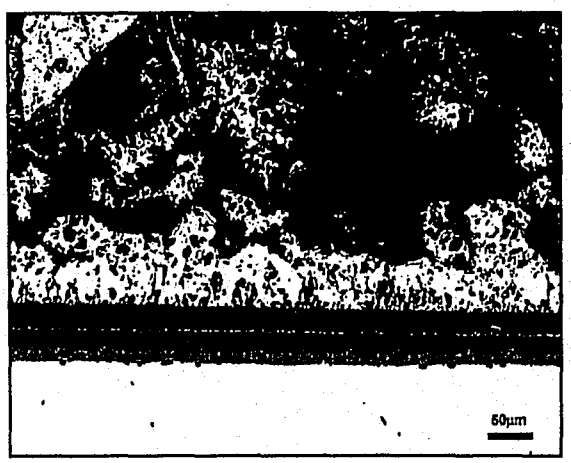

Fe-7.5Al

Fe-7.5Al-1Cr

Fe-7.5Al-2Cr

Fe-7.5Al-5Cr

Fe-7.5Al-2Cr-1.5Ti

Figure 42 – Samples containing 7.5wt%Al exposed to FeS_2 powder and the mixed oxidizing/sulfidizing environment at 500°C for 100 hours.

External Corrosion Scale
Epoxy
Substrate Corrosion Scale

Fe-7.5Al

Fe-7.5Al-1Cr

Fe-7.5Al-2Cr

Fe-7.5Al-5Cr

Fe-7.5Al-2Cr-1.5Ti

Figure 42 – Samples containing 7.5wt%Al exposed to FeS_2 powder and the mixed oxidizing/sulfidizing environment at 500°C for 100 hours.

Table 4 – Substrate corrosion scale thickness for samples exposed to FeS_2 powder and the mixed oxidizing/sulfidizing environment.

Alloy	Thickness (μm)	Standard Deviation
Fe-7.5Al	30.5	2.1
Fe-7.5Al-1Cr	19.7	4.3
Fe-7.5Al-2Cr	26.3	2.8
Fe-7.5Al-5Cr	11.3	1.8
Fe-7.5Al-2Cr-1.5Ti	28.6	2.2

3.3.2 Oxidizing Environment

Polished cross sections of alloys containing 7.5wt%Al exposed to the oxidizing gas can be seen in Figure 44. It can be seen from this figure that all of the alloys containing 7.5wt%Al developed thick external corrosion layers, which were at least 100μm thick, as well as uniform substrate corrosion scales. The external corrosion scale seemed to consist of two distinct layers. The layer directly adjacent to the metal substrate was observed to contain a large amount of porosity while the outer layer of the external scale was a thick solid layer that contained relatively no pores. The substrate corrosion products observed on these alloys seemed to consist of multiple layers and cracks could be seen to run through the substrate corrosion products perpendicular to the substrate/external corrosion scale interface. Some samples, namely Fe-7.5Al and Fe-7.5Al-2Cr-1.5Ti, showed cracks that penetrated into the base metal as well. Corrosion products were observed within some of the cracks (see Figure 44). This would indicate that the cracks formed sometime during exposure where corrosive species could penetrate into the substrate. These cracks can act as fast pathways for corrosion to take place and are therefore very detrimental to

the corrosion resistance of the alloy. Fe-7.5Al-1Cr contained cracks that ran both parallel and perpendicular to the substrate/external corrosion scale interface. The only alloy containing 7.5wt%Al that did not show significant cracking of the internal scale was Fe-7.5Al-5Cr, which contained the smallest substrate corrosion layer. This may indicate that the perpendicular cracks observed in these samples are related to the thickness of the substrate corrosion scales.

Thickness measurements were again taken of the internal corrosion scales in these alloys to determine if the alloying additions had any significant affect on the corrosion behavior. The internal corrosion scale thickness measurements for these alloys exposed to the oxidizing gas can be seen in Table 5. Similarly to the results obtained when these alloys were exposed to the mixed oxidizing/sulfidizing gas, there was no significant effect of chromium on the substrate scale thickness until 5wt%Cr was added. It was also observed that cracking of the substrate corrosion scale occurred in all samples containing thickness layers in excess of approximately 45μm. The external corrosion layer thickness seemed to decrease slightly with the addition of chromium, but the scales were too convoluted to obtain relevant thickness data. Again the addition of titanium to Fe-7.5Al-2Cr did not have any beneficial affect on the corrosion resistance of this alloy.

Alloys containing 10wt%Al exposed to the oxidizing gas can be seen in Figure 45. It can be seen from this figure that all alloys, with the exception of Fe-10Al-1Cr, formed no significant substrate or external corrosion product during 100 hours of exposure. On the other hand, Fe-10Al-1Cr developed both substrate and external corrosion layers, which appeared to look similar to the corrosion products formed on the alloys containing 7.5wt%Al exposed to the oxidizing environment. The substrate corrosion layer formed on Fe-10Al-1Cr was measured to be 92.0 ± 8.2μm thick and cracking could be seen both parallel and perpendicular to the internal/external corrosion layer interface. This specimen was believed to not be representative of the Fe-10Al series of alloys, but no explanation of this unexpected result can be given at this time.

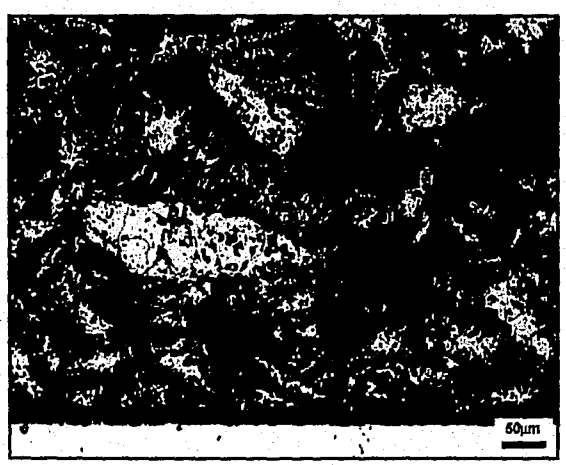

Fe-10Al

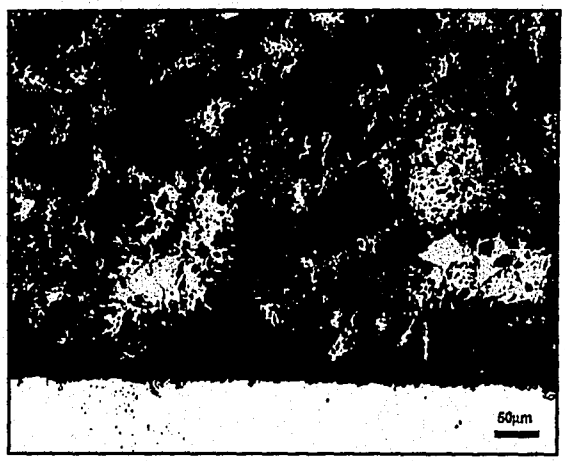

Fe-10Al-1Cr

Fe-10Al-2Cr

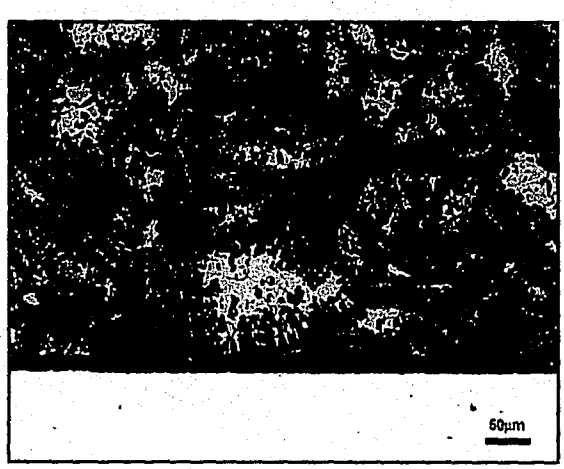

Fe-10Al-5Cr

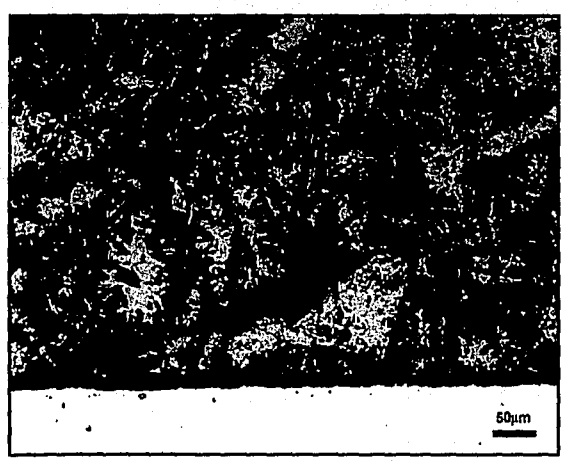

Fe-10Al-2Cr-1.5Ti

Figure 43 – Samples containing 10wt%Al exposed to FeS_2 powder and the mixed oxidizing/sulfidizing environment at 500°C for 100 hours.

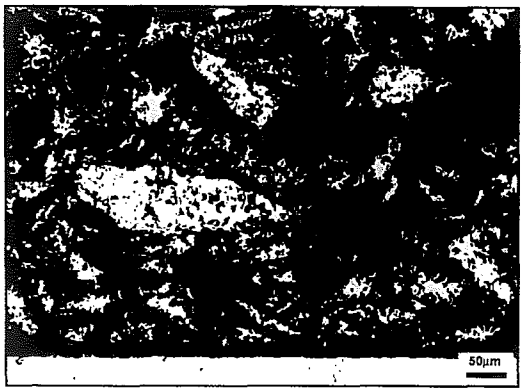

Fe-10Al

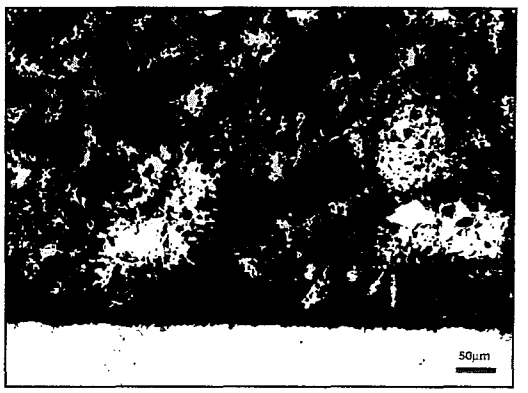

Fe-10Al-1Cr

Fe-10Al-2Cr

Fe-10Al-5Cr

Fe-10Al-2Cr-1.5Ti

Figure 43 – Samples containing 10wt%Al exposed to FeS_2 powder and the mixed oxidizing/sulfidizing environment at 500°C for 100 hours.

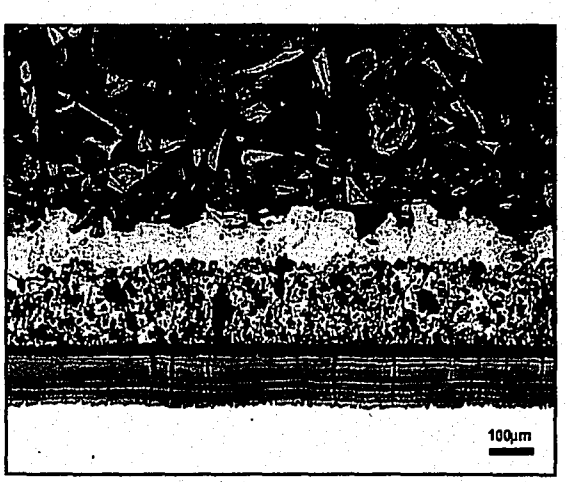

Fe-7.5Al

Fe-7.5Al-1Cr

Fe-7.5Al-2Cr

Fe-7.5Al-5Cr

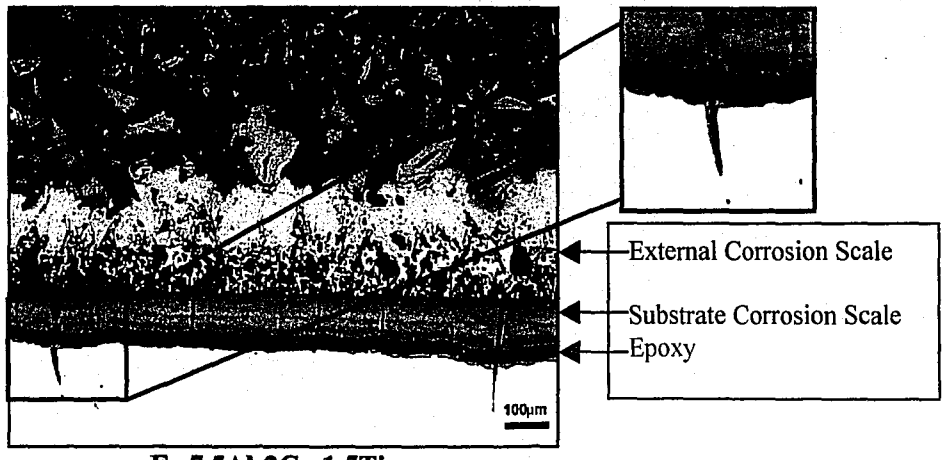

Fe-7.5Al-2Cr-1.5Ti

Figure 44– Samples containing 7.5wt%Al in contact with FeS_2 powder and exposed to the oxidizing environment at 500°C for 100 hours. Note the corrosion product that formed within the penetrating crack in the Fe-7.5Al-2Cr-1.5Ti sample.

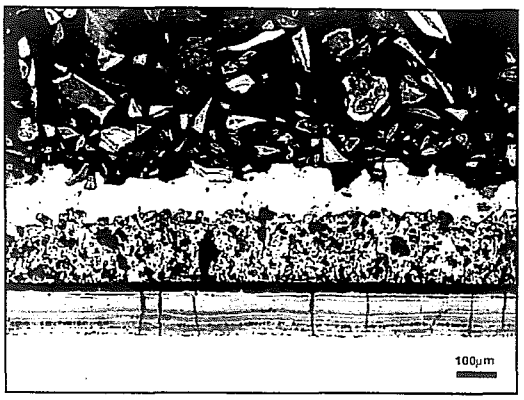

Fe-7.5Al

Fe-7.5Al-1Cr

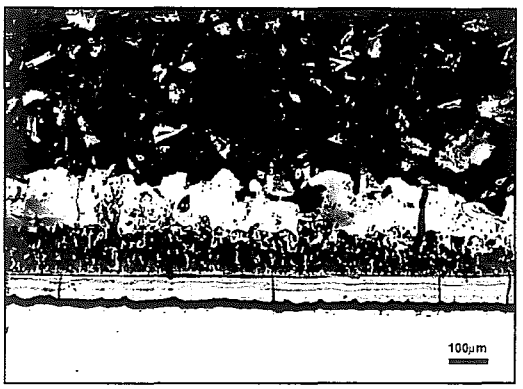

Fe-7.5Al-2Cr

Fe-7.5Al-5Cr

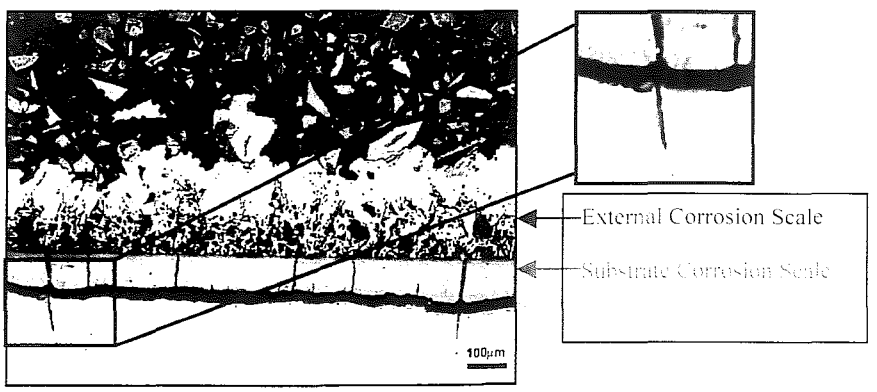

Fe-7.5Al-2Cr-1.5Ti

Figure 44– Samples containing 7.5wt%Al in contact with FeS_2 powder and exposed to the oxidizing environment at 500°C for 100 hours. Note the corrosion product that formed within the penetrating crack in the Fe-7.5Al-2Cr-1.5Ti sample.

From these results it can be seen that 10wt%Al is required to prevent significant corrosion to take place in both the mixed oxidizing/sulfidizing and oxidizing environments when alloys are in contact with FeS_2. The additions of less than 5wt%Cr had little effect on the corrosion behavior of alloys containing 7.5wt%Al, but adding 5wt%Cr helped to decrease the amount of corrosion that occurred on these alloys. Titanium additions again had no significant effect on the corrosion behavior of any of the alloys in either environment.

Table 5 – Substrate corrosion layer thickness for samples exposed to FeS_2 powder and the oxidizing environment.

Alloy	Thickness (μm)	Standard Deviation
Fe-7.5Al	103.1	12.5
Fe-7.5Al-1Cr	69.2	2.0
Fe-7.5Al-2Cr	91.3	1.6
Fe-7.5Al-5Cr	43.3	2.0
Fe-7.5Al-2Cr-1.5Ti	88.4	19.3

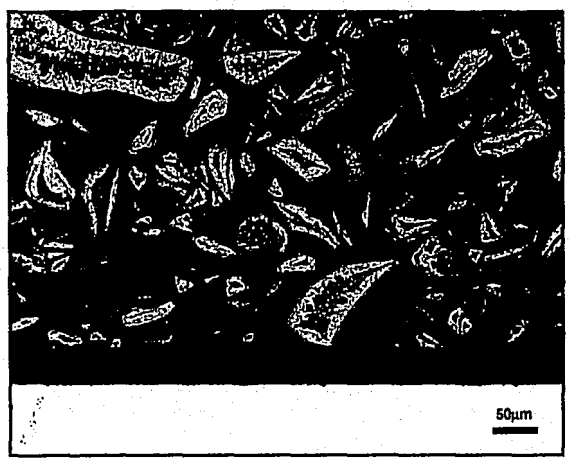

Fe-10Al

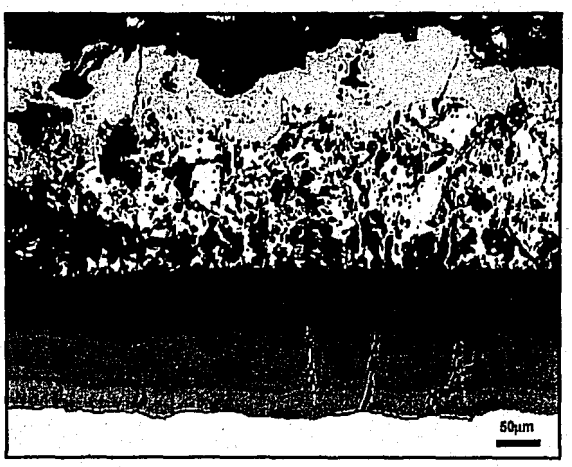

Fe-10Al-2Cr

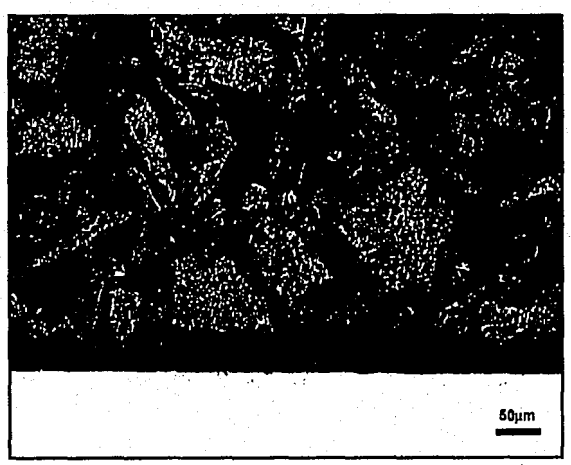

Fe-10Al-1Cr

Fe-10Al-5Cr

Fe-10Al-2Cr-1.5Ti

Figure 45 – Samples containing 10wt%Al exposed to FeS_2 powder and the oxidizing environment at 500°C for 100 hours.

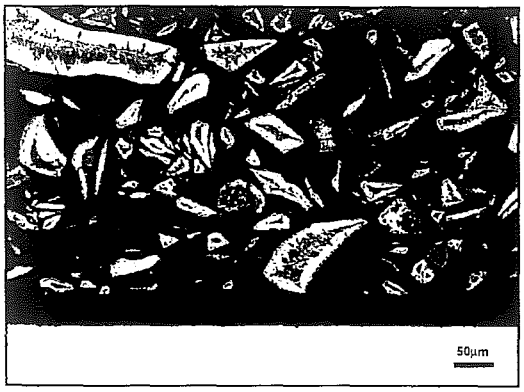

Fe-10Al

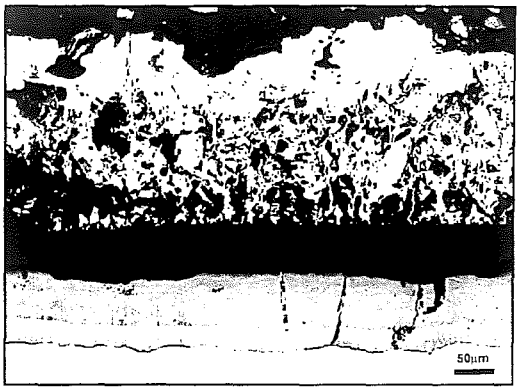

Fe-10Al-2Cr

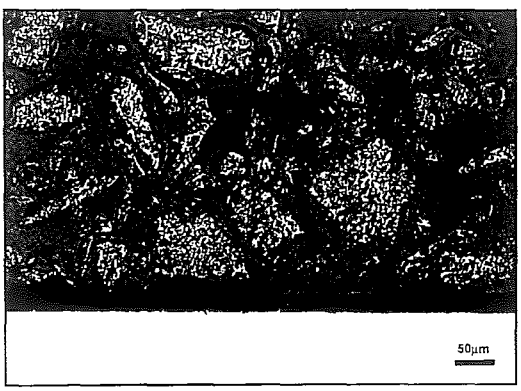

Fe-10Al-1Cr

Fe-10Al-5Cr

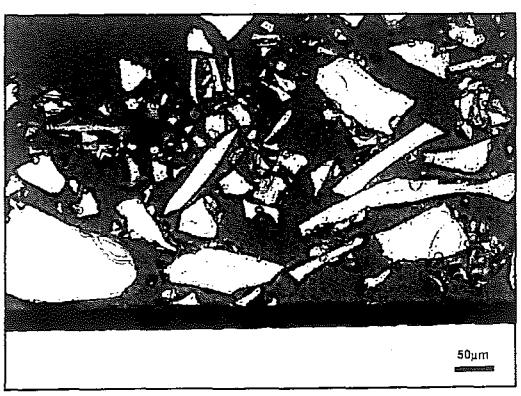

Fe-10Al-2Cr-1.5Ti

Figure 45 – Samples containing 10wt%Al exposed to FeS_2 powder and the oxidizing environment at 500°C for 100 hours.

To better understand the types of reactions that took place during the gas-slag-metal experiments, the substrate corrosion scales that formed during exposures to the oxidizing environment were considered in greater detail by obtaining quantitative compositional data on the individual internal corrosion layers. Quantitative compositional data was obtained for two samples exposed to the oxidizing environment, Fe-7.5Al and Fe-7.5Al-2Cr, by using Electron Microprobe Analysis (EPMA). Three line scans were taken on different areas for each sample and the points of analysis were selected in an attempt to obtain data for the individual corrosion products that comprised the entire substrate corrosion layer. A phi(ρz) correction scheme was applied to the raw data to correct for absorption and fluorescence of x-rays that occurs during analysis.

The first, second, and third areas where compositional traces were taken for Fe-7.5Al exposed to the oxidizing environment can be seen in Figure 46, Figure 47 and Figure 48, respectively. It can be seen from these figures that although each area had a similar structure, the observed individual layers vary from area to area. For example, the first and second areas (Figure 46 and Figure 47, respectively) had very similar layered structures, but the third area (Figure 48) contains more layers than the previous two. From the layers it was observed that there were two distinct regions in the substrate corrosion scale. A light corrosion scale region could be seen adjacent to the base metal and a darker scale could be seen towards the alloy surface. From the compositional data it could be seen that the substrate scale formed on Fe-7.5Al was rich in iron, aluminum, oxygen, and sulfur. Three EPMA line traces were also conducted on the Fe-7.5Al-2Cr sample exposed to the oxidizing environment and the first, second, and third scans taken on this sample can be seen in Figure 49, Figure 50, and Figure 51, respectively.

Although each individual phase could not be identified from the EPMA compositional data due to the layer size and variations caused by surface roughness, some general statements can be made about the substrate corrosion layer. One of the first tools that can be used to help

identify the phases that may be present in the substrate corrosion layer is the phase stability diagram. According to the Fe-O-S and Al-O-S phase stability diagrams shown in Figure 52, the stable phases that should be present in the oxidizing environment are Fe_2O_3 and Al_2O_3. By performing some simple calculations using the molecular weights of iron, aluminum, and oxygen and assuming that the amount of Fe_2O_3 and Al_2O_3 are the same within the substrate corrosion scale, approximate weight fractions for each element can be determined. From these calculations it was found that if Fe_2O_3 and Al_2O_3 are the only phases present and they are present in a 1:1 ratio (50%Fe_2O_3, 50%Al_2O_3), the weight fractions should be: 42.7wt%Fe, 20.6wt%Al, and 36.7wt%O. Comparing these values to the EPMA data found for the Fe-7.5Al sample it can be seen that the iron and aluminum levels are in good agreement with the simple weight fraction calculations. The iron and aluminum compositions for the substrate corrosion layer within the Fe-7.5Al sample are approximately 40wt%Fe and 20wt%Al. The aluminum concentration directly adjacent to the base metal was less than 20wt%Al, most likely due to an aluminum depleted region adjacent to the base metal caused by aluminum diffusion away from the metal towards the surface of the alloy.

One discrepancy with this analysis was that the oxygen levels observed through EPMA data were lower than the calculated values. Sulfur was also observed within the substrate corrosion layer, which was not predicted according to the phase stability diagrams. The presence of sulfur could possibly be explained from the FeS_2 powder that was in contact with the metal during exposure. Reactions between the gaseous environment and the slag powder could result in a local increase in the sulfur partial pressure at the metal/slag interface. Looking at the phase stability diagrams in Figure 52 it can be seen that a slight increase in sulfur partial pressure could result in the formation of either $Fe_2(SO_4)_3$ or $Al_2(SO_4)_3$, which could change the sulfur and oxygen compositions within the substrate corrosion layer.

Another major variable that could cause a discrepancy between the calculations based on the phase stability diagrams and the EPMA data is the assumption that the phases located within the substrate corrosion layer are in a 1:1 ratio. Adjusting this ratio slightly can have a significant effect on the substrate corrosion layer composition. Another variable is that the oxygen and sulfur partial pressures will decrease traveling inward from the surface of the alloy. This indicates that the stable phases will most likely change through the substrate corrosion layer. Differences in the stable phases based on the phase stability diagrams could possibly explain the increase in the sulfur composition and the decrease in the oxygen concentration observed approximately half-way through the composition trace, where the lighter scale changes over to a darker colored scale. Changes in either the stable phases or the amount of each phase present could result in the shift in the sulfur and oxygen concentrations within this region. Other factors that could contribute to the complexity of the scale interpretation are solid solubility between phases, porosity in the substrate corrosion scale, and errors associated with both the phase stability diagrams and collecting EPMA data. Overall, it can be said that the most probable phases present in the Fe-7.5Al substrate corrosion scale are Fe_2O_3, $Fe_2(SO_4)_3$, Al_2O_3, and $Al_2(SO_4)_3$. These phases are most likely to be present but the amount of each phase and where the phases are located cannot be determined using this technique.

Analysis on the Fe-7.5Al-2Cr sample exposed to the oxidizing environment was more difficult than analysis performed on the Fe-7.5Al sample, when making the same assumptions as was made for analysis of the Fe7.5Al sample. According to the Cr-O-S Phase Stability Diagram (shown in Figure 53) Cr_2O_3 should be the chromium containing stable phase. Again, due to the FeS_2 powder in contact with the metal, the sulfur partial pressure could increase slightly and change the stable phase from Cr_2O_3 to $Cr_2(SO_4)_3$. Simple analysis of the predicted weight fractions for each element, assuming a 1:1:1 ratio, could not be correlated with the EPMA data for the chromium-containing sample. As with the Fe-7.5Al sample, the most probable phases

present in the Fe-7.5Al-2Cr substrate corrosion layer are Fe_2O_3, $Fe_2(SO_4)_3$, Al_2O_3, $Al_2(SO_4)_3$, Cr_2O_3, and $Cr_2(SO_4)_3$.

Some general trends can also be pointed out from these compositional traces performed on the two samples, Fe-7.5Al and Fe-7.5Al-2Cr. It can be seen from the traces performed on both samples that, generally speaking, the aluminum concentration increased from the base metal towards the surface. A depleted region was observed in the base metal adjacent to the substrate corrosion scale. The nominal composition of the as-received samples was approximately 7.5wt%Al and the metal had a composition of approximately 5wt%Al adjacent to the metal/substrate corrosion layer interface. The chromium trace performed on the Fe-7.5Al-2Cr also showed a slight increase in the chromium level from the base metal towards the metal surface. These observations would indicate that aluminum and chromium diffused outward from the metal to the surface of the alloy, which is consistent with the general observation that high temperature corrosion occurs by outward cation diffusion.

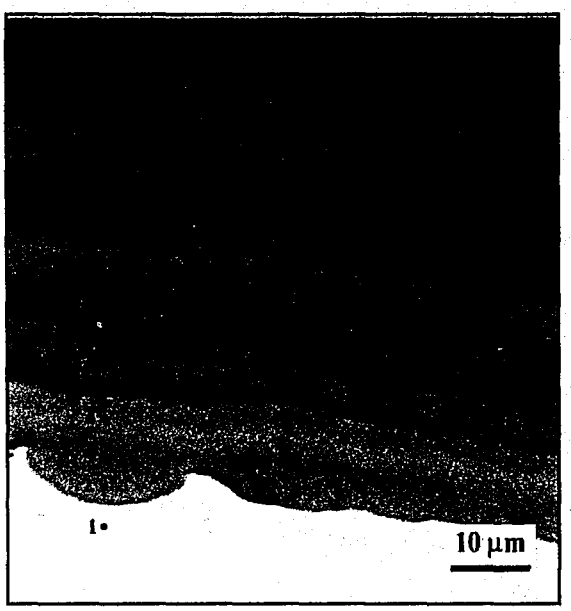

(a)

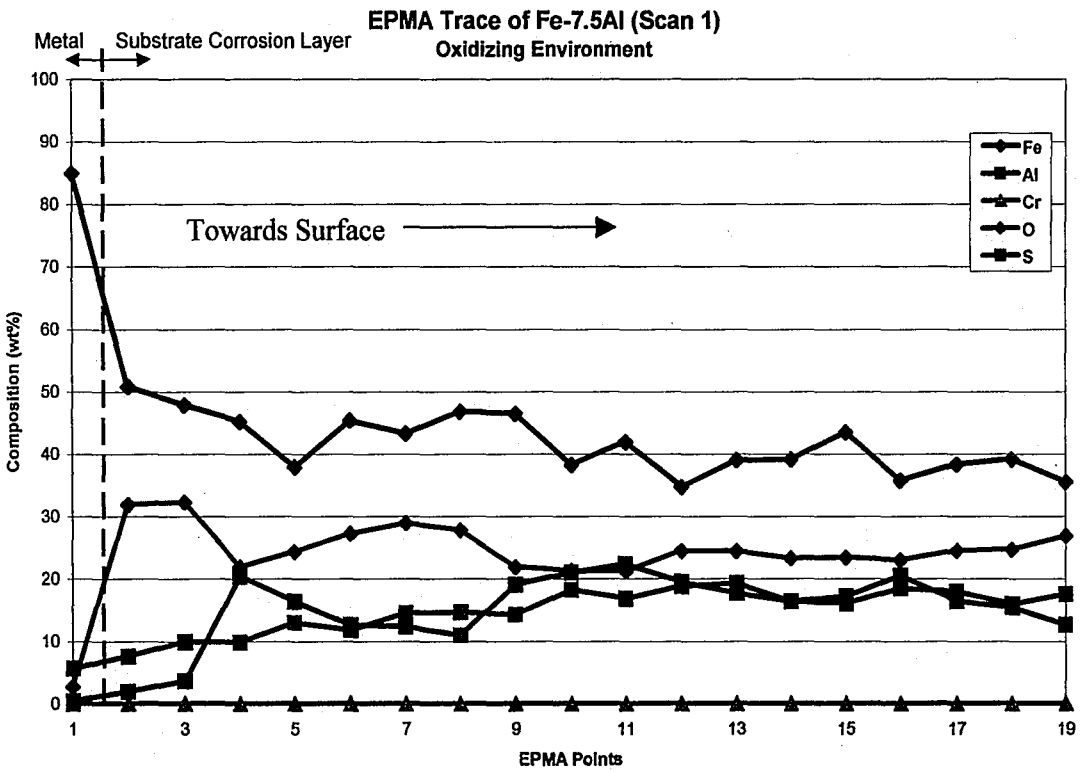

(b)

Figure 46 – EPMA trace (Scan 1) across the internal scale for Fe-7.5Al exposed to the oxidizing environment while in contact with the FeS_2 powder.

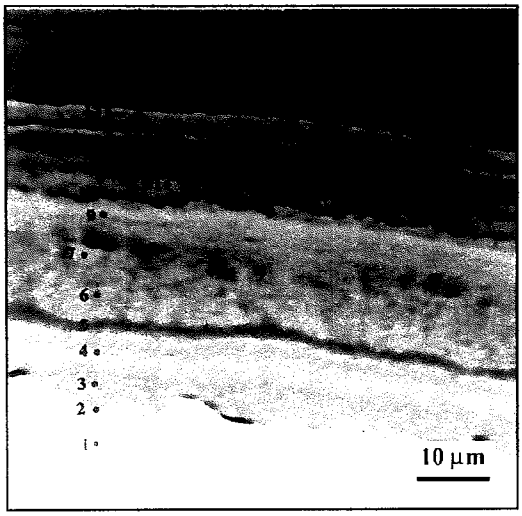

(a)

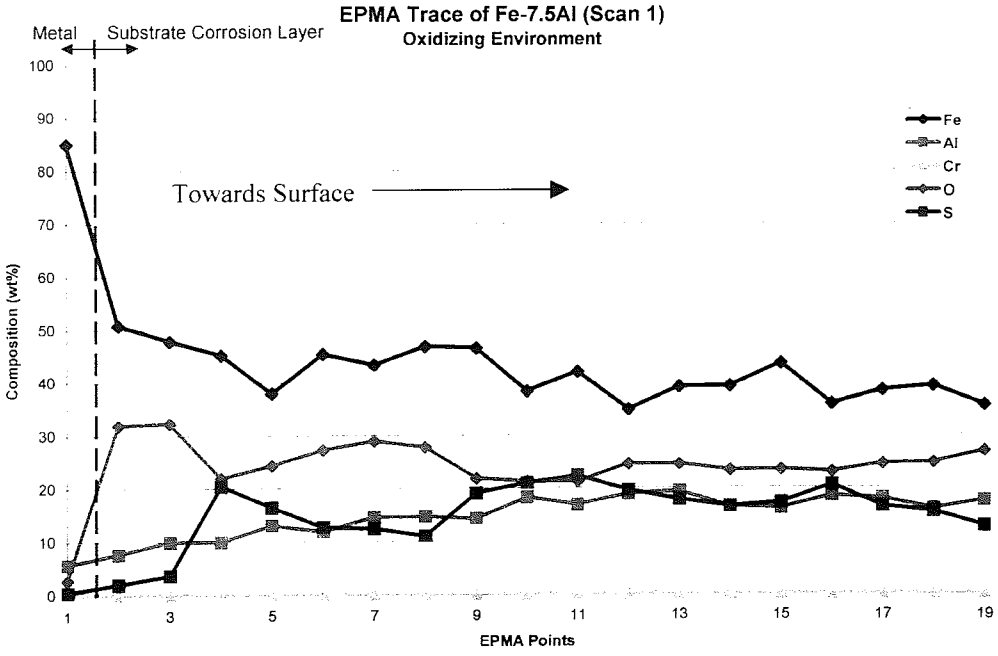

(b)

Figure 46 – EPMA trace (Scan 1) across the internal scale for Fe-7.5Al exposed to the oxidizing environment while in contact with the FeS_2 powder.

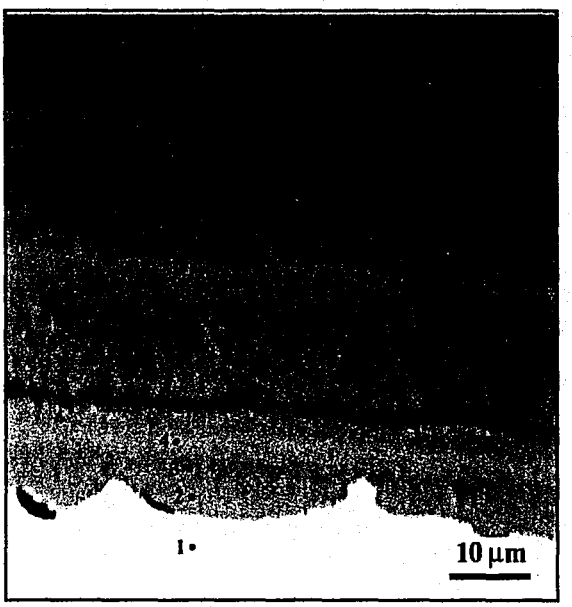

(a)

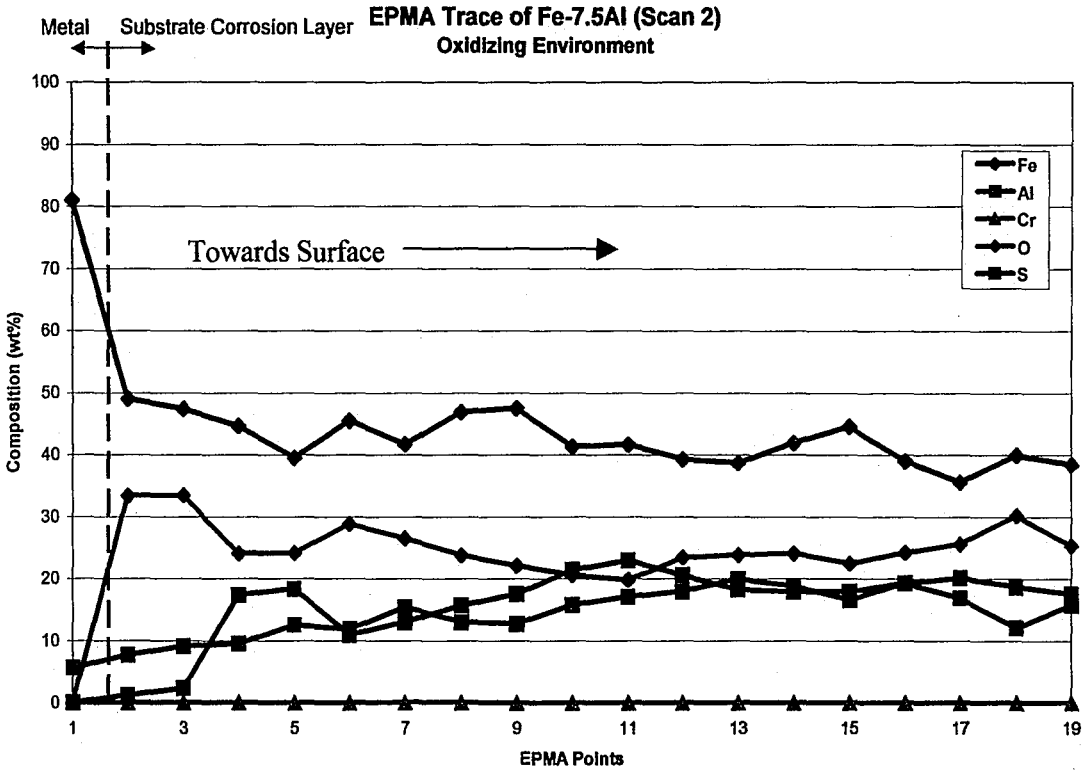

(b)

Figure 47 – EPMA trace (Scan 2) across the internal scale for Fe-7.5Al exposed to the oxidizing environment while in contact with the FeS_2 powder.

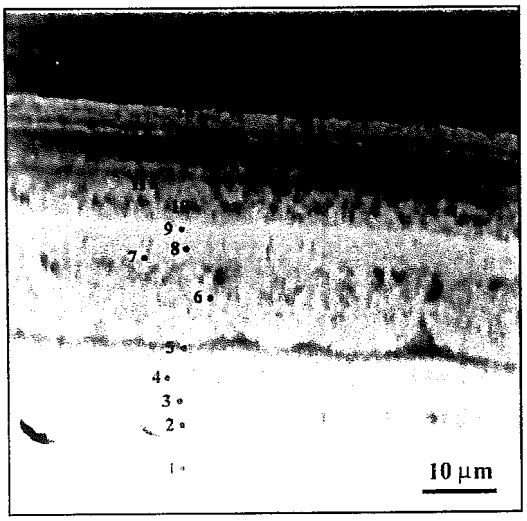

(a)

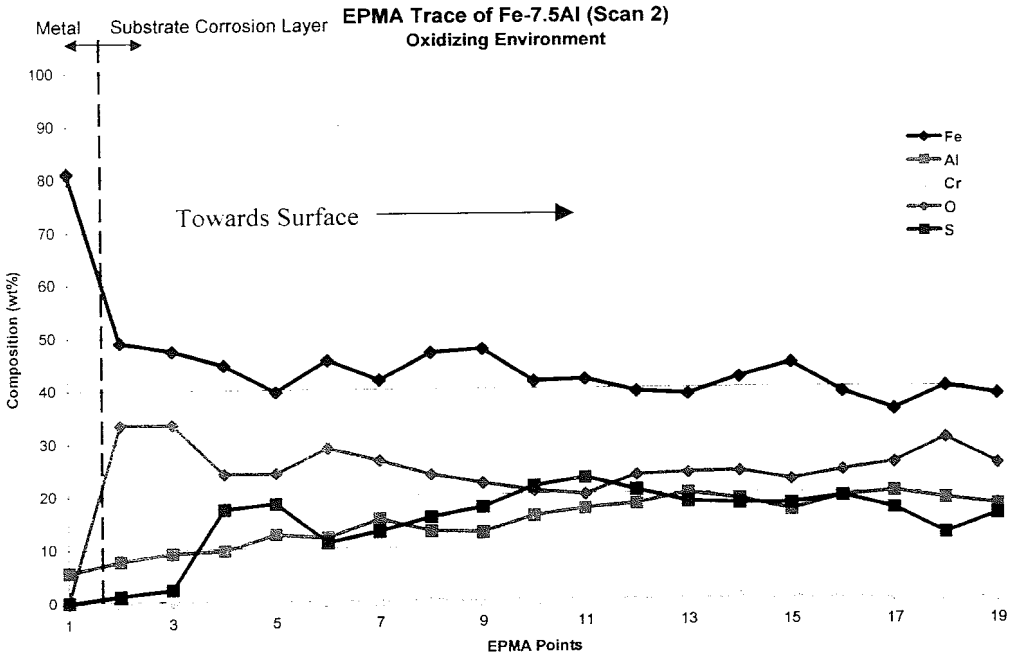

(b)

Figure 47 – EPMA trace (Scan 2) across the internal scale for Fe-7.5Al exposed to the oxidizing environment while in contact with the FeS_2 powder.

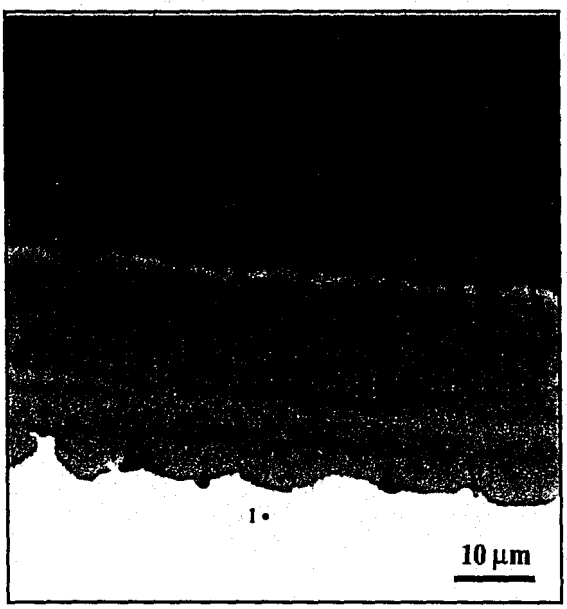

(a)

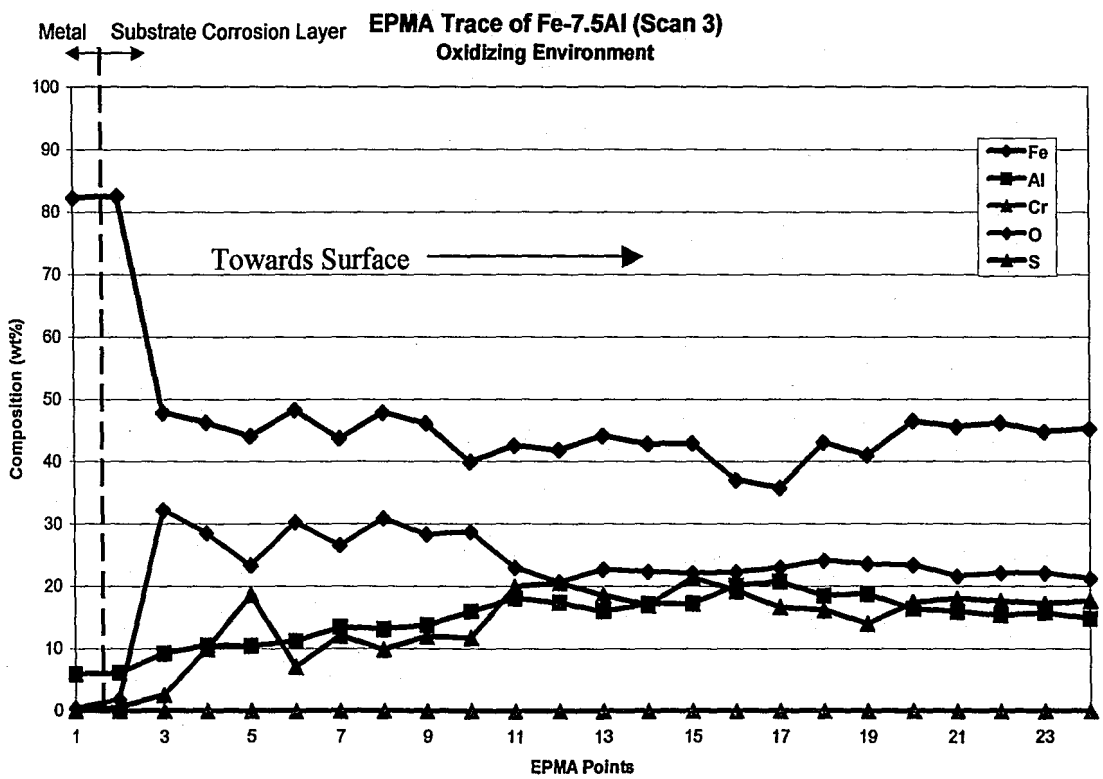

(b)

Figure 48 – EPMA trace (Scan 3) across the internal scale for Fe-7.5Al exposed to the oxidizing environment while in contact with the FeS_2 powder.

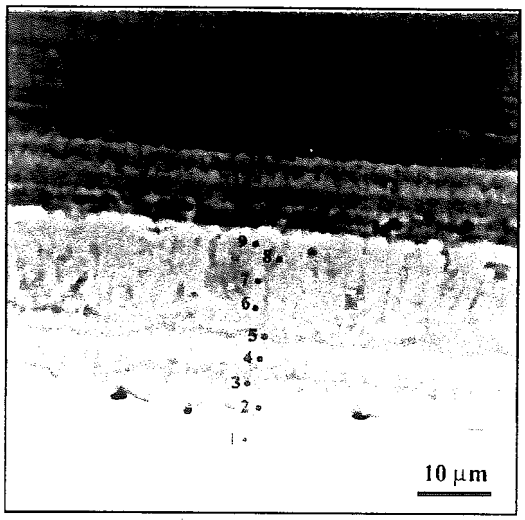

(a)

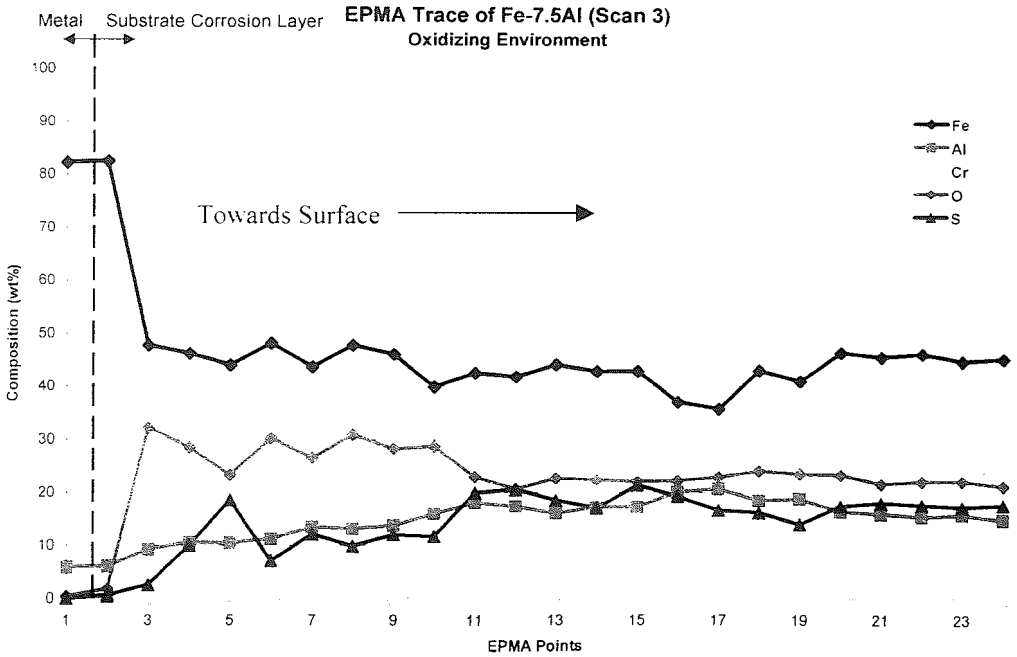

(b)

Figure 48 – EPMA trace (Scan 3) across the internal scale for Fe-7.5Al exposed to the oxidizing environment while in contact with the FeS_2 powder.

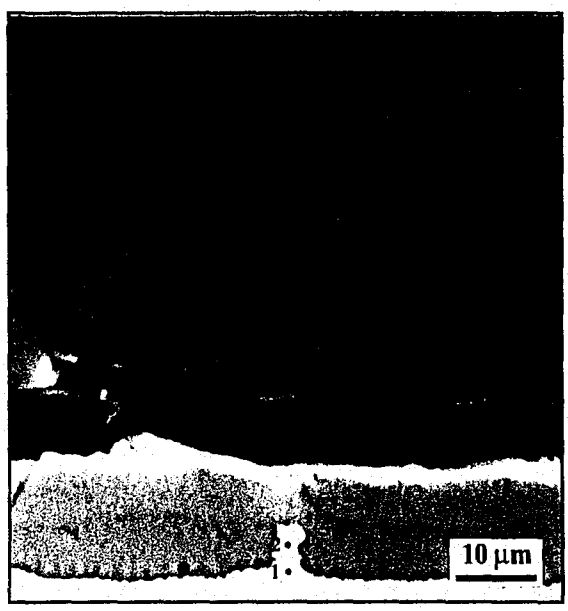

(a)

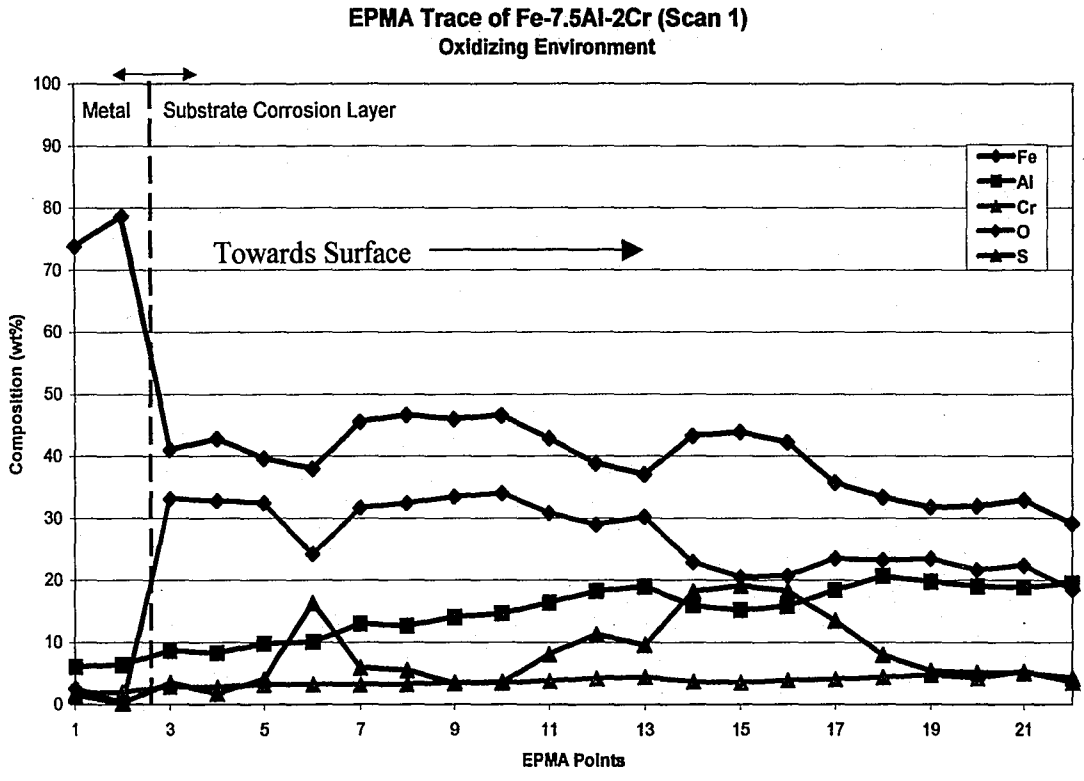

(b)

Figure 49 – EPMA trace (Scan 1) across the internal scale for Fe-7.5Al-2Cr exposed to the oxidizing environment while in contact with the FeS_2 powder.

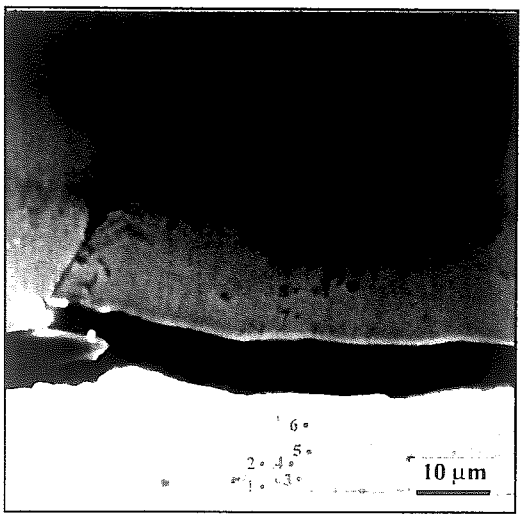

(a)

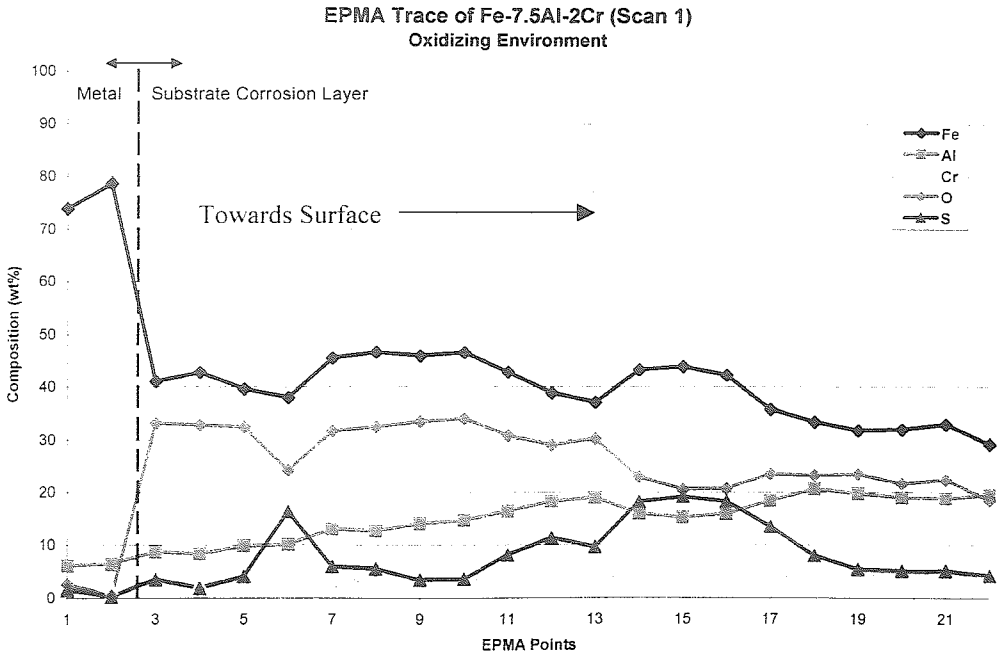

(b)

Figure 49 – EPMA trace (Scan 1) across the internal scale for Fe-7.5Al-2Cr exposed to the oxidizing environment while in contact with the FeS_2 powder.

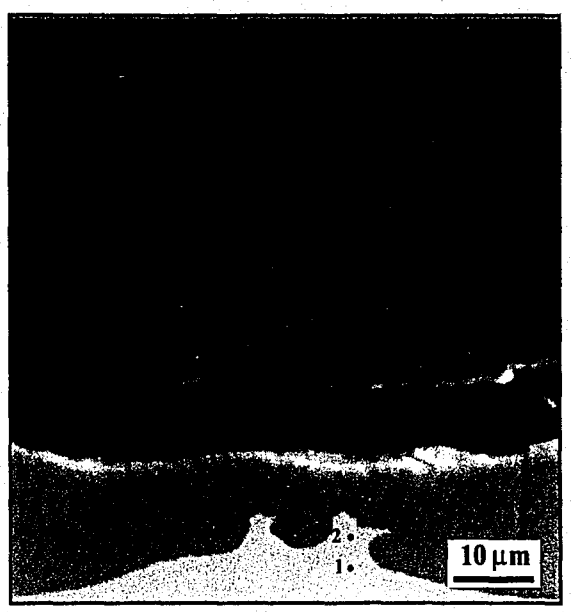

(a)

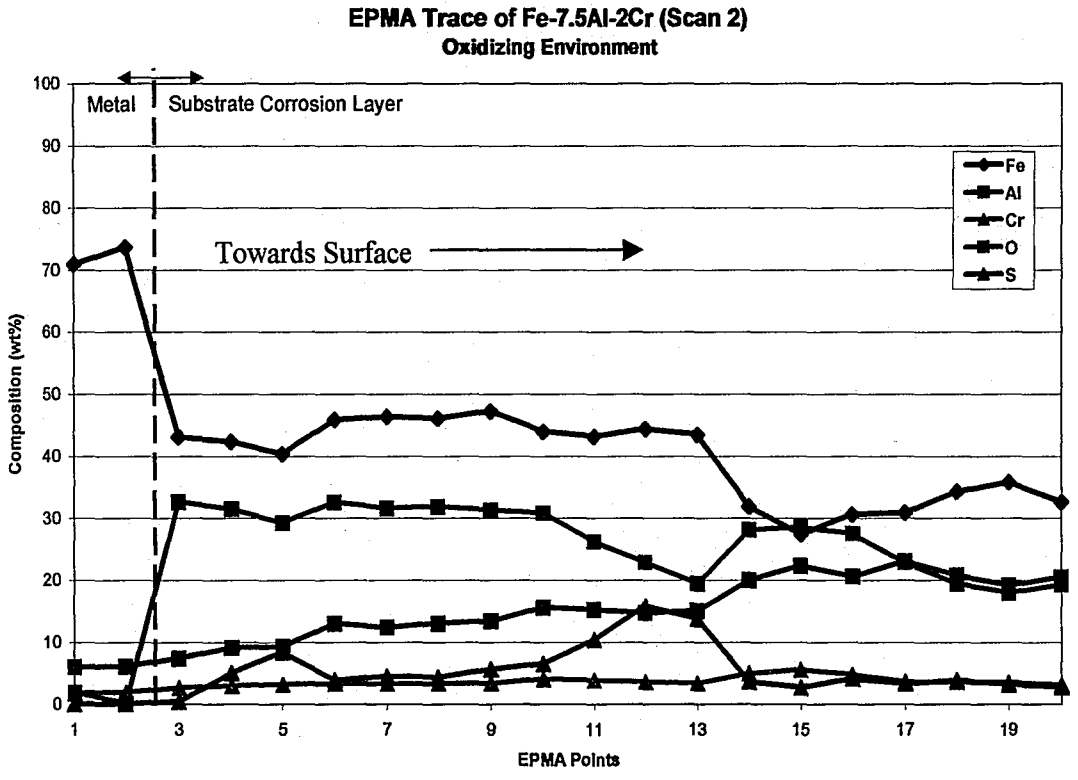

(b)

Figure 50 – EPMA trace (Scan 2) across the internal scale for Fe-7.5Al-2Cr exposed to the oxidizing environment while in contact with the FeS_2 powder.

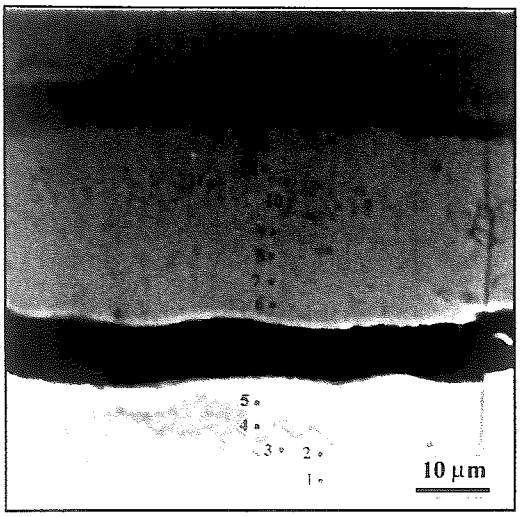

(a)

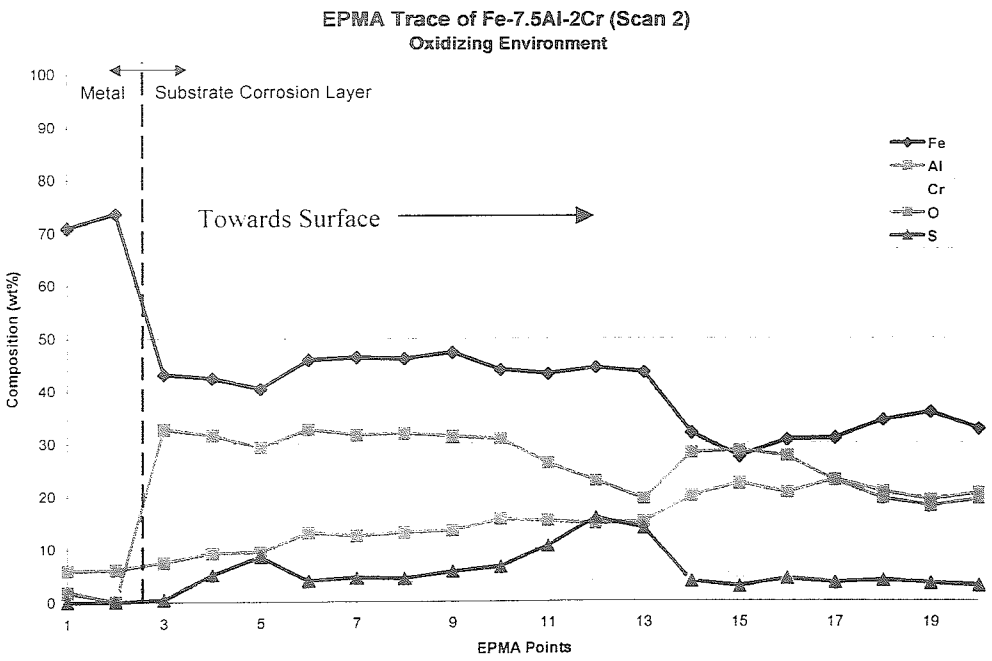

(b)

Figure 50 – EPMA trace (Scan 2) across the internal scale for Fe-7.5Al-2Cr exposed to the oxidizing environment while in contact with the FeS_2 powder.

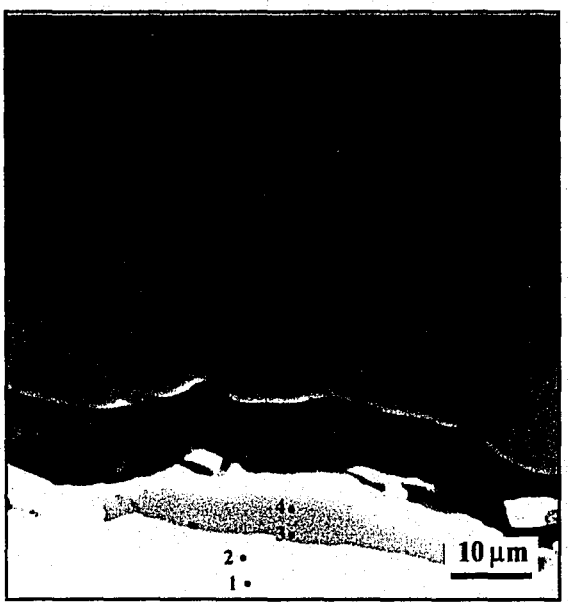

(a)

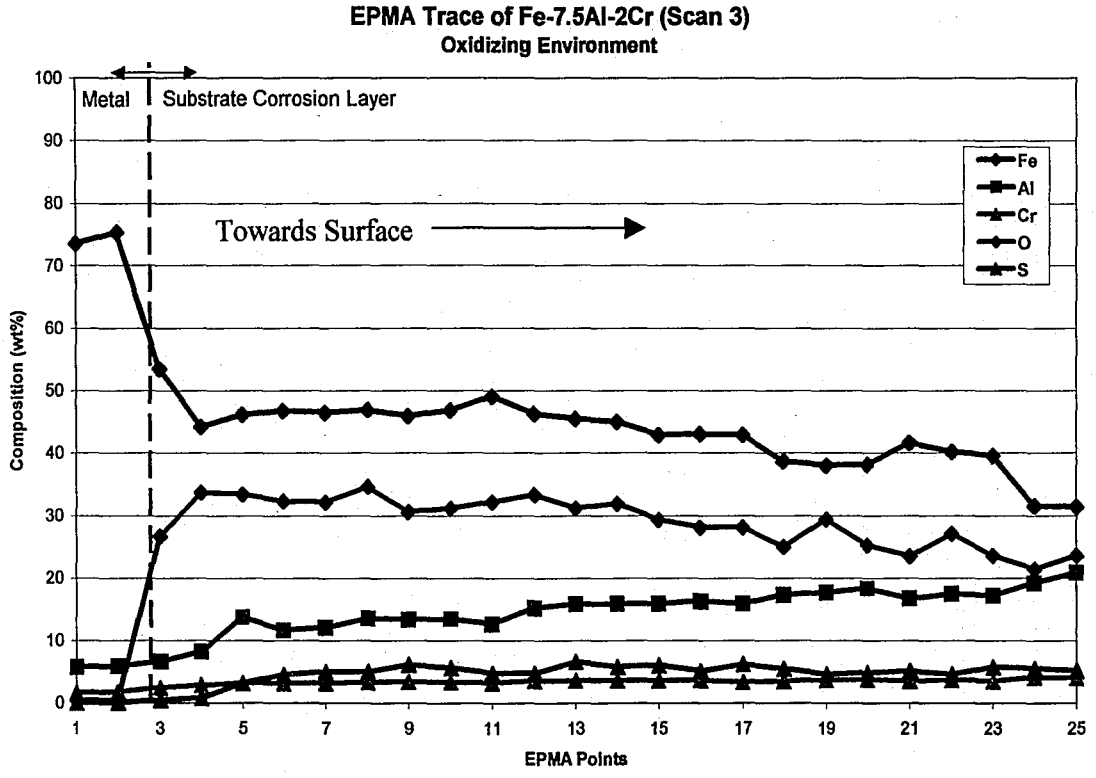

(b)

Figure 51 – EPMA trace (Scan 3) across the internal scale for Fe-7.5Al-2Cr exposed to the oxidizing environment while in contact with the FeS_2 powder.

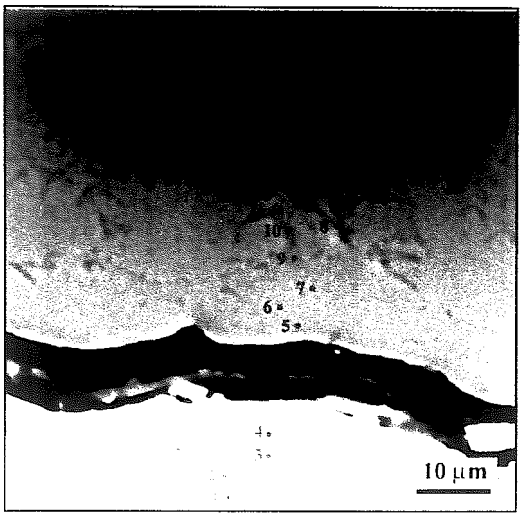

(a)

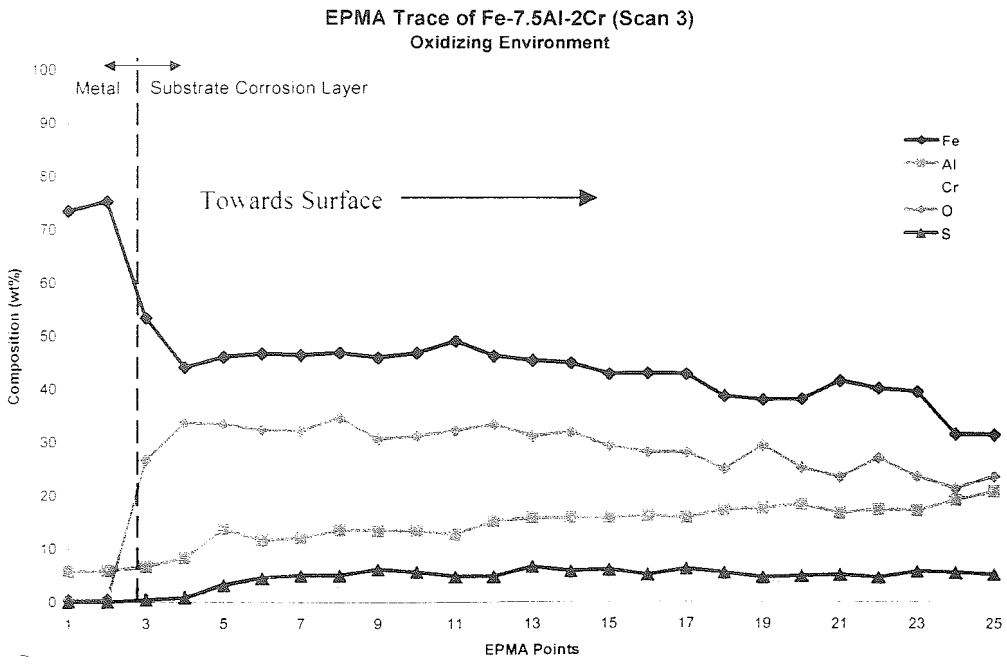

(b)

Figure 51 – EPMA trace (Scan 3) across the internal scale for Fe-7.5Al-2Cr exposed to the oxidizing environment while in contact with the FeS_2 powder.

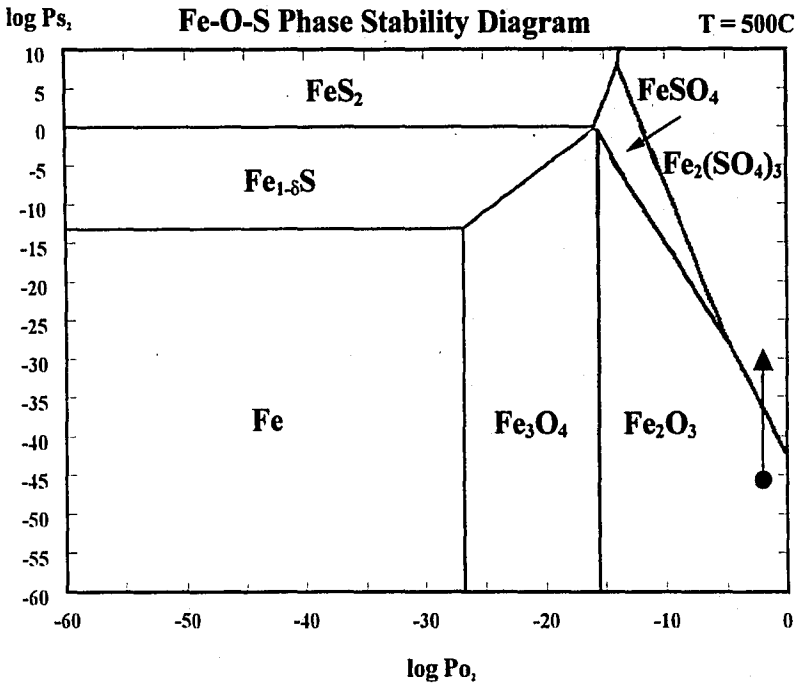

(a)

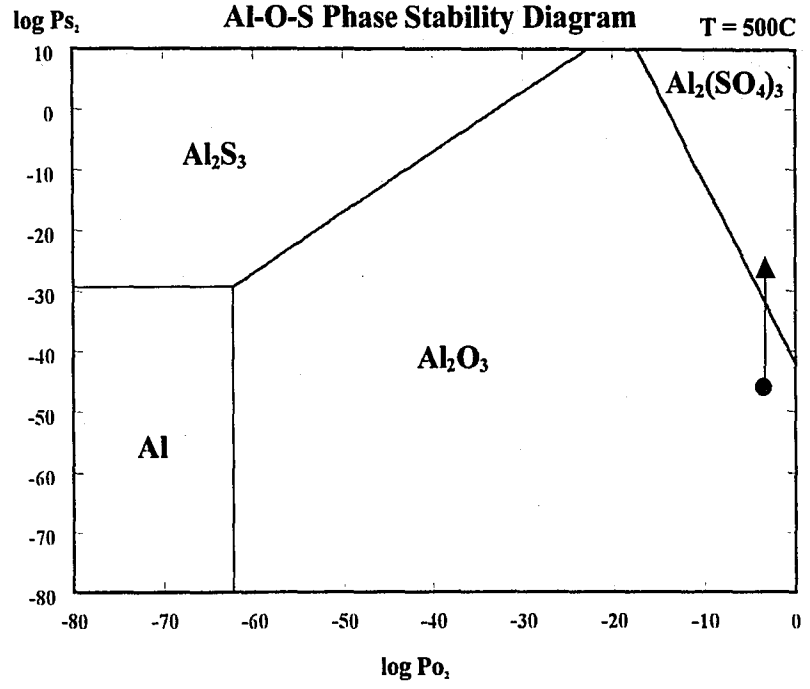

(b)

Figure 52 – Fe-O-S Phase Stability Diagram (a) and Al-O-S Phase Stability Diagram (b). The red point indicates where the oxidizing environment lies in each diagram.

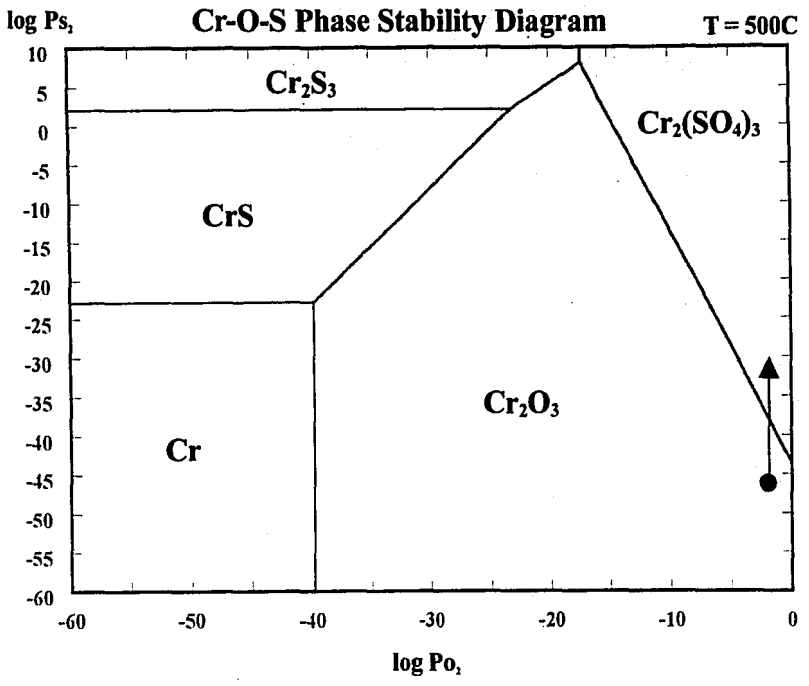

Figure 53 – Cr-O-S Phase Stability Diagram. The red point indicates the appropriate oxygen and sulfur partial pressures for the oxidizing environment.

3.4 Conclusions

Ten iron-aluminum based alloys were exposed to two corrosive environments while in contact with FeS_2 powder at 500°C for 100 hours. It was found that:

- In the mixed oxidizing/sulfidizing environment alloys containing aluminum concentrations of only 7.5wt% were not protective regardless of chromium and titanium additions. These alloys all formed an internal corrosion layer, which were approximately 20-30μm thick, along with significant external corrosion layers. On the other hand, alloys containing 10wt%Al performed well in the mixed oxidizing/sulfidizing environment, as they formed no significant corrosion products.

- In the oxidizing environment it was found that alloys containing 7.5wt%Al were again not protective and formed both internal and external growing corrosion products. The substrate corrosion layer showed cracks that protruded into the base metal as well. Additions of 5wt%Cr helped to reduce the amount of corrosion that occurred during 100 hours of exposure. Again, increasing the aluminum concentration to 10wt% improved the corrosion resistance dramatically. Additions of 1wt%Cr actually had a detrimental effect on the corrosion resistance of these alloys in the oxidizing environment, but increasing the chromium concentration to 2wt% provided protection during 100 hours of exposure.
- EPMA results on samples exposed to the oxidizing environment showed that the substrate corrosion scale that formed on gas-slag-metal samples consisted of various layers that varied slightly in composition. Phase stability diagrams were used to identify the most probable corrosion products present in the substrate corrosion layer. A region adjacent to the substrate corrosion scale was slightly depleted in aluminum and these levels increased within the scale towards the surface of the alloy. This indicated that the alloying elements diffused outward from the sample to form both external and substrate corrosion scales.

4. Chapter 4: Thermal Spray Coatings

"Corrosion Behavior of Fe-Al Based HVOF Thermal Spray Coatings"

4.1 Introduction

In order to prevent the corrosion of waterwall boiler tubes in fossil-fueled power plants, Fe-Al based alloys are being considered for coatings to be deposited on the boiler tubes. Two main types of coatings that are being considered are weld overlay claddings and thermal spray coatings. Weld overlay claddings have an advantage to thermal spray coatings as they provide a good metallurgical bond between the coating and the substrate. Unfortunately, Fe-Al based alloys with aluminum concentrations greater than 10wt%Al are susceptible to hydrogen cracking[7,95]. It has been shown previously that the high temperature corrosion lifetime of a coating is directly related to the aluminum content of the alloy[55]. Therefore, desired high aluminum content Fe-Al based coatings have yet to be successfully deposited using weld claddings. On the other hand, the main advantage of thermal spray coatings is that higher aluminum concentrations can be achieved within the coating.

It has been shown that traditionally used Arc Plasma Sprayed (APS) thermal spray coatings have high amounts of porosity and aluminum depleted regions due to the degradation of the Fe-Al based powder during application[9]. The porosity within the coating can be detrimental to the protection of the coating because corrosive gases may be able to permeate through the coating and attack the underlying substrate. A relatively new technique, known as High-Velocity Oxy-Fuel (HVOF) process, has been shown to deposit coatings with relatively low porosity and oxide inclusions[9]. Lowering the amount of porosity and oxide inclusions within the coating could potentially prevent the corrosive gas from penetrating to the substrate and attacking beneath the coating. It has previously been shown that the corrosion resistance of Fe-Al based HVOF is superior to that of Fe-Al based APS coatings[9]. In order to determine how the high temperature

corrosion behavior of HVOF thermal sprays compare to weld overlay claddings, multiple coating samples were exposed to two corrosive gaseous environments both with and without FeS_2 slag in contact with the coating.

4.2 Experimental Procedure

Iron-aluminum powder used to produce thermal spray coatings with lower aluminum concentration (Powder 16), commercially known as FAS, was provided by AMETEK. The powder used for the coatings was classified as having a US Standard Mesh Size of –270, which meant that the largest particles were less than 50μm in diameter. Oak Ridge National Laboratory (ORNL) provided iron-aluminum powder used to produce the thermal spray coatings with higher aluminum concentration (Powder 21). The chemical compositions of the powders were found using wet chemical analysis and can be seen in Table 6. The powder was sent to Idaho National Engineering and Environmental Laboratory (INEEL) where it was sifted once again and sprayed. Thermal sprays were applied to a low carbon steel substrate using a High-Velocity Oxy-Fuel (HVOF) process. Once received, the thermal spray coatings were sectioned using a high-speed diamond saw. Sprayed coating compositions were obtained using a JEOL 733 Microprobe, and a phi(ρz) correction scheme was used to correct for absorption and fluorescence that occurred during EPMA. EPMA gathered for the coating compositions was carried out over 10-15 points located randomly across the entire length of the thermal spray coatings. Sections of the coating coupons were mounted in cold setting epoxy and polished to 1μm for observation on the Light Optical Microscope. Coating thickness and oxide/porosity area fraction measurements were carried out using a Light Optical Microscope interfaced with a LECO digital imaging program.

Gaseous and gas-slag-metal corrosion experiments were carried out in a Lindberg/Blue Horizontal Tube Furnace. Samples used for the gas-slag-metal corrosion experiments were cleaned in acetone before a quartz ring was glued onto the coating surface. The quartz tube was

filled with a predetermined amount (1680mg) of FeS_2 powder. A schematic diagram of the gas-slag-coating experiments can be seen in Figure 54. The powder was weighed to the nearest tenth of a milligram using a digital balance. Both the gas-slag-coating sample and the gaseous sample were simultaneously tested at 500°C for 100 hours exposed to either the mixed oxidizing/sulfidizing gas or the oxidizing gas. The gas compositions can be seen back in Table 3 (p. 71). The sulfur and oxygen partial pressures were calculated using the HSC Chemistry program[39]. A gas-slag-metal sample and a gaseous sample were exposed in the mixed oxidizing/sulfidizing gas at 500°C for 450 hours as well. The samples were then mounted in cold setting epoxy and observed on the Light Optical Microscope. Images were taken using a camera integrated onto a Light Optical Microscope.

Table 6 – Iron-aluminum powder composition used to produce lower aluminum HVOF coatings (wt%).

Elements	Powder 16 (FAS)	Powder 21
Fe	80.25	77.09
Al	16.10	21.67
Cr	2.58	0.04
O	0.056	0.023
S	0.011	0.006
C	0.064	0.058

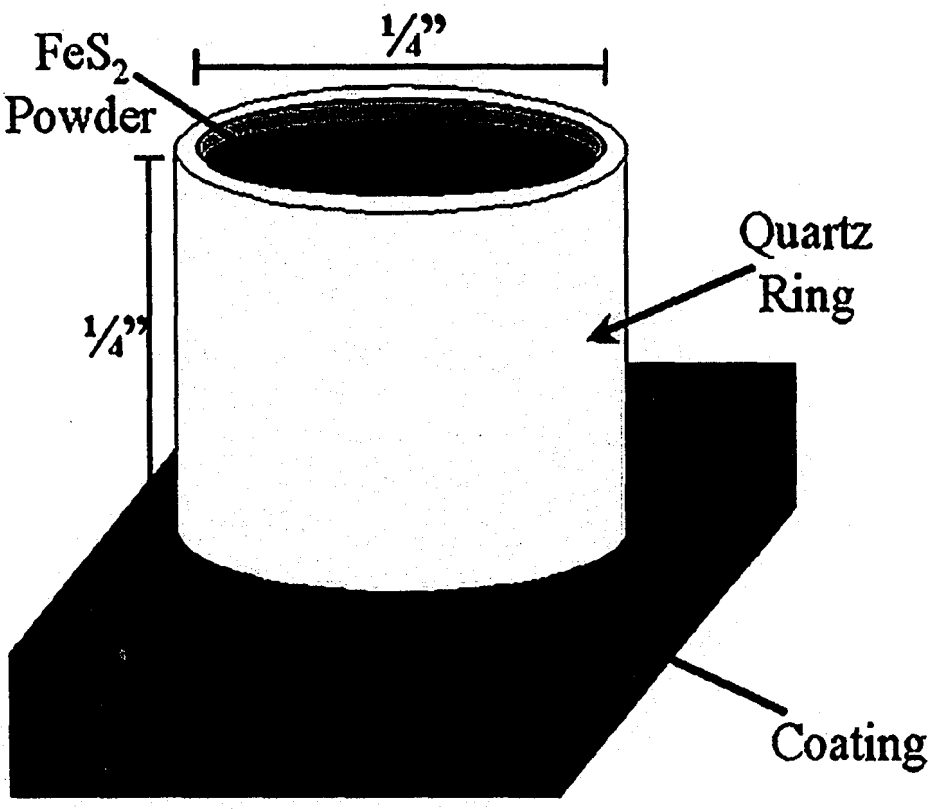

Figure 54 – Schematic diagram of the gas-slag-coating experimental setup.

4.3 Results and Discussion

4.3.1 Initial Characterization

Six HVOF thermal spray coatings made with Powder 16 and four HVOF coatings made with Powder 21 were received from INEEL. The thermal spray coupons were approximately 15mm wide by 7cm long. Quantitative chemical analysis of selected coatings was obtained by EPMA and can be seen in Table 7. Polished cross sections observed on the LOM revealed that all the coatings contained little porosity or oxides and that the coating thickness for all of the samples were on the order of several hundred microns. The maximum thickness of the coatings was located at the center of the thermal spray coupon and the thickness tapered off to minimum values at the edges of the coupon. Thickness measurements were therefore taken both at the

center of the coating and at the edges as well. Edge measurements were taken from approximately 2mm from the edge inward while center measurements were taken from approximately 2mm on each side of the maximum thickness of the coating. Oxides and porosity observed in the coatings were difficult to differentiate between using the LOM, therefore area fraction measurements were taken of the combined oxide/porosity contained in the coatings. The coating thickness measurements and the oxide/porosity contents can be seen in Table 8. The letter designation for the thermal sprays indicates that separate spray runs were made for each powder, but with identical processing parameters. Typical micrographs of the thermal sprays made with Powder 16 and Powder 21 can be seen in Figure 55. It can be seen from the thickness results that the coatings ranged from less than 150μm to over 400μm thick. Overall, the HVOF16 series coatings were slightly thicker than the HVOF21 series coatings, but the lower aluminum content coatings (HVOF16) contained significantly more oxides/porosity than the higher aluminum content coatings (HVOF21).

Table 7 – Chemical compositions of coatings selected for corrosion testing obtained by EPMA.

Elements	HVOF16A	HVOF21A
Fe	82.7 ± 0.37	78.3 ± 1.3
Al	15.6 ± 0.20	21.4 ± 0.74
Cr	2.1 ± 0.08	0.04 ± 0.03
O	0.10 ± 0.14	0.31 ± 0.44
S	0.01 ± 0.01	0.01 ± 0.01

Table 8 – Coating thickness and oxide/porosity area fraction measurements.

Coating Designation	Center Thickness (μm)	Edge Thickness (μm)	Oxide/Porosity Area Fraction (%)
Lower Aluminum Content Coatings (Powder 16)			
HVOF16A	294	181	14
HVOF16B	262	161	16
HVOF16C	340	255	17
HVOF16D	385	223	12
HVOF16E	408	266	10
HVOF16F	319	249	15
Higher Aluminum Content Coatings (Powder 21)			
HVOF21A	291	180	4
HVOF21B	252	178	5
HVOF21C	318	201	2
HVOF21D	215	139	5

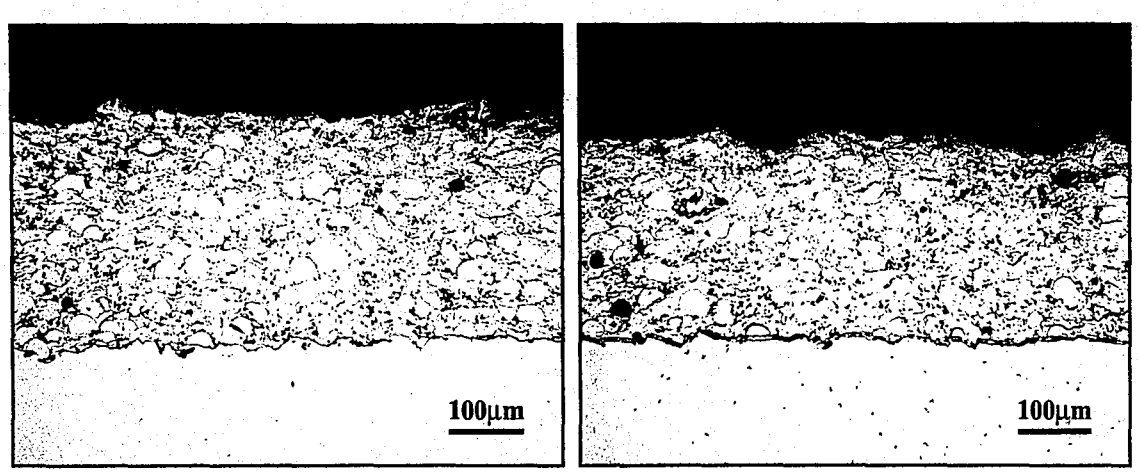

HVOF16A HVOF21A

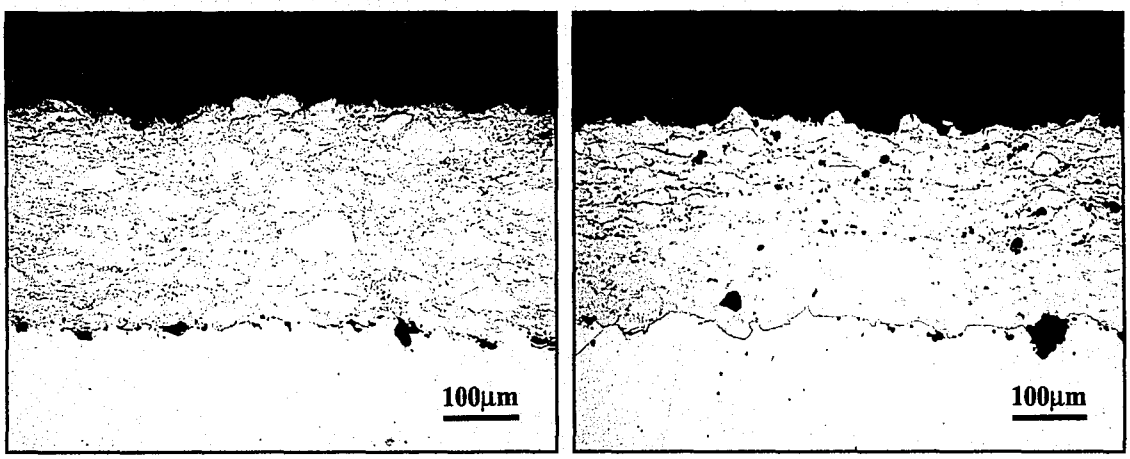

HVOF16B HVOF21B

Figure 55 – As received HVOF thermal spray coatings representative of coatings tested.

4.3.2 Gaseous Corrosion Testing

Two thermal spray samples were selected from each class of coatings. Coating HVOF16A and coating HVOF21A were selected for gaseous corrosion testing in the mixed oxidizing/sulfidizing and oxidizing environments at 500°C for 100 hours. Coating HVOF16B and HVOF21B were selected for gaseous corrosion testing in the mixed oxidizing/sulfidizing environment only for 450 hours. Different samples were used from each group of thermal sprays because there was not enough coating on one sample to perform all corrosion tests. Polished

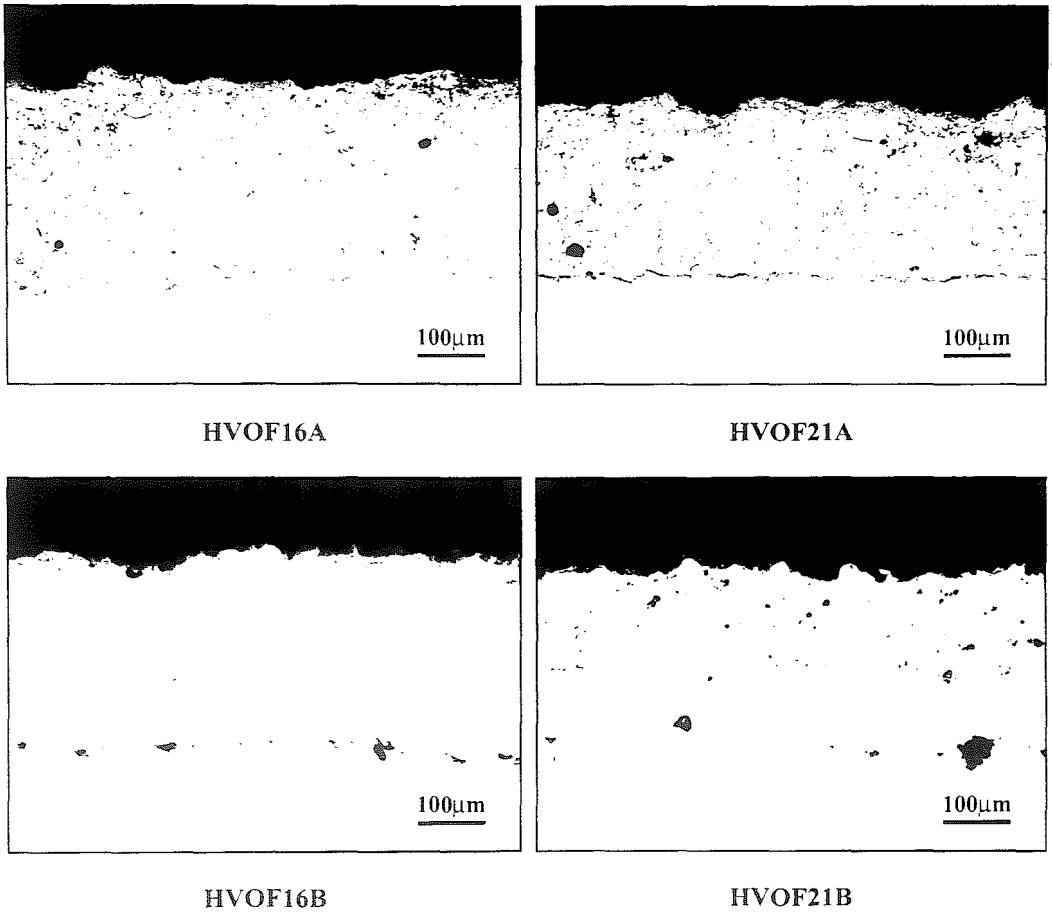

Figure 55 – As received HVOF thermal spray coatings representative of coatings tested.

4.3.2 Gaseous Corrosion Testing

Two thermal spray samples were selected from each class of coatings. Coating HVOF16A and coating HVOF21A were selected for gaseous corrosion testing in the mixed oxidizing/sulfidizing and oxidizing environments at 500°C for 100 hours. Coating HVOF16B and HVOF21B were selected for gaseous corrosion testing in the mixed oxidizing/sulfidizing environment only for 450 hours. Different samples were used from each group of thermal sprays because there was not enough coating on one sample to perform all corrosion tests. Polished

cross sections of HVOF16A and HVOF21A exposed to the mixed oxidizing/sulfidizing environment for 100 hours can be seen in Figure 56. It can be seen from this figure that very little attack of the coatings actually occurred, but it appeared that some corrosion products formed in the HVOF16A sample at the coating/substrate interface. This was verified using Energy Dispersive Spectroscopy (EDS), which indicated that sulfur and oxygen were present at the interface after being exposed to the mixed oxidizing/sulfidizing environment (Figure 57). A crack was also present at the coating/substrate interface on the HVOF16A sample. It was then observed that the higher aluminum content coating (HVOF21A) had extensive cracking that ran parallel to the coating/substrate interface and around unmelted particles. No corrosion products were observed at the interface on the HVOF21A sample after 100 hours of exposure.

HVOF16B and HVOF21B exposed to the mixed oxidizing/sulfidizing environment for 450 hours had oxygen and sulfur rich corrosion products at the coating/substrate interface as well. Figure 58 shows these coatings exposed for longer times in the mixed oxidizing/sulfidizing environment. It can be seen from this figure that HVOF21B, which contained approximately 21wt%Al, showed extensive corrosion after 450 hours of exposure. Note that the coating can still be seen between the outward growing external scale and the internal growing scale. The 16wt%Al coating also lost considerable amount of coating thickness after being exposed to the mixed environment for 450 hours. Comparing HVOF16B as received (Figure 55) and after 450 hours of exposure in the mixed oxidizing/sulfidizing environment (Figure 58) it can be seen that over half of the original coating thickness was lost. Relatively small amounts of corrosion products could be seen on the HVOF16B sample at the coating/substrate interface as well.

The significant amount of coating loss that was observed on the HVOF16B and HVOF21B samples exposed to the mixed oxidizing/sulfidizing environment for 450 hours may have occurred due to two possible events. First, relatively small amounts of corrosion product can be seen on HVOF16B both at the coating/substrate interface and on the coating surface, while

large amounts of corrosion can be seen on HVOF21B. One possible reason for the coating loss may be that the coating was not protective for long times in the mixed oxidizing/sulfidizing environment and the top of the coating was attacked and broke away due to thermal and growth stresses within the corrosion scale. Another possible explanation may be that the cracks that run parallel to the coating/substrate interface seen on some samples, such as HVOF21A exposed to the mixed oxidizing/sulfidizing environment for 100 hours, were also present on the HVOF16B and HVOF21B samples after 450 hours of exposure. These cracks could have lead to a coating loss if the coating was under enough stress for the top portion to break away from the rest of the coating. These cracks could also act as fast diffusion paths for corrosive gases to attack the underlying coating or substrate if the cracks were exposed to the atmosphere. Despite the mechanism behind the coating losses, it can be seen that the HVOF thermal spray coatings are not protective at longer times when exposed to the mixed oxidizing/sulfidizing environment.

Similar results were found for HVOF16A and HVOF21A exposed to the oxidizing gas for 100 hours. Polished cross sections of these coatings, seen in Figure 59, revealed that relatively no corrosion took place within the 21wt%Al coating and no corrosion products could be observed at the coating/substrate interface. Again, cracks running parallel to the coating/substrate interface could be seen in the HVOF21A sample after exposure to the oxidizing environment for 100 hours. For the 16wt%Al coating, significant coating thickness loss occurred similar to the mixed oxidizing/sulfidizing environment at longer times. No corrosion products were observed either within the HVOF16A coating or at the coating/substrate interface. Again coating loss may have been either due to the formation of cracks parallel to the coating/substrate interface or from corrosion products forming within the coating and the top portion of the coating breaking away due to thermal or scale growth stresses.

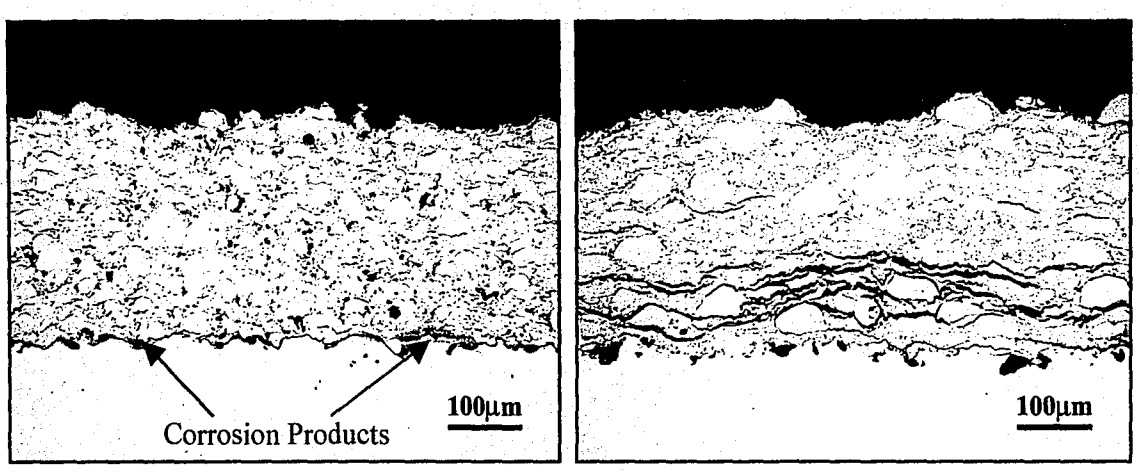

(a) (b)

Figure 56 – HVOF16A (a) and HVOF21A (b) exposed to the mixed oxidizing/sulfidizing environment at 500°C for 100 hours. Note the corrosion product that can be seen on HVOF16A at the coating/substrate interface and the large cracks that run along the HVOF21A coating.

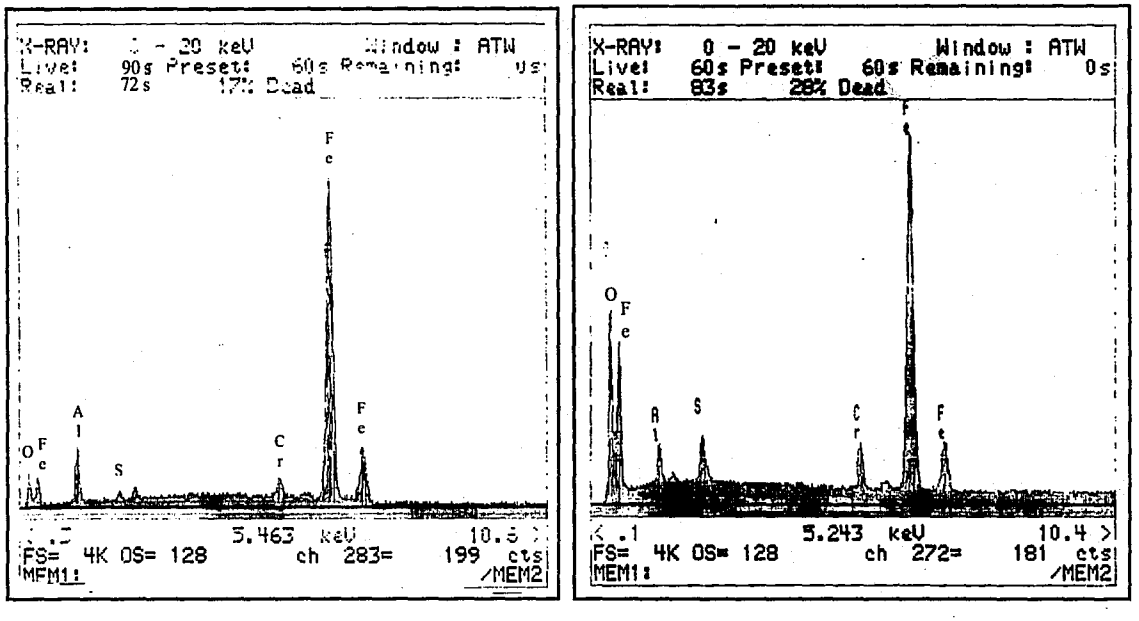

(a) (b)

Figure 57 – EDS of the corrosion products found at the coating/substrate interface on the HVOF16A coating exposed to the mixed oxidizing/sulfidizing environment (a) and the HVOF16A coating exposed to the oxidizing environment while in contact with FeS_2 (b) for 100 hours. Note that oxygen and sulfur were both present at the coating/substrate interfaces.

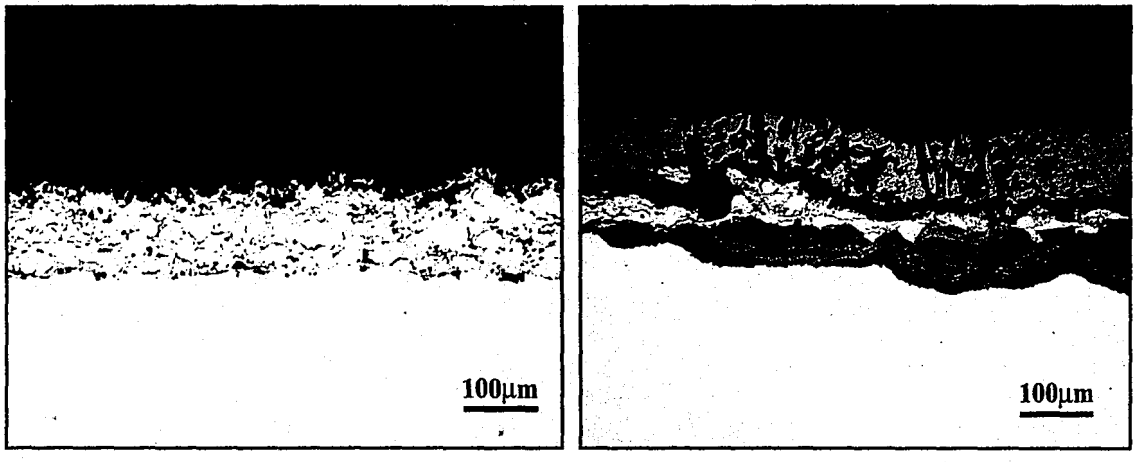

(a) (b)

Figure 58 – HVOF16B (a) and HVOF21B (b) exposed to the mixed oxidizing/sulfidizing environment at 500°C for 450 hours.

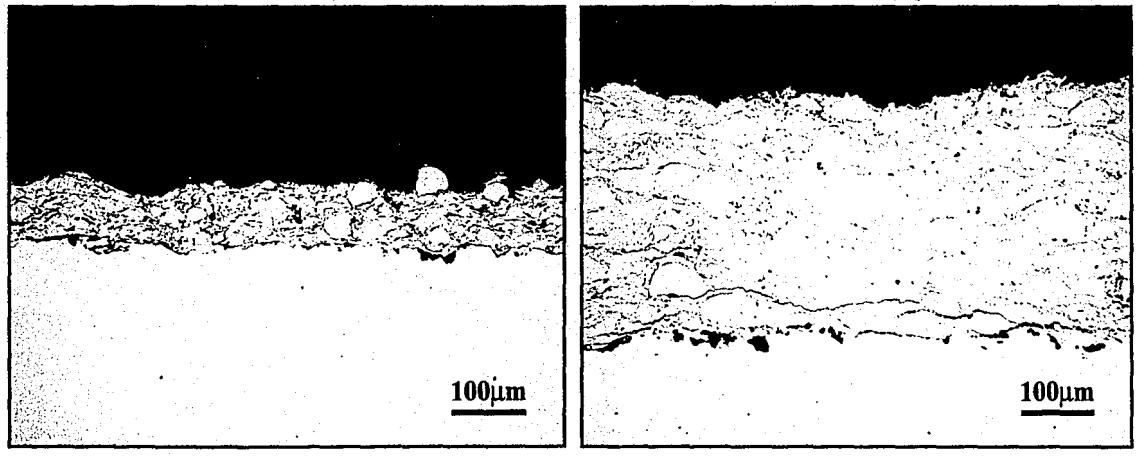

(a) (b)

Figure 59 – HVOF16A (a) and HVOF21A (b) exposed to the oxidizing gas for 100 hours.

4.3.3 Gas-Slag-Coating Corrosion Testing

Coatings HVOF16A and HVOF21A were exposed to the mixed oxidizing/sulfidizing gas and the oxidizing gas while in contact with FeS_2 powder at 500°C for 100 hours. Polished cross sections of these samples can be seen in Figure 60. It can be seen that these coating exposed during the gas-slag-metal corrosion test behaved similarly to when they were exposed to the gas only. Cracks were observed in all the HVOF16A and HVOF21A coatings exposed to both the mixed oxidizing/sulfidizing environment and the oxidizing environment while in contact with FeS_2. These cracks ran parallel or along the coating/substrate interface. Corrosion products could not be detected within the coatings, but they were found along the coating/substrate interface on HVOF16A after exposure to the oxidizing environment while in contact with FeS_2. The corrosion products observed at the coating/substrate interface on the HVOF16A coating exposed to the oxidizing environment while in contact with FeS_2 were rich in both oxygen and sulfur and can be seen in Figure 57.

It can be seen from these results that although the HVOF thermal spray coatings were relatively corrosion resistant at 500°C in the two environments up to 100 hours of exposure, extensive cracking could be seen running parallel to or along the coating/substrate interface in several samples, and in other samples it was also observed that the corrosive atmosphere was able to reach and attack the non-protective substrate. When looking at each individual coating, the HVOF16A coating (16wt%Al) formed corrosion products rich in oxygen and sulfur at the coating/substrate interface after 100 hours of exposure to the mixed oxidizing/sulfidizing environment. The coating with an equivalent composition (HVOF16B) demonstrated significant coating thickness loss after 450 hours of exposure in this mixed atmosphere. After 100 hours of exposure to the oxidizing environment, HVOF16A demonstrated a significant coating thickness loss as well. The addition of FeS_2 powder to the mixed oxidizing/sulfidizing atmosphere and the oxidizing environment resulted in cracks along the coating/substrate interface for HVOF16A

coatings. HVOF16A also formed small corrosion products rich in oxygen and sulfur after being exposed to the oxidizing environment (with FeS_2) for 100 hours.

The HVOF21A coating (21wt%Al) formed cracks that ran parallel to the coating/substrate interface after 100 hours of exposure to the mixed oxidizing/sulfidizing environment. After 450 hours of exposure in the same mixed environment, significant corrosion took place of both the coating (HVOF21B) and the substrate and a large amount of the coating thickness was lost. In the oxidizing environment, HVOF21A did not form any corrosion products but cracking of the coating was observed again after 100 hours of exposure. Placing FeS_2 in contact with the HVOF21A coatings did not change the corrosion behavior of this coating in either the mixed oxidizing/sulfidizing environment or the oxidizing atmosphere. Again, cracks running parallel to the coating/substrate interface were observed in the HVOF21A coatings exposed to both types of environments containing FeS_2. A summary of the corrosion behavior for these HVOF thermal spray coatings can be seen in Table 9. These results seem to indicate that although the HVOF thermal spray coatings are a higher quality coating than the traditional APS thermal spray coatings, the HVOF thermal spray coatings are not acceptable as corrosion resistant coatings in these types of environments because they either form corrosion products at the coating/substrate interface or significant cracking of the coating is observed.

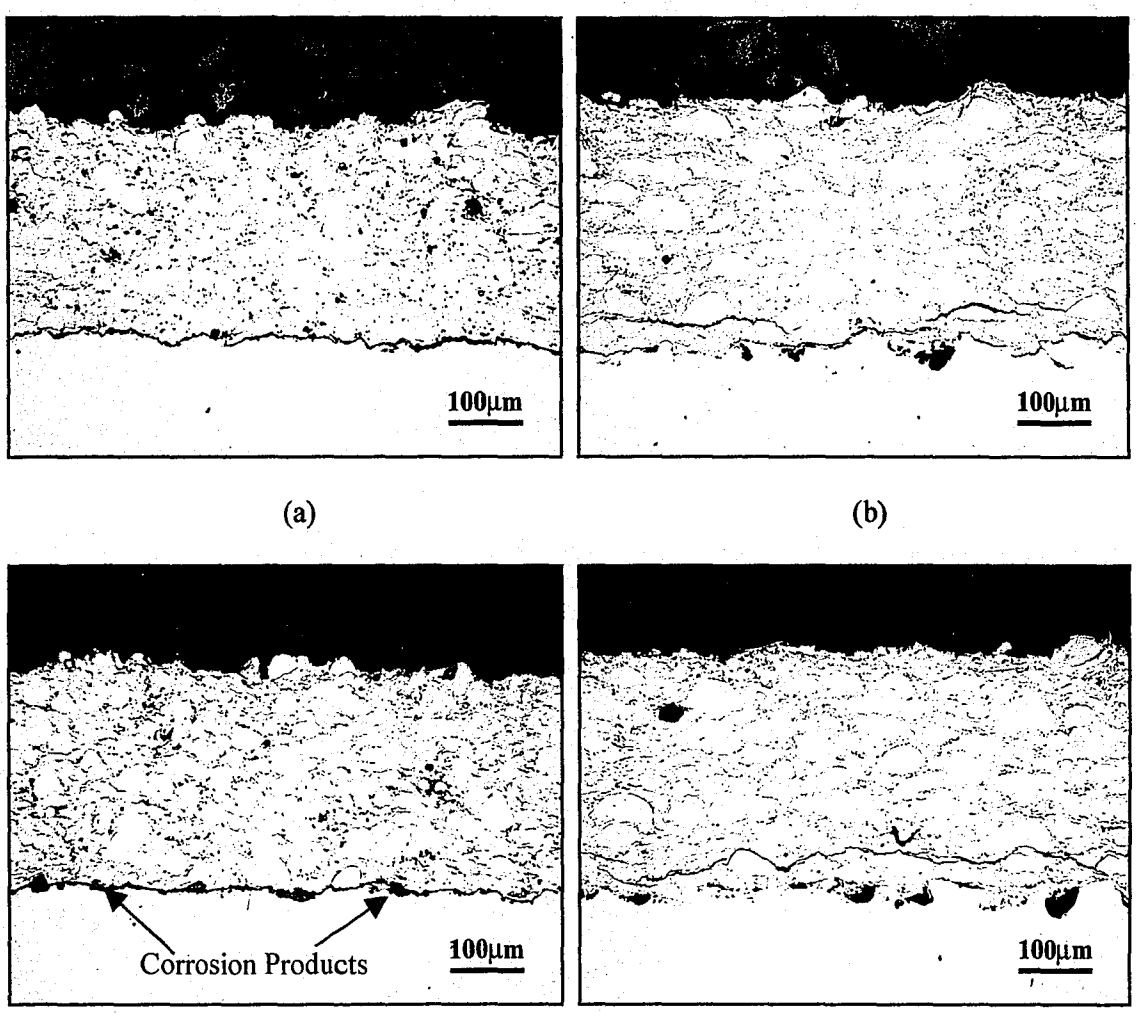

Figure 60 – HVOF16A exposed for 100 hours at 500°C in the mixed oxidizing/sulfidizing environment (a) and the oxidizing environment (c) combined with HVOF21A exposed to the mixed oxidizing/sulfidizing atmosphere (b) and the oxidizing atmosphere (d).

Table 9 – Summary of HVOF coating corrosion behavior in each environment. Corrosion indicates that corrosion products were observed either on the surface of the coating or at the coating/substrate interface. Cracking indicates that cracks were observed either within the coating or at the coating/substrate interface.

HVOF Coating		Mixed O_2/S_2 Gas (100H)	Mixed O_2/S_2 Gas (450H)	Mixed O_2/S_2 Gas + FeS_2 (100H)	Oxidizing Gas (100H)	Oxidizing Gas + FeS_2 (100H)
HVOF16	Cracking	X	✓(LOSS)	✓	✓(LOSS)	✓
	Corrosion	✓	✓	X	X	✓
HVOF21	Cracking	✓	✓(LOSS)	✓	✓	✓
	Corrosion	X	✓	X	X	X

✓ - Cracking occurred only

✓(LOSS) – Cracking occurred with significant coating thickness loss

X – Cracking or corrosion did not occur

4.4 Conclusions

HVOF thermal spray coatings containing 16wt%Al or 21wt%Al were exposed to several corrosive environments at 500°C. It was found that:

- HVOF coatings having an aluminum concentration of 16wt%Al contained observable corrosion products, cracks along the coating/substrate interface, demonstrated a coating thickness loss, or had a combination of these when exposed to the corrosive environments for 100 hours.
- HVOF coatings containing 21wt%Al showed no indication of corrosive attack either within the coating or at the coating/substrate interface, but cracks were observed within the coating parallel to the coating/substrate interface after 100 hours of exposure in all of the corrosive environments.

- Coatings exposed to the mixed oxidizing/sulfidizing environment for longer times (450 hours) demonstrated significant coating thickness losses and corrosion products were observed on these samples as well.
- FeS_2 powder in contact with the coatings seemed to have no significant effect on their corrosion behavior.
- It was therefore concluded that although the HVOF thermal spray coatings have been shown to offer better corrosion protection than the traditional APS coatings, they cannot provide the corrosion protection needed for the application of boiler tube coatings.

5. Chapter 5: Critical Alloying Concentrations Needed for Corrosion Protection

5.1 Introduction

It has been shown in the previous chapters that there are several factors that determine the corrosion resistance of a coating. The reactive environment, the temperature of exposure, the type of coating, and coating composition are all important factors to consider when determining whether a coating is protective or not. In addition, the chemical composition required for a protective coating differed depending on the technique used to characterize the alloy. Results from Chapter 2 showed that several weld overlay compositions were protective in the three gaseous environments when considering the kinetics of corrosion because they showed no significant weight gains during 100 hours of exposure. This method of selecting protective coatings has been used a great deal in the past by many researchers in the field of high temperature corrosion[6,8,58,68,98-100]. Although this criterion is acceptable for ranking the corrosion resistance of different alloys, it was seen in Chapter 2 that corrosion kinetics cannot solely be used to describe if an alloy or coating is protective, but the corrosion morphology must be considered as well. Based on these observations, the combination of the corrosion kinetics and the resulting scale morphologies was used to determine whether a coating was protective in a gaseous environment. For gas-slag-coating exposures of weld overlays and thermal spray coatings, kinetic data was not available so microstructural observations were used to rank and characterize the coatings.

In two of the gaseous environments, the effect of water vapor on the high temperature corrosion resistance was explored as well. For many years, it has been well documented that water vapor additions to high temperature corrosion environments is detrimental to the alloy and results in higher corrosion rates and lower coating lifetimes[90,91]. Although this phenomenon has been observed many times, the mechanisms that cause the decrease in the corrosion resistance is

not well understood. The effect of water vapor in this study was considered to determine if the critical alloying compositions changed significantly between dry and wet environments, but the mechanisms behind the change in corrosion behavior with the addition of water vapor is currently being studied.

5.2 Experimental Procedure

Alloys used in this part of the study to simulate weld overlay compositions were cast as described in Chapter 2. The alloying compositions used in this part of the study can be seen in Table 10. Alloys with titanium additions were not included in this section of the study because there were mixed results on the effects of titanium additions on the corrosion behavior of ternary Fe-Al-Cr alloys. Corrosion experiments were carried out using a Netzsch STA 409 high-temperature thermogravimetric (TG) balance, which measures changes in weight over time. The sample preparation was described in the experimental procedure section of Chapter 2. The specimens were heated at a rate of 50°C/min and were held at 500°C for 100 hours. Water vapor present in the mixed oxidizing/sulfidizing and the oxidizing environments was injected into the furnace at a controlled rate. In order to compare the corrosion behavior of alloys in wet and dry environments, the mixed oxidizing/sulfidizing and the oxidizing environments were used, but no water was injected into these environments to obtain the dry conditions. All of the gases used in this part of the study can be seen in Table 11. The sulfur and oxygen partial pressures were calculated for the gases using the HSC Chemistry program[39]. A JEOL 6300 Scanning Electron Microscope (SEM) was used to obtain surface images. Samples were observed with a 17mm working distance and accelerating voltages of 5keV. SEM surface images were used with an imaging program to obtain area fractions. The gas-slag-metal experimental setup was described in detail in the experimental procedure section of Chapter 3. LOM images were taken with an integrated camera on a LECO digital imaging system. The internal corrosion scales observed in

non-protective alloys were measured using an imaging program interfaced with a Light Optical Microscope.

Table 10 – Approximate alloy compositions used for gaseous and gas-slag-metal corrosion testing (wt%).

Alloy Designation	Fe	Al	Cr
Fe-7.5Al	Bal.	7.5	--------
Fe-7.5Al-1Cr	Bal.	7.5	1.0
Fe-7.5Al-2Cr	Bal.	7.5	2.0
Fe-7.5Al-5Cr	Bal.	7.5	5.0
Fe-10Al	Bal.	10.0	--------
Fe-10Al-1Cr	Bal.	10.0	1.0
Fe-10Al-2Cr	Bal.	10.0	2.0
Fe-10Al-5Cr	Bal.	10.0	5.0

Table 11 – Wet and dry gas compositions used for gaseous corrosion testing (vol.%).

Gas Component	Sulfidizing Environment	Wet Mixed Oxidizing/ Sulfidizing Environment	Dry Mixed Oxidizing/ Sulfidizing Environment	Wet Oxidizing Environment	Dry Oxidizing Environment
O_2	--------	--------	--------	2	2
CO	15	10	10	--------	--------
CO_2	--------	5	5	15	15
H_2	3	--------	--------	--------	--------
H_2O	--------	2	--------	6	--------
H_2S	0.12	0.12	0.12	--------	--------
SO_2	--------	--------	--------	0.12	0.12
N_2	Bal.	Bal.	Bal.	Bal.	Bal.
Log Po_2	-28	-19	-20	-2	-4
Log Ps_2	-6	-8	-8	-46	-46

5.3 Results and Discussion

5.3.1 Gaseous Environments

Kinetic experiments were carried out for alloys exposed to the sulfidizing environment, the wet mixed oxidizing/sulfidizing environment, and the wet oxidizing environment. The specific kinetic results for these three environments are reported in Chapter 2. The total weight gains that occurred over 100 hours of exposure in each of these environments were used along with each alloy composition in an attempt to find the compositions required to prevent high corrosion rates. Regression analysis was performed on the alloy compositions to determine if

there were critical alloying concentrations needed to prevent large weight gains during 100 hours of exposure. The regression analysis results indicated that an alloying content factor could be obtained combining the aluminum and chromium compositions. The coefficient for the aluminum concentration was given as approximately 1, and the coefficient for the chromium concentration was reported to be approximately 0.5. This led to the alloying content factor of:

$$F = (wt\%Al) + 0.5(wt\%Cr) \quad (17)$$

The alloying content factor for each alloy used in this part of the study can be seen in Table 12. The alloying content factor for each alloy was plotted against total weight gains after 100 hours of exposure to the sulfidizing, the wet mixed oxidizing/sulfidizing, and the wet oxidizing environments and can be seen in Figure 61. From this figure it can be seen that below the alloying content factor of 10 significant weight gains were observed, but above 10 no weight gains were observed in all three gasses and alloys in this alloying range seemed protective. It was therefore concluded that according to the kinetic results alone there is a critical alloying content factor of 10 needed to prevent significant corrosion weight gains from occurring during 100 hours of exposure.

Table 12 – Alloying Content Factors for each alloy used in the study.

Alloy Designation	F = (wt%Al) + 0.5(wt%Cr)
Fe-7.5Al	7.5
Fe-7.5Al-1Cr	8.0
Fe-7.5Al-2Cr	8.5
Fe-7.5Al-5Cr	10.0
Fe-10Al	10.0
Fe-10Al-1Cr	10.5
Fe-10Al-2Cr	11.0
Fe-10Al-5Cr	12.5

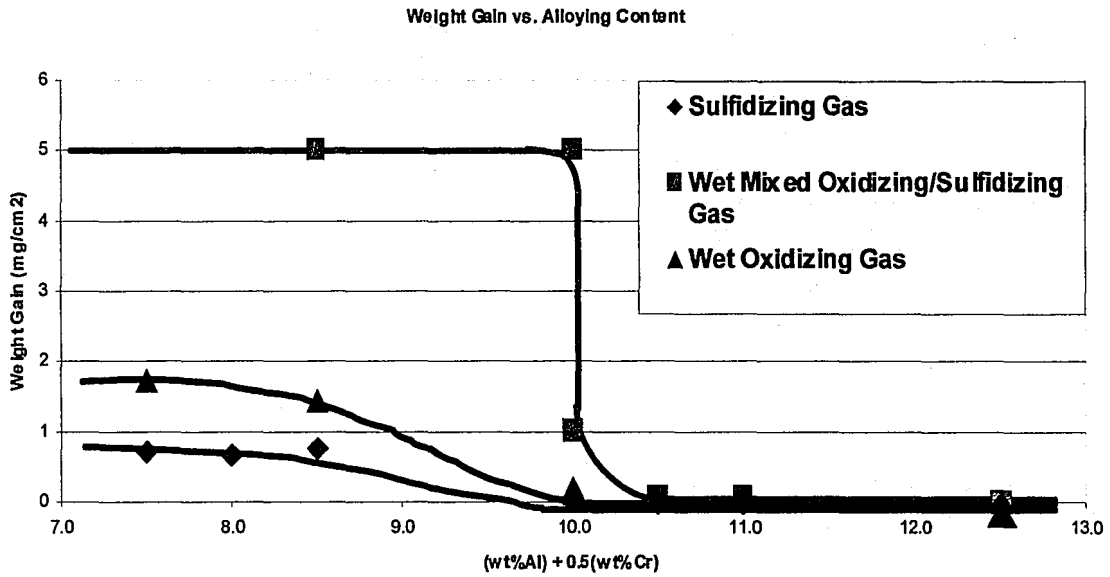

Figure 61 – Total weight gain after 100 hours of exposure plotted against the alloying content factors for each alloy.

Although this is a good indication as to what alloying compositions are required to prevent high weight gains in the three environments, it has been shown in Chapter 2 that kinetic data alone cannot be used to determine if an alloy is protective. The scale morphology was therefore considered as well to help determine alloying concentrations needed to obtain a protective coating. Figure 62 shows the nodule area fractions for alloys exposed to the sulfidizing, the wet mixed oxidizing/sulfidizing, and the wet oxidizing gases. This figure indicates that an alloying content factor of 10 was required to significantly decrease the amount of surface area covered by external nodule growth. Considering the wet mixed oxidizing/sulfidizing environment, it can be seen that there were still nodules present on the surface for the Fe-10Al-1Cr (F=10.5) and the Fe-10Al-2Cr (F=11.0) alloys, but nodules are no longer present on the Fe-10Al-5Cr alloy (F=12.5). It was therefore concluded that although the alloys demonstrated no weight gains and the amount of surface area covered by external nodules significantly decreases in all three of these environments above F=10, an alloying content factor of 12.5 is required to ensure that the coating maintains a passive layer and is protective through 100 hours of exposure in the sulfidizing, the wet mixed oxidizing/sulfidizing, and the wet oxidizing environments.

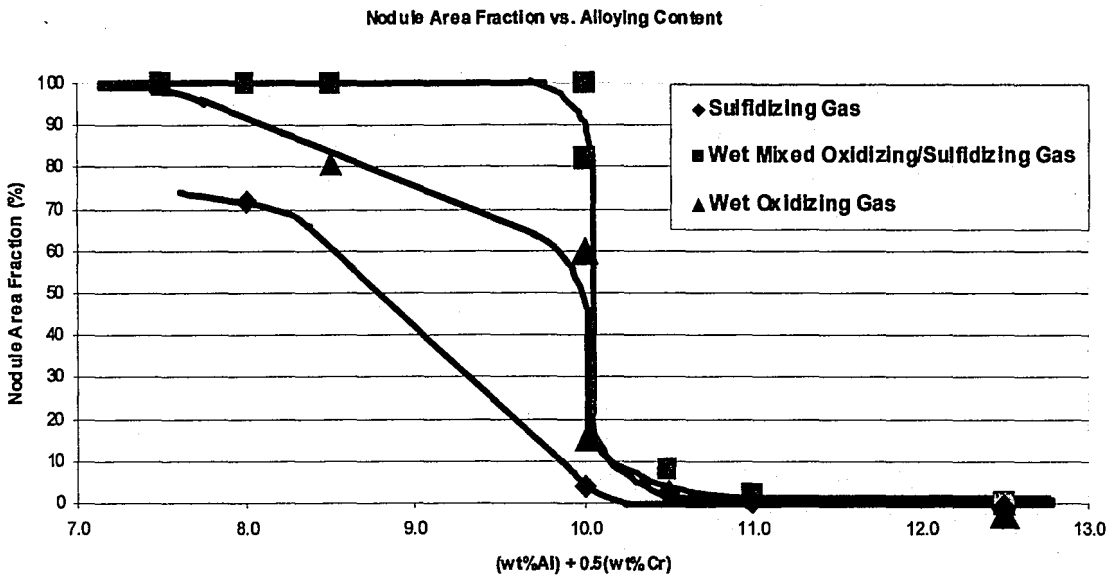

Figure 62 – Nodule area fraction plotted against the alloying content factors for each alloy.

5.3.2 Gas-Slag Environments

Several alloys were tested in gas-slag environments where the slag was simulated by placing FeS_2 powder in intimate contact with the alloy and exposing the setup to either the mixed oxidizing/sulfidizing environment (wet only) or the oxidizing atmosphere (also wet only). The experimental procedure for this setup can be seen in detail in Chapter 3. These samples were cross-sectioned and polished for light optical observations. Many of the samples contained substrate corrosion scales, which were measured. The substrate corrosion layer thickness for samples containing 7.5wt%Al and exposed to the mixed oxidizing/sulfidizing environment can be seen back in Table 4. Alloys containing 10wt%Al exposed to the mixed oxidizing/sulfidizing environment did not contain any measurable substrate corrosion layer. Substrate scale thickness measurements of samples containing 7.5wt%Al that were exposed to the oxidizing gas while in contact with the FeS_2 powder can be seen back in Table 5. Again, alloys containing 10wt%Al that were in contacts with the FeS_2 powder did not form any measurable substrate corrosion layer.

In order to further investigate the critical alloying contents required to obtain a protective weld overlay coating, the substrate corrosion scale thickness measurements were further explored to determine if the thickness had any alloying dependence. Therefore, the substrate scale thickness was plotted against the alloying content factors and can be seen in Figure 63. It can be seen from this figure that the substrate corrosion layer thickness decreases to zero above an alloying content factor of 10 (with the exception of Fe-10Al-1Cr, which showed a significant substrate corrosion layer after 100 hours of exposure to the oxidizing gas while in contact with the FeS_2 powder). These results are consistent with the gaseous corrosion testing results, which also showed that an alloying content factor of 10 was required to prevent significant weight gains and a significant amount of nodules from forming during 100 hours of exposure. The two alloys that had an alloying content factor of 10 were Fe-7.5Al-5Cr and Fe-10Al. In order to completely prevent nodules from forming on the alloy surface over 100 hours of exposure, it was found that an alloying content factor of 12.5 was required, which corresponded to the Fe-10Al-5Cr alloy.

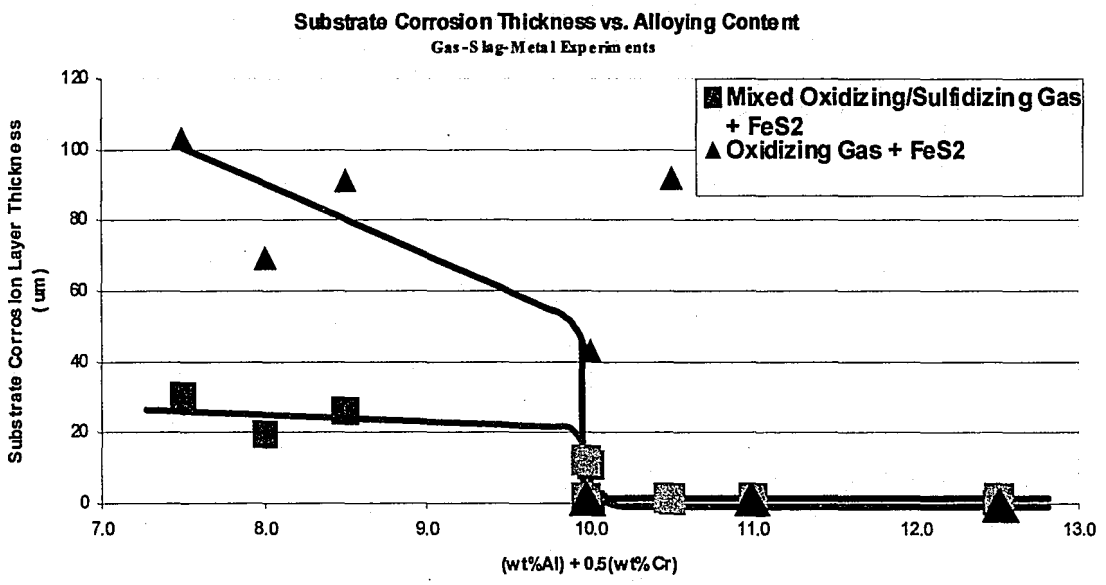

Figure 63 – Substrate corrosion layer thickness plotted against the alloying content factors for each alloy.

5.3.3 Effect of Water Vapor

Mixed Oxidizing/Sulfidizing Environment

Two alloys were exposed to the mixed oxidizing/sulfidizing with and without the presence of water vapor. Fe-7.5Al-5Cr and Fe-10Al were the two alloys chosen for this part of the study because they both have an alloying content factor of 10 and lie directly on the border between protective and non-protective compositions. The kinetic results from these experiments can be seen in Figure 64. From this figure it can be seen that there was a dramatic change in the corrosion kinetics of Fe-7.5Al-5Cr when water vapor was removed from the mixed oxidizing/sulfidizing gas. Fe-7.5Al-5Cr gained on the order of 5mg/cm^2 during 100 hours of exposure to the wet mixed oxidizing/sulfidizing environment, but then only gained approximately 0.8mg/cm^2 when exposed to the dry mixed oxidizing/sulfidizing gas for 100 hours. On the other hand, the Fe-10Al alloy showed similar results but with less of a difference in the overall weight gain. As can be seen in the figure, Fe-10Al gained approximately 1mg/cm^2 when exposed to the wet mixed oxidizing/sulfidizing gas, but had a weight gain on the order of 0.15mg/cm^2 during exposure to the dry mixed oxidizing/sulfidizing gas for 100 hours. These trends, which showed that the presence of water vapor increased the high temperature corrosion kinetics, were expected from the literature[86-91].

When considering the amount of surface area covered by external nodules, it was seen that the amount of external nodules present on the surface decreased when the water vapor was removed from the wet mixed oxidizing/sulfidizing environment. This effect of water vapor on nodule area fraction can be seen in Table 13, which shows the area fraction covered by external nodules for the two alloys exposed to the wet and dry mixed oxidizing/sulfidizing environments. It can be seen from this table that removal of water vapor from the wet mixed oxidizing/sulfidizing gas resulted in a significant decrease in the area covered by external nodule growth for both alloys. The Fe-7.5Al-5Cr alloy was completely covered by an external scale

after exposure to the wet mixed oxidizing/sulfidizing atmosphere, but the area covered by an external scale decreased almost 50% when the water vapor was removed. Similarly for the Fe-10Al alloy, the amount of area covered by nodules decreased from 82% in the wet environment to approximately 2% without the presence of water vapor. Although the amount of surface area covered by nodules changed with the presence of water vapor, the morphology of the nodules did not seem to vary between the samples exposed to the wet and dry mixed oxidizing/sulfidizing environment as can be seen in Figure 65.

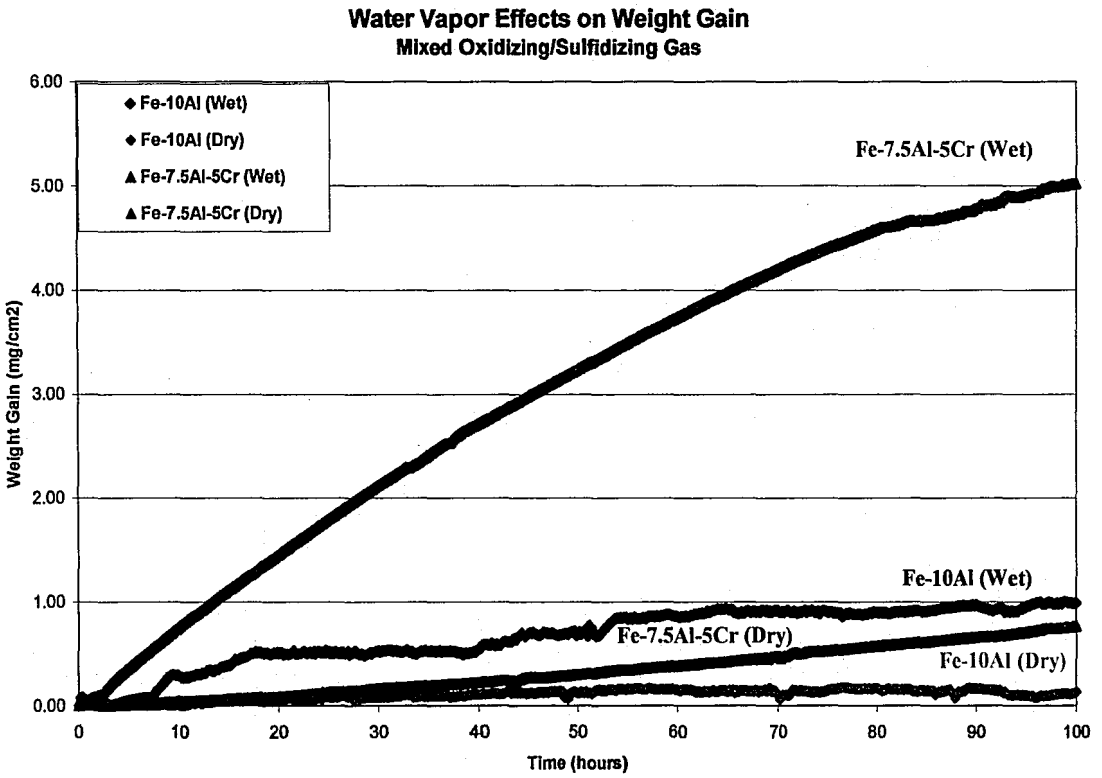

Figure 64 – Kinetic results from samples exposed to the mixed oxidizing/sulfidizing environment with and without the presence of water vapor.

Table 13 – Surface area fraction covered by external nodules of samples exposed to the wet and dry mixed oxidizing/sulfidizing environments (%).

Alloy	Wet Mixed Oxidizing/Sulfidizing Environment	Dry Mixed Oxidizing/Sulfidizing Environment
Fe-7.5Al-5Cr	100	54
Fe-10A	82	2

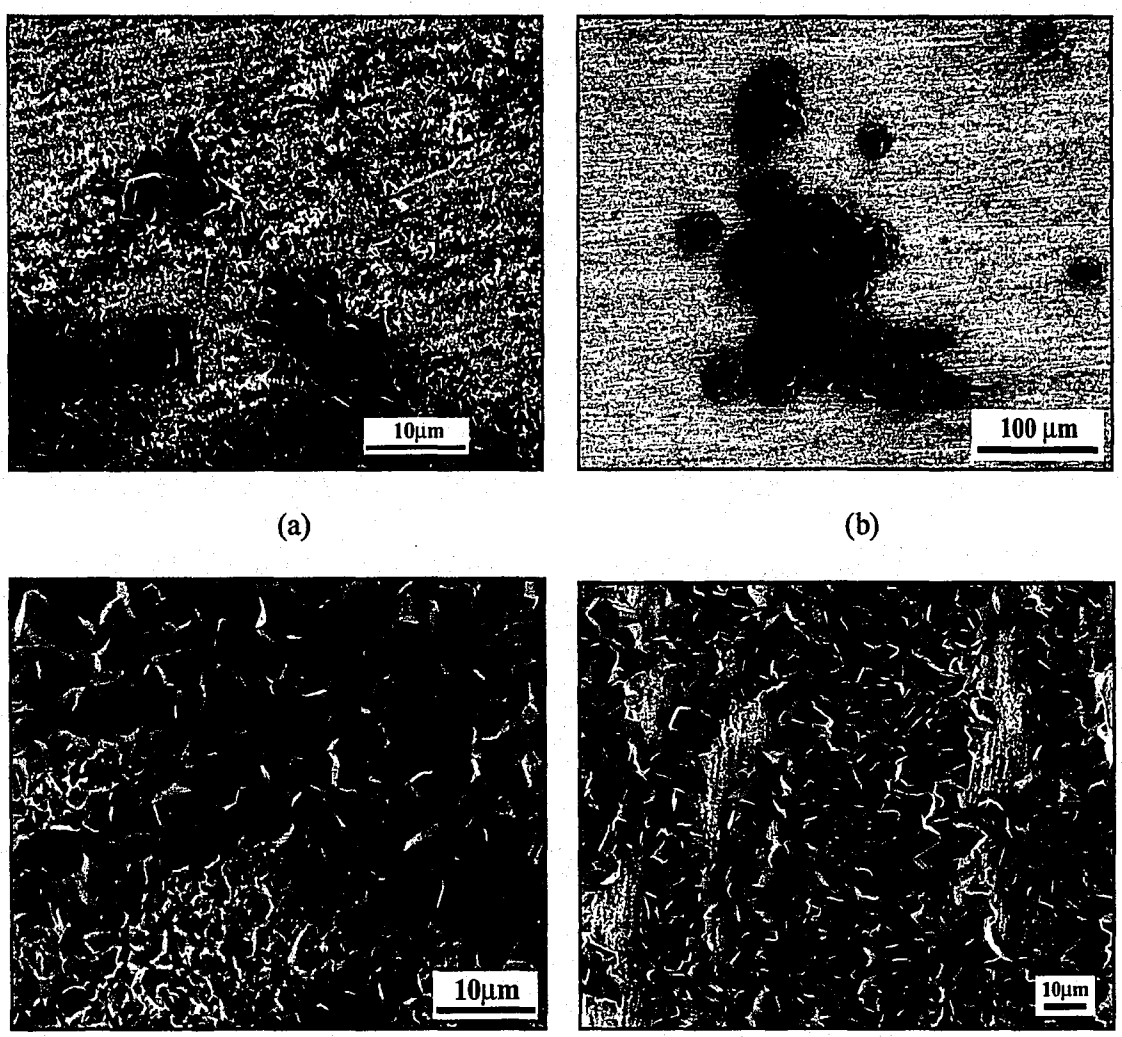

Figure 65 – Scale morphology samples exposed to the wet and dry mixed oxidizing/sulfidizing environments. It can be seen that there is not a significant difference in the scale morphology between Fe-10Al exposed to the wet environment (a) and the dry environment (b). The scale morphology between Fe-7.5Al-5Cr exposed to the wet environment (c) is very similar to the morphology of the alloy exposed to the dry environment (d).

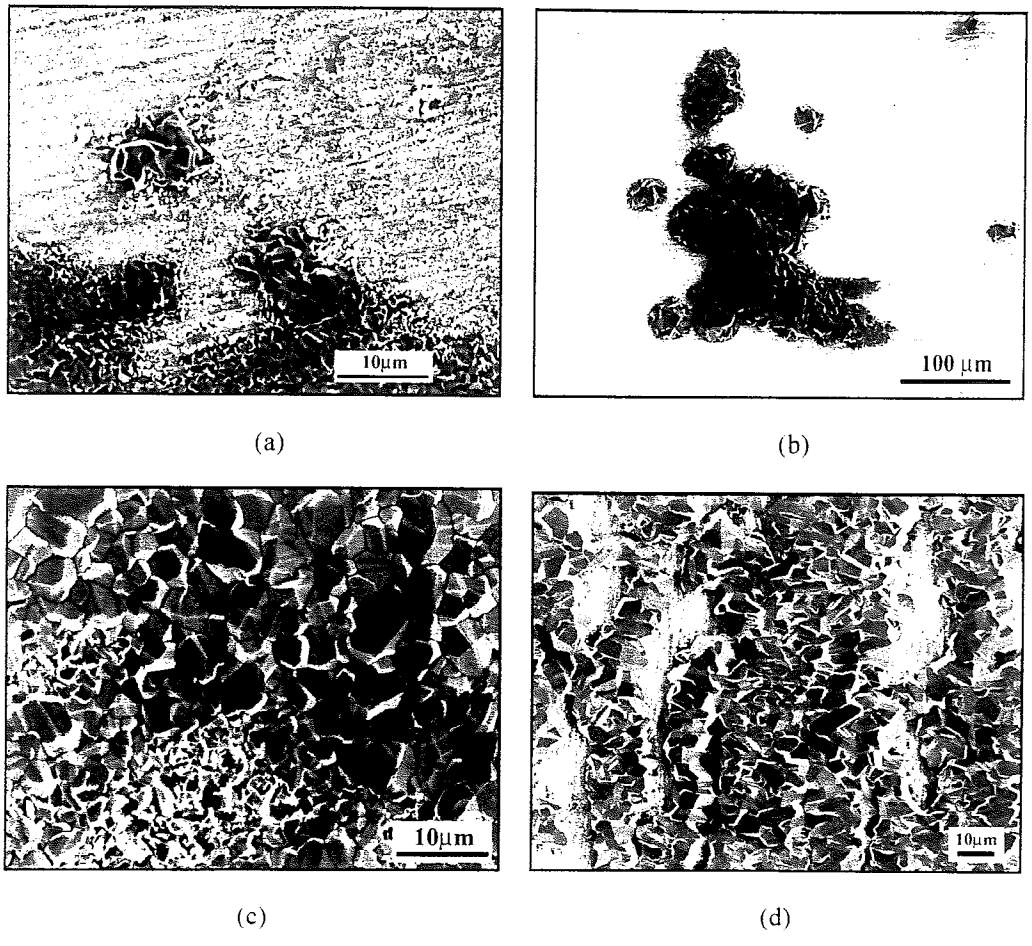

Figure 65 – Scale morphology samples exposed to the wet and dry mixed oxidizing/sulfidizing environments. It can be seen that there is not a significant difference in the scale morphology between Fe-10Al exposed to the wet environment (a) and the dry environment (b). The scale morphology between Fe-7.5Al-5Cr exposed to the wet environment (c) is very similar to the morphology of the alloy exposed to the dry environment (d).

Oxidizing Environment

The same two alloys exposed to the wet and dry mixed oxidizing/sulfidizing atmospheres were exposed to the oxidizing environment with and without the presence of water vapor. The kinetic results of these experiments can be seen in Figure 66. It can be seen from this figure that the effect of water vapor on the corrosion kinetics was consistent with the effect observed on the same samples exposed to both the wet and dry mixed oxidizing/sulfidizing environments. The Fe-7.5Al-5Cr sample exposed to the wet oxidizing environment gained approximately 0.2mg/cm^2, but the amount of weight gain decreased by an order of magnitude to approximately 0.02mg/cm^2 when the water vapor was removed from the gas. Although the overall weight gain of the Fe-10Al alloy did not change much between the wet and dry oxidizing environments, the initial growth kinetics seemed to be a bit more rapid in the wet oxidizing environment up to approximately 40 hours.

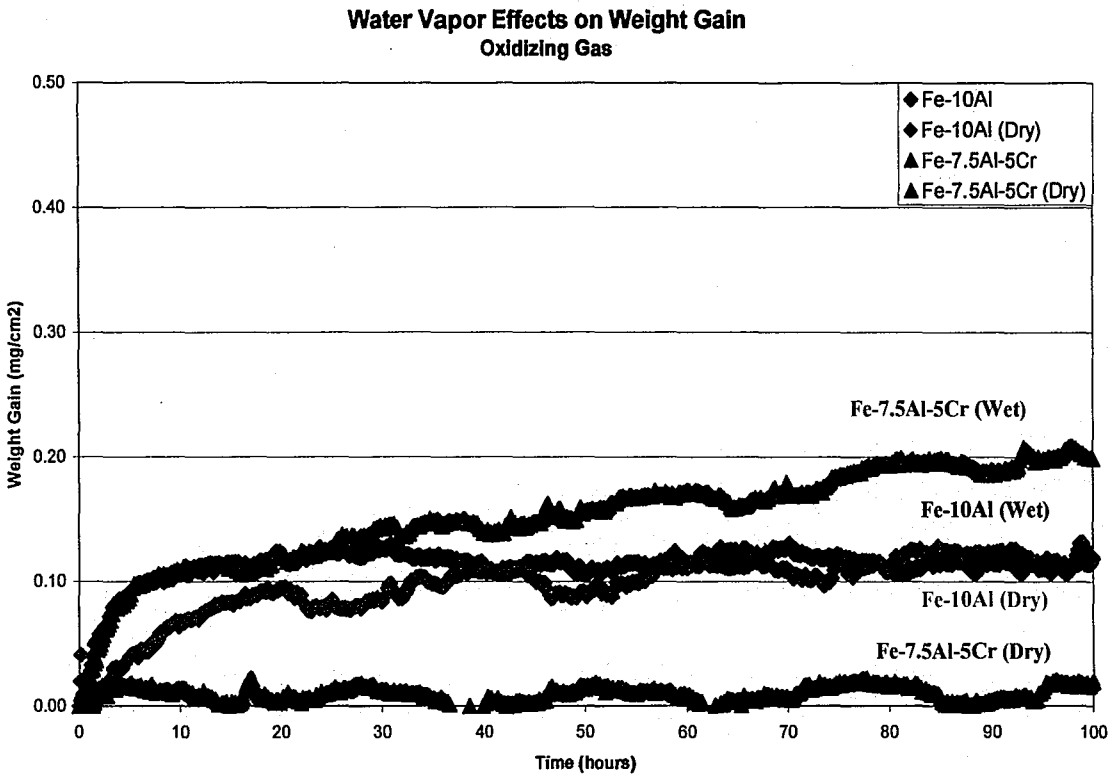

Figure 66 – Kinetic results from samples exposed to the oxidizing environment with and without the presence of water vapor.

The amount of surface area covered by external nodules again varied depending on whether water vapor was present in the environment or not. Removing water vapor from the wet oxidizing environment resulted in a decrease in the amount of area covered by nodules, which can be seen in Table 14. As can be seen in this table, Fe-7.5Al-5Cr showed a dramatic decrease in nodule area fraction as it decreased from approximately 60% to <1% when water vapor was removed from the wet oxidizing environment. The Fe-10Al samples also showed a decrease in the nodule area fraction when water vapor was removed from the environment, but the change was not as large as seen with the Fe-7.5Al-5Cr samples.

When considering the scale morphology between the wet and dry oxidizing environments, the external nodules formed on the Fe-7.5Al-5Cr samples in the wet oxidizing gas were different from the few scattered nodules that could be seen on the sample exposed to the dry

oxidizing gas. These nodules formed on the Fe-7.5Al-5Cr samples exposed to both the wet and dry oxidizing environments can be seen in Figure 67. The Fe-10Al samples exposed to the wet and dry oxidizing environments formed nodules that had much different morphologies as well. Figure 68 shows that the nodules formed on the sample exposed to the wet oxidizing atmosphere formed large nodules over 100μm in diameter, whereas the sample exposed to the dry oxidizing atmosphere formed very small nodules in sporadic areas on the sample. These differences in the morphology of the nodule corrosion products were consistent with observations made by previous researchers that water vapor effects the morphology of the non-protective corrosion products that form once the passive layer breaks down[90,91]. Although this theory is consistent with results obtained for alloys exposed to the oxidizing environment, the nodule morphology did not significantly change when the water vapor was removed from the mixed oxidizing/sulfidizing environment.

Table 14 – Surface area fraction covered by external nodules of samples exposed to the wet and dry oxidizing environments (%).

Alloy	Wet Oxidizing Environment	Dry Oxidizing Environment
Fe-7.5Al-5Cr	60	< 1
Fe-10Al	15	< 1

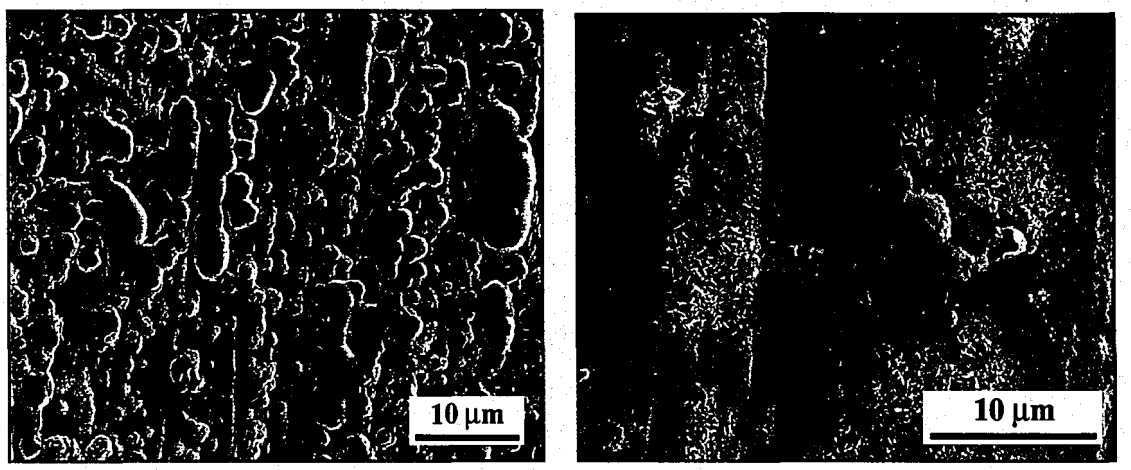

(a) (b)

Figure 67 – Nodule morphology of Fe-7.5Al-5Cr exposed to the wet (a) and the dry (b) oxidizing environments.

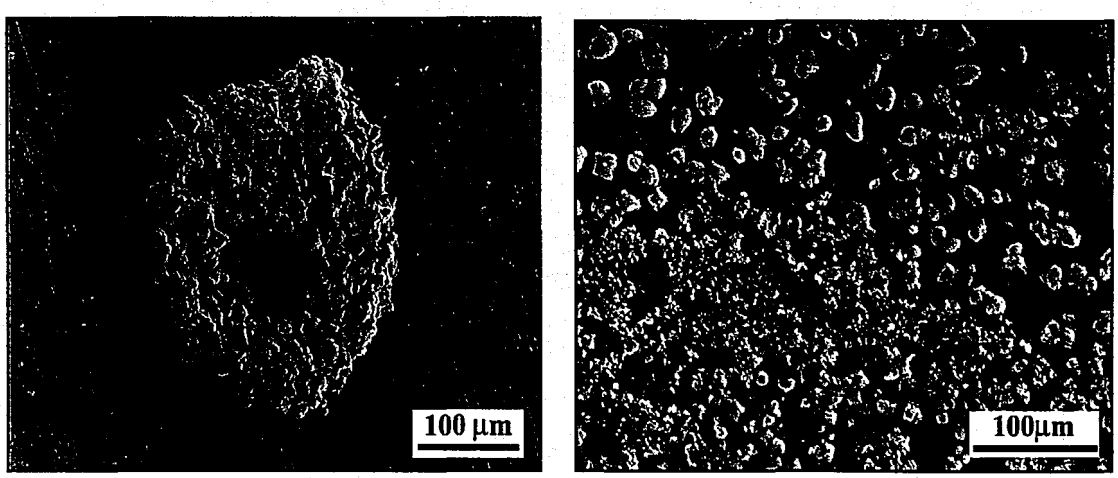

(a) (b)

Figure 68 – Nodule morphology of Fe-10Al exposed to the wet (a) and the dry (b) oxidizing environments.

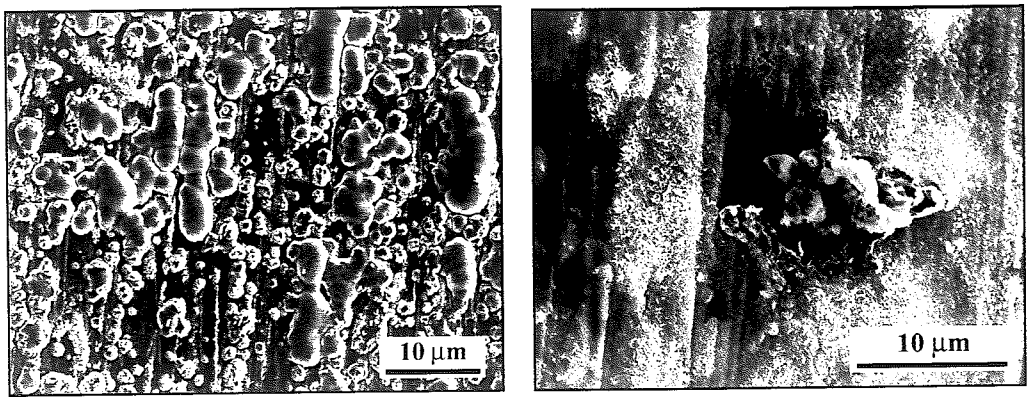

(a) (b)

Figure 67 – Nodule morphology of Fe-7.5Al-5Cr exposed to the wet (a) and the dry (b) oxidizing environments.

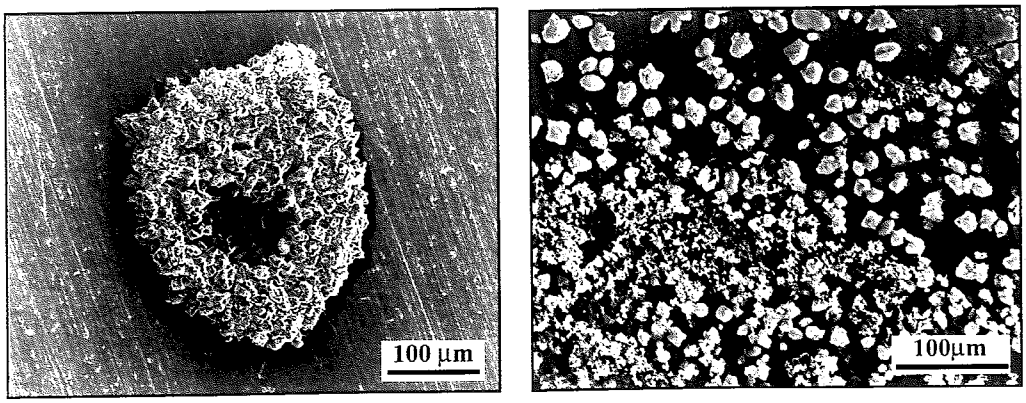

(a) (b)

Figure 68 – Nodule morphology of Fe-10Al exposed to the wet (a) and the dry (b) oxidizing environments.

5.4 Conclusions

When considering the three criteria used to determine the critical alloying content needed to obtain a protective weld overlay coating:

- The total weight gain and surface area covered by nodules were considered for gaseous corrosion samples, while the substrate corrosion layer thickness was considered for gas-slag-metal corrosion samples.
- An alloying content factor was established by regression analysis and was found to be: $F = (wt\%Al) + 0.5(wt\%Cr)$.
- It was found that an alloying content factor of 10 was required to significantly reduce the total weight gains and the surface area covered by nodule growth for gaseous samples tested in a sulfidizing, a mixed oxidizing/sulfidizing, and an oxidizing environment.
- The same alloying content factor (F=10) was also required to almost completely eliminate the substrate corrosion layer for samples in contact with FeS_2 powder while exposed to the mixed oxidizing/sulfidizing and the oxidizing environments.
- Although an alloying factor of 10 significantly reduced the amount of corrosion that occurred on these alloys, an alloying content factor of 12.5 was required to completely reduce the amount of surface area covered by nodule growth and was therefore the most protective alloying composition.
- It was therefore concluded that although alloys such as Fe-7.5Al-5Cr and Fe-10Al (F=10) are the critical compositions needed to reduce the amount of corrosion that takes place, an alloy with a greater alloying content factor, such as Fe-10Al-5Cr (F=12.5), is required to completely prevent corrosion from occurring at 500°C for 100 hours (as measured by passive layer breakdown and nodule formation).

The effect of water vapor was also considered in this chapter, by exposing selected samples to wet and dry mixed oxidizing/sulfidizing and oxidizing environments. The results showed that:

- The presence of water vapor in high temperature corrosive environments increases the corrosion kinetics (and in turn the overall weight gain) as well as the amount of external nodules that form on the surface of the alloy.
- Water vapor did not seem to have an effect on the nodule morphology formed on alloys exposed to the mixed oxidizing/sulfidizing environment, but did change the nodule morphology formed on alloys exposed to the oxidizing environment.
- It was found that the alloy containing chromium (namely Fe-7.5Al-5Cr) was influenced by the presence of water vapor to a greater extent than the binary alloy (Fe-10Al). The influence of water on high temperature corrosion may be due to the shift in the oxygen partial pressure that occurs when water vapor is removed from the mixed oxidizing/sulfidizing or the oxidizing environments.

6. References

1. C. G. McKamey, J. H. DeVan, P. F. Tortorelli, and V. K. Sikka, A review of recent developments in iron-aluminum (Fe_3Al)-based alloys. *J. Mater. Res.* **6**, 1779-1805 (1991).

2. G. Y. Lai. Investigation of Long-Term Oxidation of Several Alloys in Air and Combustion Atmospheres. [Paper No. 231]. (1993). NACE International. CORROSION/93.

3. J. H. DeVan and P. F. Tortorelli, Oxidation/sulfidation of iron-aluminum alloys. *Mater. High Temp.* **11**, 30-35 (1993).

4. J. H. DeVan. Development of surface treatments and alloy modifications for corrosion-resistant oxide scales. (1990). Proc. Annu. Conf. Fossil Energy Mater., 4th.

5. P. F. Tortorelli, J. H. De Van, and U. K. Abdali. Cyclic Oxidation of Iron Aluminides. [Paper No. 258]. (1993). NACE International. CORROSION/93.

6. P. F. Tortorelli and J. H. DeVan. Compositional influences on the high-temperature corrosion resistance of iron aluminides. (1994). Process., Prop. Appl. Iron Aluminides, Proc. Symp. Annu. Meet. Miner., Met. Mater. Soc.

7. S. W. Banovic, J. N. DuPont, and A. R. Marder. Weldability and high temperature sulfidation behavior of iron-aluminum weld overlays. (1999). Trends Weld. Res., Proc. Int. Conf., 5th.

8. S. W. Banovic, J. N. DuPont, and A. R. Marder, High temperature sulfidation behavior of low-Al iron-aluminum compositions. *Scr. Mater.* **38**, 1763-1767 (1998).

9. K. Luer, J. DuPont, and A. Marder, High-temperature sulfidation of Fe sub 3Al thermal spray coatings at 600 deg C. *Corrosion* **56**, 189-198 (2000).

10. R. Whitaker. EPRI Journal, 18-25. (1982).

11. Jones C., Maladies of Low-NOx Firing Come Home to Roost. *Power* **January/February**, 54-60 (1997).

12. E. Raask, *Mineral Impurities in Coal Combustion*, Hemisphere Publishing, Washington, D.C. (2001).

13. J. E. Gabrielson and E. D. Kramer. Measurement of Reducing Gases Formed in Low NOx Combustion. 1, 19-23. (1996). ASME. 1996 Joint Power Generation Conference.

14. F. Clarke and C. W. Morris. Combustion aspects of furnace wall corrosion. (1983). Corros. Resist. Mater. Coal Convers. Syst., [Proc. Int. Conf.].

15. W. T. Bakker and J. Stringer, Mixed oxidant high temperature corrosion in gasifiers and power plants. *Mater. High Temp.* **14**, 101-108 (1997).

16. Y. Kawahara, Development and Application of High-Temperature Corrosion-Resistant Materials and Coatings for Advanced Waste-to-Energy Plants. *Materials at High Temperatures* **14**, 191-198 (1997).

17. K. Shimizu, R. C. Furneaux, G. E. Thompson, G. C. Wood, A. Gotoh, and K. Kobayashi, On the nature of "easy paths" for the diffusion of oxygen in thermal oxide films on aluminum [Erratum to document cited in CA115(4):33733n]. *Oxid. Met.* **36**, 505 (1991).

18. S. Mrowec and K. Przybylski, Transport properties of sulfide scales and sulfidation of metals and alloys. *Oxid. Met.* **23**, 107-139 (1985).

19. H. A. Wriedt, Fe-O Equilibrium Phase Diagram. In *Binary Alloy Phase Diagrams 2nd Ed.*, ed. by T. Massalski, pp 1739-1744. ASM International, Metals Park, OH (1990).

20. Kubaschewski, Fe-S Equilibrium Phase Diagram. In *Binary Alloy Phase Diagrams 2nd Ed.*, ed. by T. Massalski, pp 1762-1765. ASM International, Metals Park, OH (1990).

21. U. R. Kattner, Fe-Al Equilibrium Phase Diagram. In *Binary Alloy Phase Diagrams 2nd Ed.*, ed. by T. Massalski, pp 147-149. ASM International, Metals Park, OH (1990).

22. L. Rimlinger, *Compt. Rend. Acad. Sci.* **261**, 4090 (1965).

23. H. A. Wriedt, Al-O Equilibrium Phase Diagram. In *Binary Alloy Phase Diagrams 2nd Ed.*, ed. by T. Massalski, pp 185-186. ASM International, Metals Park, OH (1990).

24. R. Prescott and M. J. Graham, The formation of aluminum oxide scales on high-temperature alloys. *Oxid. Met.* **38**, 233-254 (1992).

25. G. C. Rybicki and J. L. Smialek, Effect of the .theta.-.alpha.-aluminum oxide transformation on the oxidation behavior of .beta.-nickel-aluminum + zirconium. *Oxid. Met.* **31**, 275-304 (1989).

26. J. K. Doychak and T. E. Mitchell. Formation of single-crystal aluminum oxide scales on .beta.-nickel-aluminum. 1. (1984). Proc. - Int. Congr. Met. Corros.

27. E. J. Felten and F. S. Pettit, Development, growth, and adhesion of aluminum(III) oxide on platinum-aluminum alloys. *Oxid. Met.* **10**, 189-223 (1976).

28. T. A. Ramanarayanan, M. Raghavan, and R. Petkovic-Luton, Alumina scales on ODS alloys. *Proc. - Electrochem. Soc.* **83-5**, 479-494 (1983).

29. I. Levin, T. Gemming, and D. G. Brandon, Some metastable polymorphs and transient stages of transformation in alumina. *Phys. Status Solidi A* **166**, 197-218 (1998).

30. W. E. Boggs, Oxidation of iron-aluminum alloys from 450.deg. to 900.deg. *J. Electrochem. Soc.* **118**, 906-913 (1971).

31. R. C. Sharma and Y. A. Chang, Al-S Equilibrium Phase Diagram. In *Binary Alloy Phase Diagrams 2nd Ed.*, ed. by T. Massalski, pp 203-206. ASM International, Metals Park, OH (1990).

32. V. Raghavan, Fe-Al-O Equilibrium Phase Diagram. In *Phase Diagrams of Ternary Alloys, Pt. 5* pp 10-28. The Indian Institute of Metals, Calcutta, India (1989).

33. V. Raghavan, Fe-Al-S Equilibrium Phase Diagram. In *Phase Diagrams of Ternary Alloys, Pt. 2* pp 24-34. The Indian Institute of Metals, Calcutta, India (1988).

34. G. Banik, T. Schmitt, P. Ettmayer, and B. Lux, Cr-O Equilibrium Phase Diagram. In *Binary Alloy Phase Diagrams 2nd Ed.*, ed. by T. Massalski, pp 1304-1305. ASM International, Metals Park, OH (1990).

35. M. Venkatraman and J. P. Neumann, Cr-S Equilibrium Phase Diagram. In *Binary Alloy Phase Diagrams 2nd Ed.*, 2 Edn, ed. by T. Massalski, pp 1322-1326. ASM International, Metals Park, OH (1990).

36. J. L. Murray and H. A. Wriedt, Ti-O Equilibrium Phase Diagram. In *Binary Alloy Phase Diagrams 2nd Ed.*, ed. by T. Massalski, pp 2924-2927. ASM International, Metals Park, OH (1990).

37. J. L. Murray, Ti-S Equilibrium Phase Diagram. In *Binary Alloy Phase Diagrams 2nd Ed.*, ed. by T. Massalski, pp 3286-3288. ASM International, Metals Park, OH (1990).

38. B. Sundmann, B. Jansson, and J. O. Andersson, *CALPHAD* **9**, 153 (1985).

39. HSC. HSC Chemistry for Windows, Version 4.0. [4.0]. (1997). Oy, Finland, Outokupmu Research.

40. CRC, *CRC Handbook of Chemsitry and Physics 74th Ed.*, London, England (1993).

41. W. Smith, *Principles of Materials Science and Engineering*, McGraw-Hill, Inc., New York, NY (1996).

42. K. N. Strafford and R. Manifold, Corrosion of iron and some iron-based alloys in sulfur vapor at 500.deg. *Corros. Sci.* **9**, 489-507 (1969).

43. N. Birks and G. H. Meier, *Introduction to High-Temperature Oxidation of Metals*, Edward Arnold Ltd., London, England (1982).

44. F. Saegusa and L. Lee, Oxidation of iron-aluminum alloys in the range of 500-1000.degree. *Corrosion* **22**, 168-177 (1966).

45. C. Wagner, Passivity and Inhibition During the Oxidation of Metals at Elevated Temperatures. *Corros. Sci.* **5**, 751-764 (1965).

46. P. Kofstad, *High-Temperature Oxidation of Metals*, (1967).

47. P. Tomaszewicz and G. R. Wallwork, Observations of nodule growth during the oxidation of pure binary iron-aluminum alloys. *Oxid. Met.* **19**, 165-185 (1983).

48. S. W. Banovic, J. N. DuPont, and A. R. Marder, Growth of nodular corrosion products on Fe-Al alloys in various high-temperature gaseous environments. *Oxid. Met.* **54**, 339-369 (2000).

49. W. C. Hagel, The oxidation of iron-, nickel-, and cobalt-base alloys containing aluminum. *Corrosion* **21**, 316-26, (1965).

50. M. Sakiyama, P. Tomaszewicz, and G. R. Wallwork, Oxidation of iron-nickel-aluminum alloys in oxygen at 600-800.degree.C. *Oxid. Met.* **13**, 311-330 (1979).

51. J. P. Orchard and D. J. Young, Gas-phase composition effects on the iron sulfide scaling reaction. *J. Electrochem. Soc.* **133**, 1734-1741 (1986).

52. R. A. Meussner and C. E. Birchenall, The growth of ferrous sulfide on iron. *Corrosion* **13**, 677t-689t (1957).

53. P. Tomaszewicz and G. R. Wallwork, The oxidation of high-purity iron-chromium-aluminum alloys at 800.degree. *Oxid. Met.* **20**, 75-109 (1983).

54. P. Tomaszewicz and G. R. Wallwork, Iron-aluminum alloys: a review of their oxidation behavior. *Rev. High-Temp. Mater.* **4**, 75-105 (1978).

55. P. F. Tortorelli and K. Natesan, Critical factors affecting the high-temperature corrosion performance of iron aluminides. *Mater. Sci. Eng. , A* **A258**, 115-125 (1998).

56. G. R. Wallwork and M. B. McGirr, *Stress Effects and the Oxidation of Metals*, Metal Society of the American Institute of Mining, Metallurgical, and Petroleum Engineers, New York, NY (1975).

57. K. N. Strafford and R. Manifold, Scaling behavior of an iron-5% aluminum alloy in sulfur vapor. *Oxid. Metals* **1**, 221-240 (1969).

58. K. N. Strafford and R. Manifold, Effects of aluminum alloying additions on the sulfidation behavior of iron. *Oxid. Metals* **5**, 85-112 (1972).

59. P. C. Patnaik and W. W. Smeltzer, Sulfidation properties of iron-aluminum alloys at 1173 K in hydrogen sulfide-hydrogen atmospheres. *Oxid. Met.* **23**, 53-75 (1985).

60. P. C. Patnaik and W. W. Smeltzer, Sulfidation properties of iron-aluminum alloys (6-28 a/o aluminum) at 1173 K in sulfur vapor at $PS_2 = 1.45x10^{-3}$ Pa. *J. Electrochem. Soc.* **132**, 1226-1232 (1985).

61. P. J. Smith and W. W. Smeltzer, A method for long-term sulfidation of metal at low sulfur pressures and its application to sulfidation of an iron-20 at.% aluminum alloy at 1023 K. *Oxid. Met.* **28**, 291-308 (1987).

62. P. J. Smith, P. R. S. Jackson, and W. W. Smeltzer, The sulfidation behavior of an iron-10 atomic percent aluminum alloy in argon-sulfur and hydrogen-hydrogen sulfide atmospheres at 1023 K. *J. Electrochem. Soc.* **134**, 1424-1431 (1987).

63. P. F. Tortorelli and J. H. DeVan, Behavior of iron aluminides in oxidizing and oxidizing/sulfidizing environments. *Mater. Sci. Eng. , A* **A153**, 573-577 (1992).

64. P. F. Tortorelli, G. M. Goodwin, M. Howell, and J. H. DeVan. Weld-overlay iron-aluminide coating for use in high temperature oxidizing/sulfidizing environments. (1995). Heat-Resist. Mater. II, Conf. Proc. Int. Conf., 2nd.

65. J. H. DeVan, P. F. Tortorelli, and U. K. Abdali. Environmental effects on iron aluminides. 217-226. (1992). Oak Ridge Natl. Lab., [Rep.] ORNL/FMP (U. S.).

66. W. Kai, J. P. Chu, R. T. Huang, and P. Y. Lee, High temperature corrosion behavior of iron aluminides containing ternary additions in H2/H2S/H2O mixed gases. *Mater. Sci. Eng. , A* **A239-240**, 859-870 (1997).

67. O. T. Goncel, A. S. Sasa, and K. N. Strafford. 316-322. (1984). Turkey International Congress Metallic Corrosion.

68. W. Kai and R. T. Huang, The high-temperature corrosion behavior of Nb-Al alloys in a $H_2/H_2S/H_2O$ gas mixture. *Oxid. Met.* **48**, 439-470 (1997).

69. G. H. Fair and J. V. Wood, Mechanical alloying of iron-aluminum intermetallics. *Powder Metall.* **36**, 123-128 (1993).

70. P. F. Tortorelli, I. G. Wright, G. M. Goodwin, and M. Howell. High-temperature oxidation/sulfidation resistance of iron-aluminide coatings. (1996). Elevated Temp. Coat.: Sci. Technol. II, Proc. Symp.

71. J. H. DeVan. Oxidation behavior of iron-aluminum (Fe3Al) and derivative alloys. (1988). Oxid. High-Temp. Intermet., Proc. Workshop.

72. B. A. Pint, Study of the reactive element effect in ODS iron-base alumina formers. *Mater. Sci. Forum* **251-254**, 397-404 (1997).

73. R. F. A. Jargelius-Pettersson, Application of the pitting resistance equivalent concept to some highly alloyed austenitic stainless steels. *Corrosion* **54**, 162-168 (1998).

74. M. W. Brumm and H. J. Grabke, The oxidation behavior of nickel aluminide (NiAl). I. Phase transformations in the alumina scale during oxidation of NiAl and NiAl-chromium alloys. *Corros. Sci.* **33**, 1677-1690 (1992).

75. D. Renusch, B. W. Veal, K. Natesan, L. Koshelev, and M. Grimsditch, Strain measurements in thermally grown alumina scales using ruby fluorescence. *Proc. - Electrochem. Soc.* **96-26**, 62-73 (1997).

76. P. F. Tortorelli, J. H. DeVan, G. M. Goodwin, and M. Howell. High-temperature corrosion resistance of weld overlay coatings of iron aluminide. (1995). Elevated Temp. Coat.: Sci. Technol. I, Proc. Symp.

77. C. Zhou, Y. Yang, S. Gong, and H. Xu, Effect of Ti-Al-Cr coatings on the high temperature oxidation behavior of TiAl alloys. *Materials Science and Engineering A* **307**, 182-187 (2001).

78. S. K. Wu and M.-R. Yang, Oxidation behavior and oxide layers of Ti-50Al intermetallics by preoxidation in high-pressure oxygen. *Oxid. Met.* **54**, 473-490 (2000).

79. T. Yoshioka and O. Ohashi, Behavior of high temperature oxidation of Ti(Al, X) sub 3 (X=Mn, Cr, Ag, Cu) and diffusion of TiAl/Ti(Al, X) sub 3 joints. *Journal of the Japan Institute of Metals* **64**, 1127-1132 (2000).

80. C. G. McKamey, C. T. Liu, J. V. Cathcart, S. A. David, and E. H. Lee. Evaluation of Mechanical and Metallurgical Properties of Fe3Al-Based Aluminides. ORNL/TM-10125. (1986). Oak Ridge, TN, Oak Ridge National Laboratory.

81. C. G. McKamey, C. T. Liu, S. A. David, J. A. Horton, D. H. Pierce, and J. J. Campbell. Development of Iron Aluminides for Coal Conversion Systems. ORNL/TM-10793. (1988). Oak Ridge, TN, Oak Ridge National Laboratory.

82. C. G. McKamey. ORNL/FMP-90/1. (1990). Oak Ridge, TN, U.S. Department of Energy. Proceedings of the Fourth Annual Conference on Fossil Energy Materials.

83. P. M. Giles and A. R. Marder. Patent. [3,859,079]. (1975).

84. D. Lin, D. Li , and Y. Xu, Oxidation behavior of FeAl alloys with and without titanium. *J. Mater. Sci.* **36**, 979-983 (2001).

85. G. Culbertson and C. S. Kortovich. Development of Iron Aluminides. AFWAL-TR-85-4155. (1987). Wright-Patterson Air Force Base, OH, Air Force Wright Aeronautical Laboratories.

86. H. Asteman, J. E. Svensson, L. G. Johansson, and M. Norell, Indication of chromium oxide hydroxide evaporation during oxidation of 304L at 873 K in the presence of 10% water vapor. *Oxid. Met.* **52**, 95-111 (1999).

87. Y. Ikeda and K. Nii, THE MECHANISM OF ACCELERATED OXIDATION OF Fe-Cr ALLOYS IN WATER VAPOR CONTAINING ATMOSPHERE. *Corr. Eng. Japan* **31**, 156-163 (1982).

88. H. Buscail and S. Heinze, Water-Vapor-Effect on the Oxidation of Fe-21.5wt%Cr-5.6wt%Al at 1000C. *Oxid. Met.* **47**, 445-464 (1997).

89. W. J. Sherwood, THE EFFECT OF WATER VAPOR ON THE OXIDATION BEHAVIOR OF DILUTE IRON-SILICON ALLOYS, (DISSERTATION). *Diss. Abstr. Int.* **47**, 175 (1987).

90. J. Shen and L. Zhou, High-Temperature Oxidation of Fe-Cr alloys in Wet Oxygen. *Oxid. Met.* **48**, 347-356 (1997).

91. J. Shen, L. Zhou, and T. Li, Effect of water vapor on high temperature oxidation of Fe-Cr alloys. *Chinese Journal of Materials Research* **12**, 128-132 (1998).

92. A. Galerie. How Does Water Vapor Influence the Nature, Growth Rate, Stress State and Adhesion of Thermal Oxide Scales? (2001). Gordon Research Conference on High Temperature Corrosion.

93. A. A. Fasching, D. I. Ash, G. R. Edwards, and S. A. David, Hydrogen cracking behavior in an iron aluminide alloy weldment. *Scr. Metall. Mater.* **32**, 389-394 (1995).

94. G. M. Goodwin, P. J. Maziasz, C. J. McKamey, J. H. DeVan, and V. K. Sikka. Weldability of iron aluminides. 205-210. (1994). Oak Ridge Natl. Lab., [Rep.] ORNL/FMP (U. S.).

95. S. W. Banovic, J. N. DuPont, P. F. Tortorelli, and A. R. Marder, The role of aluminum on the weldability and sulfidation behavior of iron-aluminum cladding. *Weld. Res. (Miami)* **78**, 23S-30S (1999).

96. S. W. Banovic, J. N. DuPont, and A. R. Marder. Corrosion resistance of weldable Fe-Al alloys in reducing environments. 12. (1999). P.O. Box 218340, Houston, TX, 77084, National Association of Corrosion Engineers. Corrosion 99. 4-25-1999.

97. K. Luer. Investigation of Gas-Deposit-Alloy Corrosion Interactions in Simulated Combustion Environments. (2000). Lehigh University.

98. J. H. DeVan and P. F. Tortorelli, The Oxidation-Sulfidation Behavior of Iron Alloys Containing 16-40at% Aluminum. *Corros. Sci.* **35**, 1065-1071 (1993).

99. S. Mrowec and M. Wedrychowska, Kinetics and mechanism of high-temperature sulfur corrosion of iron-chromium-aluminum alloys. *Oxid. Met.* **13**, 481-504 (1979).

100. S. W. Banovic, J. N. DuPont, and A. R. Marder, Corrosion behavior of weldable Fe-Al alloys in oxidizing-sulfidizing environments . *Mater. High Temp.* **16**, 195-199 (1999).

VITA

Jonathan Ryan Regina was born on June 6, 1977 in Bethlehem, PA to his parents Gail M. and Lawrence A. Regina. He grew up in the Pocono Mountains with his two younger brothers, Jeffrey and Jeremy, as well as his wife-to-be, Merideth. He graduated with honors in the spring of 1995 from Pleasant Valley High School, where he was the President of his class and captain of the football team. Jon began at Lehigh University in the fall of 1995 as a student athlete, taking both engineering classes and playing football. During his undergraduate career, he was inducted into several honor societies and was honored with the Cyril John Osborn Award, which is given to a student who exhibits outstanding promise for a successful career in Materials Science and Engineering. During this time he also played on two championship football teams, one of which went undefeated in the regular season and took part in the NCAA I-AA National Playoffs (1998). In the spring of 1999, Jonathan graduated with a Bachelors of Science Degree in Materials Science and Engineering. He entered the Materials Science and Engineering Department as a graduate student in the fall of 1999. On June 30, 2001, Jon married his long time friend and high-school sweetheart Merideth Jane Skinner.

END OF TITLE